# THE UNIVERSITY OF KWAZULU-NATAL

# THE EFFECT OF FRETTING MARKS INTRODUCED DURING STRAND WINDING ON THE FATIGUE PERFORMANCE OF TRANSMISSION LINE CONDUCTORS

**Larry Chama Botha**

213570453

**Supervisors:**

**Dr Richard Loubser**

**Dr Rob Stephen**

**Dr Innocent Davidson**

December, 2015

Submitted in fulfilment of the academic requirements for the degree of Master of Science in Engineering at the School of Mechanical Engineering, University of KwaZulu-Natal

# DECLARATION 1-PLAGIARISM

I, Larry Chama Botha, declare that

1. The research report in this thesis, except where otherwise indicated, is my own original research.
2. This thesis is not submitted for any degree or examination at any other university.
3. This thesis does not contain other persons' data, pictures graphs or other information, unless specifically acknowledged as being sourced from other persons
4. This thesis does not contain other persons' writing, unless specifically acknowledged as being sourced from other researchers. Where other written sources have been quoted, then:
    a) Their work has been re-written but general but general information attributed to them as been referenced
    b) Where their exact words have been used, then their writing has been placed in italics and inside quotation marks, and referenced.
5. This thesis does not contain text, graphics or tables copied and pasted from the internet, unless specifically acknowledged, and the source being detailed in the thesis and in the Reference sections.

Signed

……

SUPERVISOR

As the candidate's Supervisor I agree/do not agree to the submission of this thesis

Signed

……

# DECLARATION 2-PUBLICATIONS

DETAILS OF CONTRIBUTION TO PUBLICATIONS

1. **Elasto-Plastic Interlayer contact modelling of the Tern Conductor,** The Journal of Strain Analysis for Engineering Design

2. **The Effect of Fretting Marks Introduced During Strand Winding on the Fatigue Performance of Transmission Line Conductors,** IEE-PES Conference, 2016

3. **Improving the Quality of Overhead Line Conductors during Manufacturing,** IEEE- PES Conference, 2016

Signed:

.....

# Abstract

In this research, the Elasto-plastic interlayer contact of the TERN ACSR conductor used on Eskom's 400kV transmission lines is investigated. Characterization of the elliptical contact marks using eucentric tilting in SEM stereomicroscopy for depth measurement is conducted. The size of these manufacturing defects (fret marks) resulting from the strand winding process is quantified.

The already established observation that two geometrically dissimilar contacting surfaces may exhibit the same contact mechanics is extensively used to explain how the variations in stranding lay ratios affects the size of the fret marks and hence the surface quality of strands. From this supposition, an equivalent contacting sphere radius is calculated and used for both nonlinear and linear elastic finite element Analysis (FEA) in MSC Marc mentat.

An inner conductor contact mechanics model for determining the normal contact force per defect is also presented and used with existing inner conductor mechanics models for tension determination. The calculated equivalent radius shows strong linear correlation with the defect size, contact force, plastic strain and stress and can therefore be used in the design of conductors.

Fatigue testing was then conducted on two (02) TERN conductors. Fractographic analysis of the samples exposed to fatigue cycles was conducted using the Scanning Electron Microscopy (SEM) and Field Emission SEM (FEGSEM). Energy Dispersive Spectroscopy was also used for Surface Elemental analysis before and after the fatigue testing to analyse the changes in material composition on the fret mark surfaces.

# Acknowledgements

I would like to thank;

1. My core Supervisors Dr Richard Loubser and Dr Rob Stephen for their invaluable technical input and guidance throughout the course of my research
2. Mr Pravesh Moodley for is assistance in the setting up of the fatigue tests and during the fatigue testing
3. Mr Bertie Jacobs of Eskom for his input from the inception of this research
4. My family and friends for their patience, understanding and motivation
5. Aberdare Cables, South Africa for their financial support, technical input and provision of conductor samples
6. THRIP and the University of KwaZulu-Natal for their financial support
7. The Microscopy and Microanalysis Unit (MMU) of the University of KwaZulu-Natal for their dedication and patience
8. Eskom holdings for the infrastructure support and the training offered via Trans Africa Projects (TAP)
9. Dr Innocent Davidson for the administrative support, encouragement and guidance
10. Mr Henni Scholtz and Mr Jonathan Young of Aberdare cables for the provision of the necessary standards and controlled documents needed for this research.

# List of Acronyms

| | |
|---|---|
| ACSR | Aluminium Conductor Steel Reinforced |
| OHL | Overhead Line Conductor |
| EDS | Every Day Stress |
| EDS(X) | Electron Dispersive Spectroscopy |
| SEM | Scanning Electron Microscope |
| FEGSEM | Field Emission Gun Scanning Electron Microscope |
| LVDT | Linear Voltage Differential Transform |
| FCC | Fatigue crack propagation |
| LE | Linear Elastic |
| FEA | Finite Element Analysis |
| SANS | South Africa National Standards |
| IEC | International Electrotechnical Commission |
| EIFS | Initial Equivalent Flaw Size |
| IFS | Initial Flaw Size |

# List of Symbols

| | |
|---|---|
| $D_0$ | Outer diameter of conductor |
| $n_s$ | Number of still wires |
| $d_s$ | Diameter of the steel wires |
| $d_a$ | Diameter of aluminium wire |
| $n_a$ | Number of aluminium wires |
| $n_o$ | Number of wires in the outer layer |
| Re | Reynolds number |
| D | Diameter of the Conductor |
| V | Wind speed |
| $v$ | Viscosity coefficient |
| S | Strouhal number |
| $F_w$ | Frequency of the turbulences |
| A | Projected area of the conductor |
| $\omega$ | Angular frequency |
| t | Time |
| $R_w$ | Radius of the strand |
| $w$ | Width of the fret mark |
| f | Resonant frequency |
| L | Span Length |
| n | Mode of the vibration |
| $R_l$ | Lead wire resistance |
| $R_g$ | Nominal strain gauge resistance |
| GF | Gauge factor of the strain gauge |
| $\varepsilon$ | Strain (in micro-strains) |
| $V_0$ | Bridge output voltage |
| $V_0$ (Unstrained) | Bridge output voltage |
| $V_{ex}$ | Excitation voltage |
| D | Mean diameter or pitch |
| P | Lay length |
| $Y_b$ | Bending amplitude |
| $E$ | Modulus of Elastic |
| $\sigma_b$ | Bending stress ( 0 to peak) |
| $d$ | Diameter of the outer strand |
| $T$ | Conductor tension |

| | |
|---|---|
| $E*I$ | Flexural rigidity |
| F | Force |
| K | Stiffness |
| X | Displacement |
| $A_c$ | Cross section area and the |
| $E_c$ | Young Modulus of the core |
| $\Delta K$ | Stress intensity factor range |
| $S_{min}$ , $S_{max}$ | Maximum and Minimum Stresses in the cycle |
| $a$ | Crack length |
| $\Delta\sigma$ | Stress range |
| $D$ | Diameter of the strand |
| $M$ | Moment |
| $I$ | Second moment of area |
| $\sigma$ | Stress |
| $\gamma$ | Lay ratio |
| $\Delta K_c$ | Fracture toughness |

# Table of Contents

## Contents

# List of Figures

# List of Tables

# 1. Introduction

Electrical overhead transmission line conductors are very important assets in the electrical power industry as they are the wheels of the much needed electrical energy. Huge investment costs are associated with the construction of these lines and the conductor itself contributes up to 40% of the total initial cost. With the demand for energy rocketing and the need to improve the reliability of supply, additional lines will have to be erected resulting in huge investment costs more especially on the conductor itself. It is therefore desirable that the life of the conductor is optimized and its life cycle cost maintained to a minimum.

Overhead transmission line conductors are manufactured in stranding machines whose design affects the strains and stresses involved in forming the strands into helices (Rawlins, 2005). Aluminum wires on bobbins are inserted into the cradles of the winding cages, locked into position and tension set to between 10-15 kg for multilayer ACSR conductors depending on the number and size of aluminum wire. The conductor is alternately laid up by rotating the cages about a linearly moving central steel core. Different lay ratios and hence lay angles can be obtained by varying the rotation speed of the cages and/or the linear speed of the steel. In order to improve the structural integrity of the conductor, the haul off (lay) capstan is used to induce a tension which in turn loads the interlayer contact points resulting in permanent plastic strains at contact points. The result is recurring elliptical marks on the surface of the strands. If no tension is injected in the conductor, the strands will separate from the core when the conductor is in service, a phenomenon known as bird caging. Bird caging is commonly defined as the separation of aluminium wires in outer layers from the core of the conductor. BS EN 50182:2001 is however more stringent in its acceptance criteria for a stringing test with regards to bird caging. Although it stipulates that bird caging is the opening up of individual wires of a conductor by an unacceptable amount, the acceptance criteria is such that no individual outer layer wire shall be raised by more than one (01) wire diameter above its normal position for bird caging to be considered absent. The effects of bird caging include; reduced conductor mechanical strength and corona with all of its undesirable effects.

The major factor affecting the service life of transmission conductors is the fretting fatigue which is induced by the Aeolian vibrations (Karman vibrations). These high frequency, low amplitude vibrations will cause the initiation and propagation of cracks from the contacting surfaces of the conductor strands leading to strand breakages and eventual conductor failure.

Studies on many different metallic specimens have shown that fatigue crack initiation and growth (FCG) is accelerated by pre-existing flaws on the surface of the specimen. This research is therefore focused on the effect of the fretting marks introduced during strand

winding on the fatigue performance of overhead line conductors. These marks, which are a defect from the stranding process of the conductors, are inevitable in Aluminium Conductors Steel Reinforced (ACSR conductors).

The research presented in this thesis is devoted to the surface quality of ACSR TERN conductor and the effect of this quality on its fatigue performance. The Tern conductor is employed on Eskom's 400kV overhead transmission which currently has a major share in terms of power transmission on the South African Grid. This is a 45 aluminium wire and seven steel wire ACSR conductor with an outer diameter of 27.03mm. The standard diameter of the aluminium and galvanised steel wires is 3.38mm and 2.25mm respectively with a mass of 1340kg/km and an ultimate tensile strength of 98.7kN. The current rating for this conductor is 830A (below 100 degrees Celsius) and comes in standard drum length of 1500m.

Eskom is a South African electricity public utility, established in 1923 as the Electricity Supply Commission (ESCOM) by the government of South Africa in terms of the Electricity Act (1922). Eskom represents South Africa in the Southern African Power Pool. Eskom procures its TERN conductors from Aberdare Cables. Aberdare Cables is one of the leading cable manufacturers in South Africa. They supply most of their manufactured conductors to Eskom and supplied the TERN conductor which was used during the construction of the 400kV Duvha Leseding line. This is 206km high voltage transmission line running from Duvha to Leseding. It was during the construction of this line that Eskom raised a non-conformance report (NCR) on the quality of the TERN conductors supplied by Aberdare which motivated the research presented in this thesis.

There has been significant research on the fatigue failure of overhead line conductors ever since it became evident that Aeolian vibration is one of the major causes of conductor failures in the field (EPRI Transmission Line Reference Book: Wind Induced Vibrations, 2006). Various laboratory set-ups have been used to study the fatigue failure of ACSR conductors but they all point to the mechanism of fretting fatigue. This phenomenon is as a result of the nucleation of micro cracks from the interlayer strand to strand contact points and their propagation and growth to a critical length leading to strand breakage. The elliptically shaped crack nucleation sites, commonly referred to as fretting marks are therefore key to the fatigue failure of the conductor although their influence on fatigue of new conductors is neglected in most of the research conducted. These fret marks come into being during the conductor manufacturing process and their size is dependent upon the net axial force injected into the conductor by the lay/haul and take up capstans as well as the lay ratio selected for each layer.

While international standards on the manufacturing of ACSR conductor such as *BS EN 50182:2001* stipulate that "*the surface of conductor strand shall be free from all imperfections*

*visible to the unaided human eye such as nicks, indentations etc. not consistent with good commercial practice*", unaided observation of the strand surfaces however revealed a series of equally spaced elliptical marks along the strand. The size of these marks varied greatly depending on the manufacturer and also varies from each interlayer contact. In this research, results from the surface characterization of conductor strands using Scanning electron Microscopy, Stereomicroscopy and 3D SEM Stereomicroscopy will be presented for the Tern conductor samples. Fret mark parameters such as length, width, depth, relative depth and eccentricity will be measured and calculated. Empirical relationships between these surface parameters and the conductor parameters such as lay ratios, lay angles and curvatures will be determined.

The interlayer strand to strand contact shall be replaced by a surrogate deformable sphere and rigid flat plane contact pair (Sanders et al, 2010; Hertz, 1882; Johnson, 1985; Kogut et al, 2002, Vu-Quoc, 2000 and Adams, 2000). The sphere radius shall be calculated as being equivalent to the Hertzman equivalent radius (Hale LC, 1999).

Attention is drawn to the establishment of the allowable initial quality of the conductors after manufacturing. 2D nonlinear FEA simulations based on the Hetzian contact mechanics were run to establish the contact forces and mitigations to reduce the size of the marks are presented. Tern conductor samples with varying surface quality were used in this study. Surface characterization of these samples using techniques such as Scanning Electron Microscopy, 3D stereomicroscopy, and stereomicroscopy was employed with emphasis on the measurement of the surface flaw. Energy dispersive spectroscopy (EDS) was used to establish the elemental composition on the fret marks.

The conductors were then exposed to a maximum of 50 million fatigue cycles unless there were two strand breakages. A post mortem Fractography inspection of the conductor in the suspension clamp region was carried out to confirm if the fatigue cracks emanated from the initial flaws (fret marks). The lengths of the initiated cracks were measured using the SEM and FEGSEM for each sample. These crack lengths were used to approximate the crack growth rate for each conductor sample and in the estimation of the maximum allowable flaw size.

### 1.1 Aluminium Conductor Steel Reinforced (ACSR)

ACSR is the most common option for bare overhead power line conductors because it combines the advantages of mechanical strength from the steel core and high conductivity from the aluminium outer layers. There are various sizes, steel ratios and stranding configurations for ACSR conductors. A brief description of the Tern conductor is given above.

Figure1-1 shows some of the ACSR conductors. Choosing which conductor is appropriate for a given application depends on specific electrical and mechanical requirements.

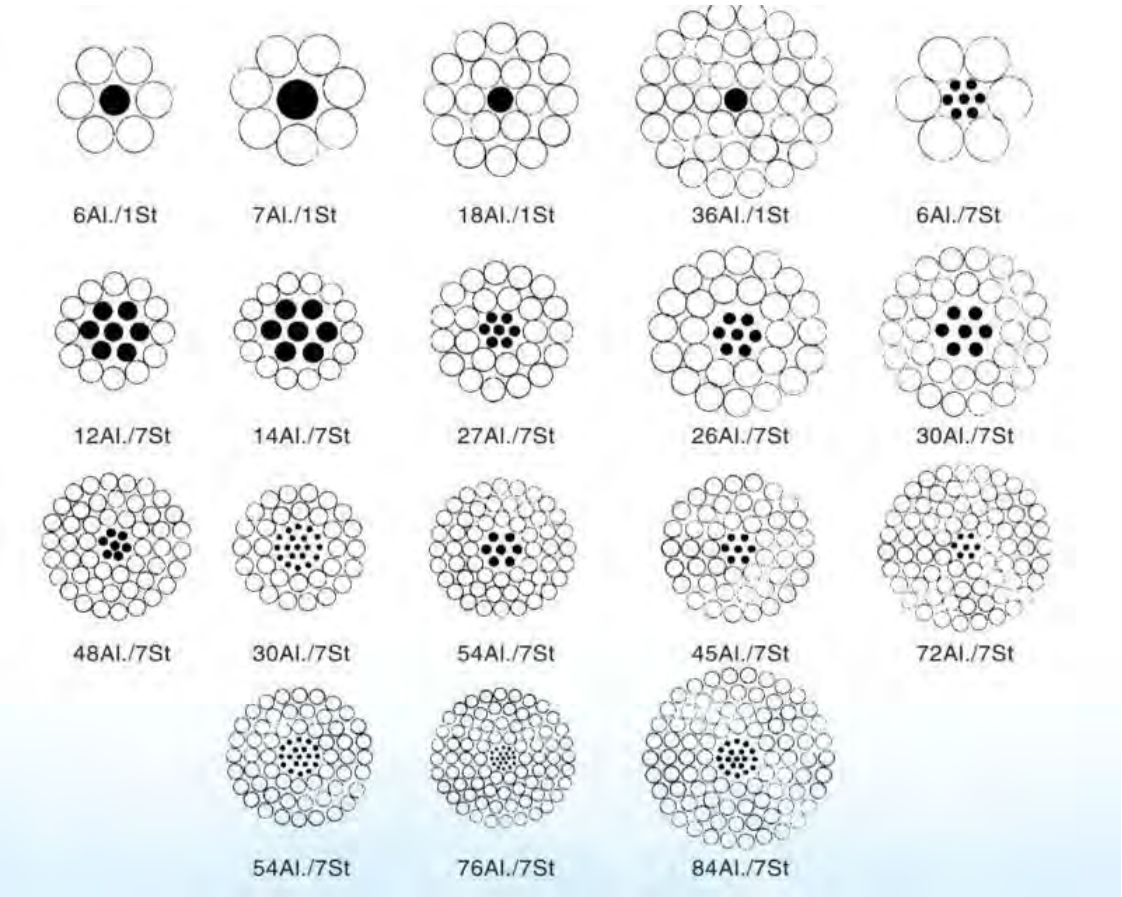


**Figure1-1: Examples of ACSR conductors**

As per IEC 60889, the aluminium wires shall be made from hard drawn Aluminium (Electrical conducting grade) in H9 condition. IEC 61089 requires that 1350 aluminum is used in the manufacture of ACSR conductors.This is at least 99.5% pure aluminium. Most of the conductors used at transmission voltage level (132kV and above) have two to three aluminium wire layers with multilayer conductors being employed for high current application. The steel used in the manufacture of the core is made of regular steel (S1, according to IEC 62219), high tensile steel (S2) or ultra-high tensile steel. The steel wire is galvanised with either class one or two to prevent corrosion.

## 1.2 Manufacturing Process of ACSR Conductors

The manufacturing of transmission line conductors starts with aluminium wire drawing in the wire breakers. Aluminium rods of diameter greater than 9.45mm are progress drawn into the

required reduced diameter by passing it into a series of dies. The drawn wire is wound on the bobbins by the spooling machines. The bobbins are then feed into the stranding machines.

After the wire drawing process, stranding is the next process. Stranding machines come in various forms but all operate on the same principle, which is a combination of two motions;

a) Rotation of the tubular body
b) Feed motion produced through the haul off unit.

### 1.2.1 Rotation of tubular body

The rotary motion of the tubular body is produced by a motor which transmits power via a gear coupling. This gear coupling is adjustable and can be used to reverse direction in order to achieve the alternate lay. Two gears designated *A* and *B* are used in speed adjustment. They are constrained by the sum of their diameters. Therefore gears with any number of teeth can be used for this combination but the sum of their diameters must remain constant. The stranding body which produces the rotary motion carries bobbins full of aluminium wires in its cradles which are locked into position by the pintles. To control the unwinding of the wires from the bobbins, dynamometers are fitted on each spindle of the bobbin for tension (braking) purposes. The dynamometers have a setting range of 10-15kg for machines used for multilayer conductor winding. Figure1-2 shows a stranding machine.

The Schematic in figure 1-3 shows the arrangement of the gears A and B for one cage of a Cortinovis-Bergamo machine used at Aberdare's Port Elizabeth Plant. In general the stranding machine will have a number of cages equal to the number of layers required in the conductor. To manufacture a three layer conductor such as a tern, you will need at least three (03) cages in a stranding machine. Each cage will carry the number of bobbins equal to the number of wires in that layer. Each cage will have a different set of gears A and B selected according to the required conductor parameters. The selection of gears A and B is also dependant on the selected gears for the lay capstan which will be explained in the subsequent paragraph. The Sum of the radii of the gears A and B is 60cm. In between gear B and the drive shaft is another combination of gears used for rotational direction reversal. The direction of rotation will be set as per the design of the conductor in terms of lays.

The rotation speed is limited to a maximum speed of 180 and 120 rev/min for Aluminium and copper stranding respectively.

**Figure1-2: Stranding Machine**

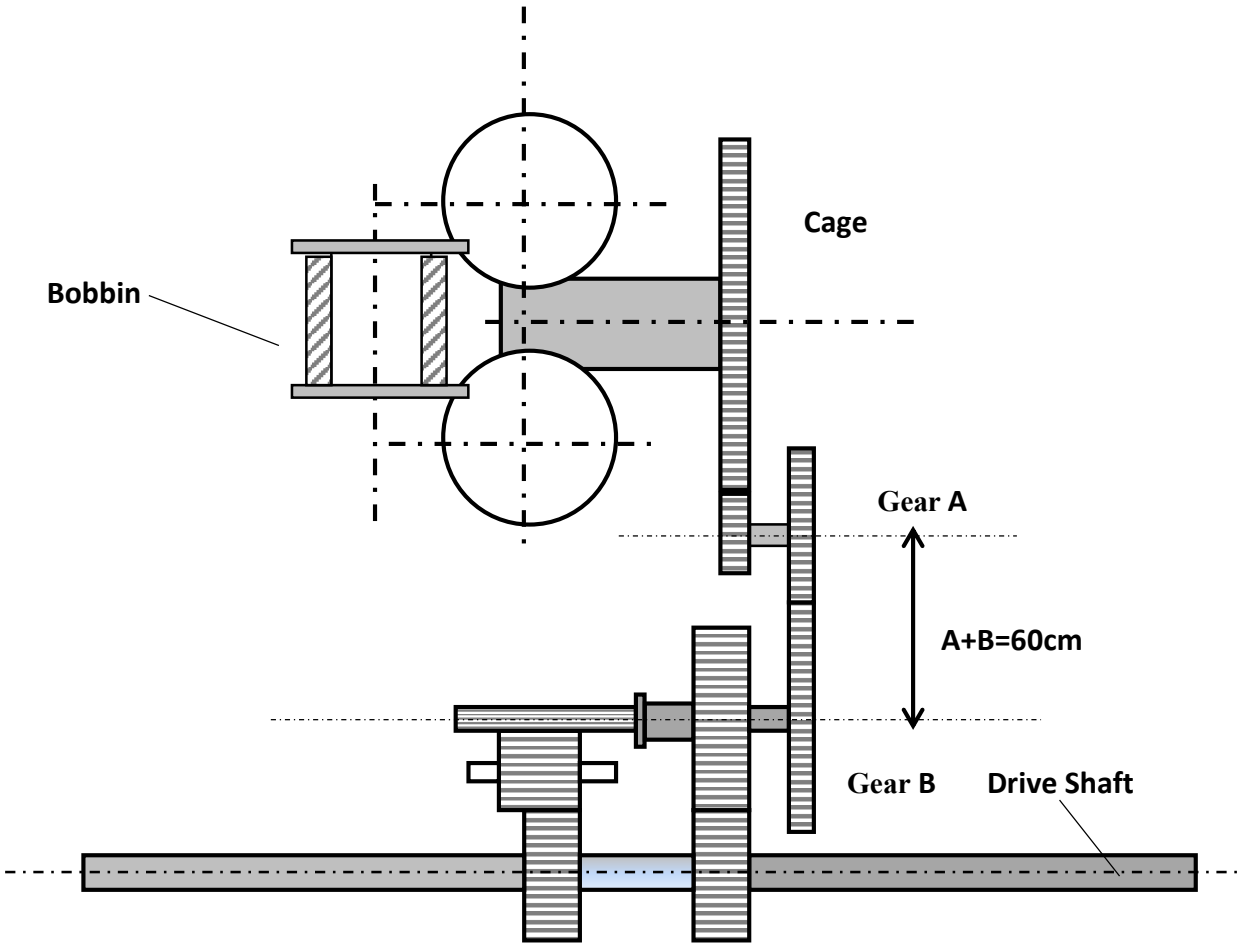


**Figure 1-3: Position of gears A and B relative to Drive Shaft**

### 1.2.2 Feed motion

The haul off capstan or cartepille is equipped with a gear box. By selecting the proper levers shown on the haul-off capstan table, you may choose the nearest lay desired. You may also select a lay necessary for a certain type of rope. The haul-off capstan is a 36 speed gear box comprising of one 12 speed and one 3 speed gear box. Figure 1- 4 shows the bulls at the haul off capstan. The different lays obtained for different gear selections are shown in table 1-1 for the gears A and B and the levers on the 36 speed gearbox.


**Figure 1-4: Bull wheels**

**Table 1-1: Stranding Machine Gear Configuration (Source: Cortinovis Machines Operating Manual)**

| Stranding lays= 204.91*(36 Speed Gear)*A/B | | | | |
|---|---|---|---|---|
| 36-Speed Gearbox | | A/B | | |
| 3-Speed | 12 Speed | 30/30 | 33/27 | 37/23 |
| 8 | 1-5 | 39.80 | 48.70 | 64.10 |
| | 2-5 | 42.40 | 51.90 | 68.20 |
| | 3-5 | 45.20 | 55.20 | 72.70 |
| | 4-5 | 48.10 | 58.80 | 77.40 |
| | 1-6 | 51.60 | 63.10 | 83.10 |
| | 2-6 | 55.00 | 67.20 | 88.50 |
| | 3-6 | 58.60 | 71.20 | 94.20 |
| | 4-6 | 62.30 | 76.20 | 100.30 |
| | 1-7 | 66.40 | 81.20 | 106.80 |
| | 2-7 | 70.70 | 86.40 | 113.70 |
| | 3-7 | 75.30 | 92.00 | 121.10 |
| | 4-7 | 80.20 | 98.00 | 128.90 |
| 9 | 1-5 | 84.40 | 103.10 | 135.70 |
| | 2-5 | 89.90 | 109.90 | 144.50 |
| | 3-5 | 95.70 | 116.90 | 153.90 |
| | 4-5 | 101.90 | 124.50 | 163.80 |
| | 1-6 | 109.40 | 133.70 | 175.90 |
| | 2-6 | 116.50 | 142.40 | 187.30 |
| | 3-6 | 124.00 | 151.60 | 199.50 |
| | 4-6 | 132.00 | 161.40 | 212.30 |
| | 1-7 | 140.70 | 171.90 | 226.20 |
| | 2-7 | 149.80 | 183.10 | 240.90 |
| | 3-7 | 159.50 | 194.90 | 256.40 |
| | 4-7 | 169.80 | 207.50 | 273.00 |
| 10 | 1-5 | 181.60 | 221.90 | 292.00 |
| | 2-5 | 193.40 | 236.30 | 310.90 |
| | 3-5 | 205.90 | 251.60 | 331.00 |
| | 4-5 | 219.10 | 267.80 | 352.40 |
| | 1-6 | 235.40 | 287.70 | 378.50 |
| | 2-6 | 250.60 | 306.30 | 403.00 |
| | 3-6 | 266.90 | 326.20 | 429.10 |
| | 4-6 | 284.10 | 347.20 | 456.80 |
| | 1-7 | 302.60 | 369.90 | 486.60 |
| | 2-7 | 322.30 | 393.90 | 518.20 |
| | 3-7 | 343.10 | 419.30 | 551.70 |
| | 4-7 | 365.30 | 446.40 | 587.30 |

The take up stand accommodates the collecting bobbins. This unit is provided with a two speed gear box. The 2 speed gear box has a slow speed gear box for bobbins or drums of large diameter and a high speed for drums of smaller diameter.

If it is required to setup a conductor layer with a lay length of 292mm, the designer will look up in table 1-1 and select the following; gear 10 on the 3 speed gear box, gear 1-5 in the 12 speed gear box and set the gears A and B to 37 and 23 respectively. The resulting lay length will however be longer than the desired 292 mm because the conductor will be subjected to a pulling force which will stretch the lay length. By experience, the cable designer would usually set a gear combination which will give a slightly smaller lay length in the table. This lay length will stretch and get to the desired lay length at the bull wheels.

The drive line is in addition provided with a ferodo lined clutch. This frictional type of clutch is adjustable and can be a set to the power transmission value suitable for the tension you want to achieve in the conductor between the haul off capstan and take-up stand. The collecting drums have specified factors for the conductors. For the ACSR conductors, the minimum bending factor is 35 times the conductor diameter.

### *1.2.3* Greasing of Conductors

The greasing of a conductor is currently done on request. The customer will request for greasing of a conductor by Aberdare and they will specify the case of greasing required. Eskom only requires case 4 greasing for most of their lubricated conductors. Four cases exist for the greasing of the conductors;

- **Case1**:- In this case on the core is lubricated. The mass of grease per unit length $v_g$ can be expressed as;

$$v_g = \frac{1}{4}\left({D_o}^2 - n_s {d_s}^2\right) \quad (1)$$

- **Case 2**:- In this case are the layers except the outer one are lubricated. The volume per unit length is given as;

$$v_g = 0.25\pi\left(D_0 - 2{d_a}^2\right) - (n_a - n_0){d_a}^2 - n_s {d_s}^2 \quad (2)$$

- **Case 3**:- Case is the most expensive type of lubrication requiring the greasing of all layers including the outer one. The volume per unit length of the grease is given as;

$$v_g = 0.25\pi({D_0}^2 - n_a {d_a}^2 - n_s {d_s}^2) \quad (3)$$

- **Case 4**:- Case 4 lubrication only leaves the outer layer surface unlubricated. It is the lubrication type commonly requested by Eskom.

$$v_g = 0.125n_0(D_0 - d_a)^2 \sin\left(\frac{360}{n_0}\right) - 0.125\pi(2n_a - n_0 - 2){d_a}^2 - 0.25\pi{d_s}^2 n_s \quad (4)$$

$D_0$ is the outer diameter of the core
$n_s$ is the number of still wires
$d_s$ is the diameter of the steel wires
$D_0$ is outer diameter
$d_a$ is diameter of aluminium wire
$n_a$ is number of aluminium wires
$n_o$ is the number of wires in the outer layer

With the density of grease equal to 0.87g/cm$^3$ and a fill factor of 0.8, the mass of grease per unit length is given by;

$$M_g = 0.8v_g\rho \; where \; \rho \; is \; the \; density. \quad (5)$$

Some standards on greasing express the mass unit length in terms of a constant *(k)* and the diameter of the aluminium wires. This is expressed as;

$$M_g = k{d_a}^2 \quad (6)$$

### 1.3 Aeolian Vibrations on Overhead Transmission lines

The vibration caused by a fluid passing over a body is known as flow induced vibration. A lot of engineering structures can be seen to vibrate as a fluid flows over them. Some of the examples of the structures which vibrate include; electric transmission line conductors, tall chimneys, fuel rods in nuclear power plants etc. (S. Rao., 2004). In transmission lines, wind induced vibrations are predominant and would sometimes reach amplitudes which are twice the diameter of the conductor. The theory of vibration caused by laminar air flow was originally developed by T.H Karman (https://en.wikipedia.org).These theories have been applied to transmission lines and the resulted validated using both experimental and simulation tools.

Aeolian vibrations are caused by changes in the air pressure caused by laminar wind flowing over the conductor. This air flow creates forces perpendicular to the direction of the wind and leads to the vertical motion of the conductor. The conductor diameter and velocity of the laminar wind are related by the Reynolds number and the viscosity of the air as shown in the equation (7);

$$Re = \frac{DV}{v} \tag{7}$$

Where:

Re = Reynolds number

D= Diameter of the Conductor

V=Wind speed

$v$= Viscosity coefficient

Turbulent flow can appear for a wide range of values of Re.

The frequency of the turbulent flow ($F_w$) is a function of the wind speed, the conductor diameter (EPRI Transmission line Reference Book: Motion Induced Vibrations, 2006) and the Strouhal number, so that:

$$F_w = \frac{Sv}{D} \tag{8}$$

Where:

S = Strouhal number

$F_w$ =Frequency of the turbulences

In the turbulence frequency region, the Reynolds number, $R_e$ is greater than 1000.

For circular conductors the value of the Strouhal number equals 0.2 (S.S. Rao, 2004) (EPRI Transmission line Reference Book: Motion Induced Vibrations, 2006 quotes 0.18). There exists a velocity where the frequency, $F_e$ (Vortex shedding frequency) is equal to the resonance frequency of the conductor. This critical velocity ($v_r$) is given by:

$$v_{cr} = \frac{F_e D}{s} \tag{9}$$

Figure 5-1 below shows a transmission line in open space. Because the wind flow will be laminar below the critical (transitional) velocity, the line is susceptible to Aeolian vibrations.

**Figure 1-5: Power transmission line**

Figure 1-6 shows wind flowing over a cylindrical object such as a transmission line conductor. The harmonically varying lift force (F (t)) acting on the object is given by equation 10.

$$F(t) = \frac{1}{2} c\rho V^2 A sin\omega t \qquad (10)$$

Where:

A is the projected area of the conductor perpendicular to the direction of V

V is the velocity of the wind

$\omega$ is angular frequency

t is the time

c is a constant which is equal to 1 for cylindrical objects

**Figure 1-6: Vortex shedding in cylindrical objects**
**Source: http://www.rpi.edu/dept/chem-eng**

During the designing of cylindrical objects which will be exposed to wind vibration, the following points are worth noting;

1. The magnitude of the force exerted on the cylinder (F) is less than the static failure load at any particular instant
2. Even if the resulting amplitude of the vibrations is small, the frequency of oscillation (f) should not cause fatigue failure during the expected life of the conductor
3. The vortex shedding frequency does not coincide with the natural frequency of the line to avoid resonance

In overhead power lines, the Aeolian vibrations are controlled by means of damper, the most common of which is the Stockbridge damper. Transmission line conductors fail by fretting fatigue.

## 1.4 Problem statement

Aluminium conductors such as the ACSR-Tern are composed of aluminium strands, alternately wound on a steel core. During manufacturing of the conductors, a balance has to be struck on how tight you wind strands of different layers on onto one another. The following serious problems affect the manufacturing companies during the manufacturing process of the ACSR conductors;

(i) **If the aluminium strands are wound too loose**, the conductor strands tend separate from the central core, a condition known as the '***bird cage'***. This phenomenon is undesirable as it results in loss of mechanical strength as well as corona.

(ii) **If the aluminium strands are wind too tight**, then ***fretting marks*** will inevitably appear on the surface of the conductor strands. If the 'bird cage' phenomenon mentioned above is to be avoided then the fretting marks in question become certain.

Many experiments have being conducted on the fatigue performance of transmission line conductors and guidelines on how these tests should be carried out have been formulated. Despite the many experiments conducted and results documented, there has never being any research which has tried to address the effects of the fretting marks on the fatigue life of the conductor. It is assumed in the fatigue life experiments that the dents have no effect on the fatigue performance of the conductor.

This research therefore took a different approach by taking these dents into consideration when investigating the fatigue life of a given conductor. Whether these marks have any effect on the fatigue life of the conductor was deduced and the effect was established.

## 1.5 Objectives

Transmission lines generally have very long service lives. In some parts of the world conductors installed in the middle $20^{th}$ century are still in existence. With the advent of new materials with a high strength to weight ratio, one would expect the conductors to live even longer. It is therefore imperative that all factors affecting the fatigue life of conductors are researched and their effect clearly understood.

The aim of this research is therefore to determine the maximum flaw that is acceptable during manufacturing of the conductors. This maximum size must be avoided without causing bird caging. The research will therefore look at both the conductor-clamp and inter-strand fretting fatigue. The focus was therefore, on what size of indentations would affect the desired life of the conductor.

While looking at this trade-off between the amount of winding, indentation of fretting marks and the bird cage phenomenon, the following objectives were to be attained;

(i) Determine the effect of the variation of the lay ratio on the geometry and size of the fret marks

(ii) Carry out nonlinear contact mechanics analysis to determine the contact parameters such as; Von Mises stress, normal contact force, plastic strain etc.

(iii) Develop an inner conductor model to be used to establish the tension in the conductor which would caused the observed indentation size during manufacturing

(iv) Establishment of the effect of the fretting marks on the fatigue performance of the transmission line conductor (ACSR-Tern).

(v) Quantify the effect of a given geometry of dent on the fatigue life of transmission line conductors.

(vi) Determine the elemental composition on the surface of the fret marks and how it changes with fatigue cycles

(vii) Determine the maximum allowable amount of indentation on the conductor strands which will allow an economical operation of the line. This will be used as a baseline for discarding or accepting a given manufactured conductor for a certain application.

## 1.6 Project justification

Overhead electrical power transmission line networks are becoming more and more complex has the world's ravenous appetite for energy increases. Longer lines are now common place and increased interconnectivity is inescapable in order to achieve the reliability of supply which is promised by most of the power suppliers. This is a direct translation into huge investment costs into these assets and hence the manufacturing quality and maintenance strategy of the conductor which accounts for 40% of the initial investment cost, will significantly impact on the net return on these assets. If for instance a line with a certain amount of indentation is procured and put in service and just lasts long enough to pass the warranty, the utility company will make losses by firstly replacing the line and by losing the connection to the customers. In the same vain, a lines engineer might see a crack or dent on the conductor and become overwhelmed to consider replacement when they could be just enough useful life left.

With the objectives of this research achieved, informed decision would be made by management when procuring and replacing transmission line conductors resulting in more effective asset management, profitability and security of supply.

# 2. Fretting Fatigue

Major design aspects for high voltage transmission lines are firstly of electrical concerns, as the power to be transmitted or the transmission losses. However, mechanical or metallurgical performance ranks high among the technical parameters in overhead transmission line design. Indeed it is important to be able to predict lifetime of conductors in order to ensure a dependable distribution of electricity at a low cost. The fundamental cause of fatigue failures of the cables is the cyclic bending stress imposed upon conductor by Aeolian vibrations (Cigre, Task Force B2.11.07 – Draft Version October 2006). At singular points of the conductor where motion is constrained against transverse vibration, more frequently at suspension clamps but also at spacer-damper device or hardware clamps, bending causes the strands of the conductor to slip relative to each other. The friction forces combined to the relative motion cause fretting at inter strand and clamp contacts. Once an initial crack is induced from the fretting mark surface, it may lead to the rupture of the wire and eventually to the complete breakdown of a conductor.

Even though the presence of fretting in conductor fatigue is a well-known phenomenon, fretting fatigue is not understood enough yet to allow the prediction of the life of a conductor-clamp system by the solution of a mathematical model when knowing the mechanical and physical properties of the wires (Cigre, Task Force B2.11.07 – Draft Version October 2006). The standard method of evaluation still remains to perform experimental tests on a case by case basis.

A state of the art on the effect of fretting fatigue on the endurance capability of conductors has recently been presented in a report prepared by GREMCA at Laval University (Dalpé et al., 2003). Considering the importance of the phenomenon for the study of fatigue endurance capability of conductor/clamp systems, the subject is presented in this chapter. After a brief description of the mechanism of fretting, a complete review of the literature tackling its importance in cable fatigue is presented below.

## 2.1 Mechanism of Fretting Fatigue

Fretting fatigue is a contact damage phenomenon that takes place when a fixed structural member is submitted to a surface micro slip associated with small-scale oscillatory motion on the order of 20-100 μm (Cigre, Task Force B2.11.07 – Draft Version October 2006). It is often responsible for unexpected fatigue failures and limits components life in aeronautical

structures and common industrial machinery such as steam and gas turbines, cables, bolted plates, shaft keys and bearings.

A vast amount of research work has been published on fretting fatigue. Fretting is complex (Vincent et al., 1992, Waterhouse, 1992, Hoeppner, 1994, Mutoh, 1995) since it is influenced by a number of factors including the normal contact load, the amplitude of relative slip, friction coefficient, surface conditions, contact materials and environment. The fretting fatigue process is also recognized as the result from a competition among wear, corrosive and fatigue phenomena driven by both the micro slip at the contact surface and cyclic local stresses.

The mechanism of fretting damage of aluminum material involves several stages of evolution (Hoeppner, 1994). At the beginning a surface oxide film is removed and once done bare surfaces in contact start to rub against each other. At the same time the surfaces tend also to adhere to each other forming weld junctions which will be broken by the relative movement. This process forms the accumulation of wear dust between the surfaces. Surface plastic deformation, change in surface chemistry and formation of oxide aluminum and wear product will increase with more fretting cycles.

The thin and brittle layer of aluminum oxide consists in $Al(OH)_3$ structure. As this oxide is more voluminous than the aluminum metal itself, it may provoke nucleation of grain-size crack with the help of contact stresses. Initiation of surface microcracks is then unavoidable. If the slip amplitudes are large enough the small cracks will be wiped out and contribute to create more fret debris without any possible dangerous propagation cracks. That is a typical fretting wear mechanism. But if the microcracks can propagate below the oxide surface into the bulk material then we get a fretting fatigue process. As the crack grows deeply the influence of the bulk stresses predominate until the complete fatigue failure of the material.

Many theories have been proposed, some well supported by laboratory tests simulating fretting fatigue, to account for the effects observed in this damage process. One may retain that the stresses reach a maximum at the edge of contact (stick-slip area) where cracks are mainly initiated. It is impossible here to attempt a complete study of the mechanism of fatigue. It suffices to mention a few researchers in that field: Waterhouse (1992), Nowell and Hills (1987), Mutoh (1995), and Johnson (1985).

In addition to the stress analysis and calculations in the bodies in contact, the fretting fatigue problem is often approached empirically. For example several researchers (Mindlin, 1949, Kuno et al., 1989, Vingsbo and Soderberg, 1988, Zhou and Vincent, 1995) used fretting maps concepts for controlling the fretting fatigue damage in practice. A “running conditions fretting map” which describes the fretting regime vs. the fretting conditions (load and displacement),

and a “material response fretting map” that defines the domains of damage (no degradation, cracking, particle detachments) vs. fretting conditions were developed. Comparing the maps one should evaluate correctly the effect of the contacts and of the external loading in fretting fatigue. The mixed fretting regime has been identified to be the most dangerous regime for crack nucleation and propagation (Kuno et al., 1989) and is characterized by a particular type of running conditions fretting map i.e. a variation in the shape of the “tangential load displacement” loops. (Cigre, Task Force B2.11.07 – Draft Version October 2006)

# 3. Research Methodology

The research methodology was divided into five (05) key areas;

1. Characterization of the fret marks
2. Energy dispersive spectroscopy (EDS)
3. Fatigue testing
4. Fractography
5. EDS on fatigue tested sample

The procedures and standards employed in each of these stages are explained below.

## 3.1 Characterization of fret marks

### 3.1.1 Sampling and surface preparation

Sampling of the strands was done as per SANS 182-2. For a forty five(45) aluminum wire conductor, this will result in sampling 2, 3 and 4 wires in the inner, middle and outer layer respectively. Table 3-1 below is an extract from SANS 182-2.

**Table 3-1: Sampling of strands (Extract from SANS 182-2)**

| Number of wires in conductor | Number of center wires | No. of strands from 1st Layer | No. of strands from 2nd Layer | No. of strands from 3rd Layer | No. of strands from 4th Layer |
|---|---|---|---|---|---|
| **7** | 1 | 3 | - | - | - |
| **19** | 1 | 2 | 3 | - | - |
| **37** | 1 | 2 | 3 | 4 | - |
| **61** | 1 | 2 | 3 | 4 | 5 |

### 3.1.2 Sample preparation

The samples were cleaned with acetone to remove all dirt and contaminants. Five fret marks were then randomly selected per strand on both the bottom and upper contacting surface for analysis giving a total of ten marks per strand. A strand of length of about 1.5 times the layer

length of the outer layer was randomly selected and fret marks observed under a stereomicroscope were also selected at random from the strands. The lay cylinder diameter, lay length and strand radius of each layer were also measured as per the recommendation from IEC 61089 and SANS 182.

The samples were first examined with a stereomicroscope to identify the points of interests. The sample was then cut into smaller specimens of about 1cm maximum length. These specimens were then mounted on stubs with a double sided tape before being mounted into the SEM. Figure 7 below shows the specimens before being inserted into the SEM.

**Figure 3-1: Specimens mounted on stub for SEM**

### 3.2 Stereomicroscopy

Stereomicroscopy was used in the measurement of the major and minor axes of the fret marks. The Stereomicroscope used is the AZ-TE80 Ergonomic trinocular Tube 80. The magnification of this optical type instrument is given as:

$$Total\ Magnification = Zoom\ magnification \times Objective\ magnification \times eye\ piece\ magnification$$

Because the surface of the strand is round, it is impossible to get the entire outline of the fret mark in focus at any particular instance. Therefore the Z-stack technique with 5 stages was used to get a fully focused reconstructed image, using the NIS Element software. The major and minor axes and the surface area were measured on this re-constructed image. The Z-stack procedure is summarized below:

1. Select the lowest of highest point of the sample by moving the stage up or down or using the main focus
2. Select the starting point of the stacking, click on the Z-stack icon on your screen
3. Two images appear, one with live image and the other with a frozen image
4. Click on the play button on your NIS element software screen
5. Click next
6. Turn the focus to second point on sample, try as much as possible to turn focus through equal divisions. The number of divisions equals the number of images to be stacked
7. Ignore the Z-step tab
8. Click finish after the last focused image
9. Select the align sequence by clicking on the drop down menu
10. Select create focused image
11. Save as TIFF file
12. Re-open image and burn in scale, then re-save
13. End

Figure 3-2 shows the images obtained without using Z-stack and when Z-stack is applied.

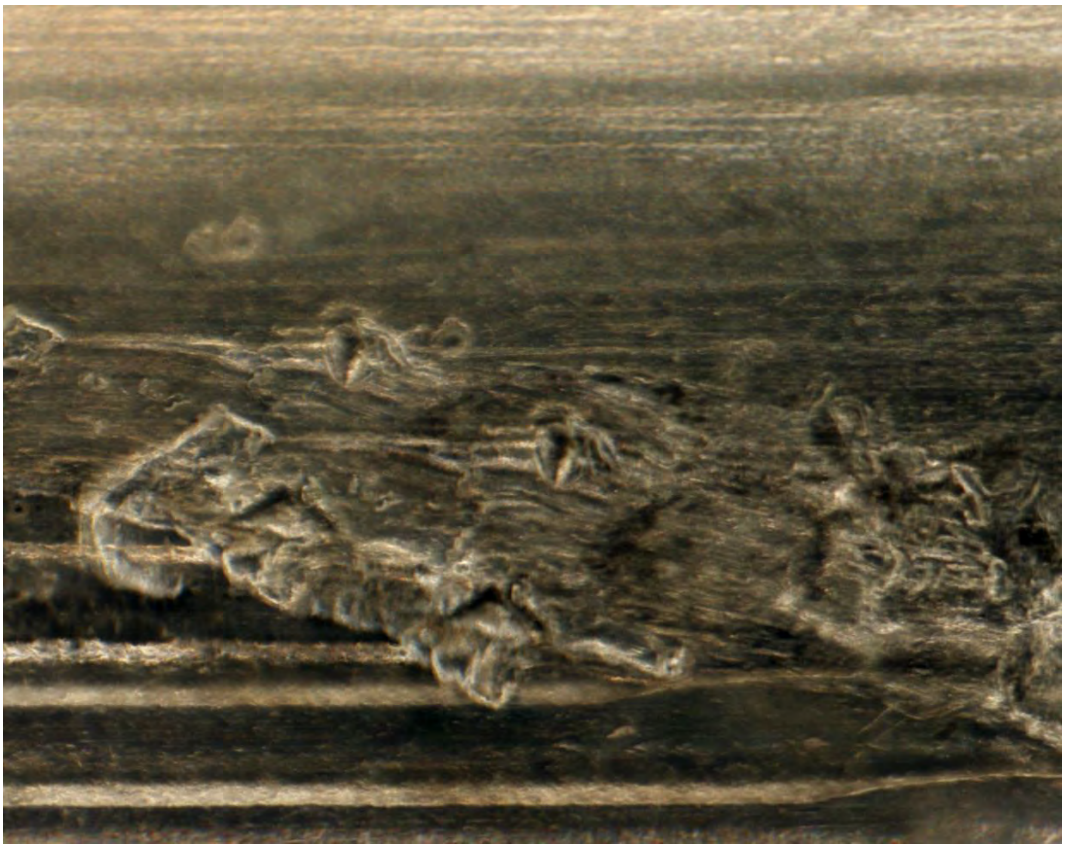

**(b) Z-Stacked Image**

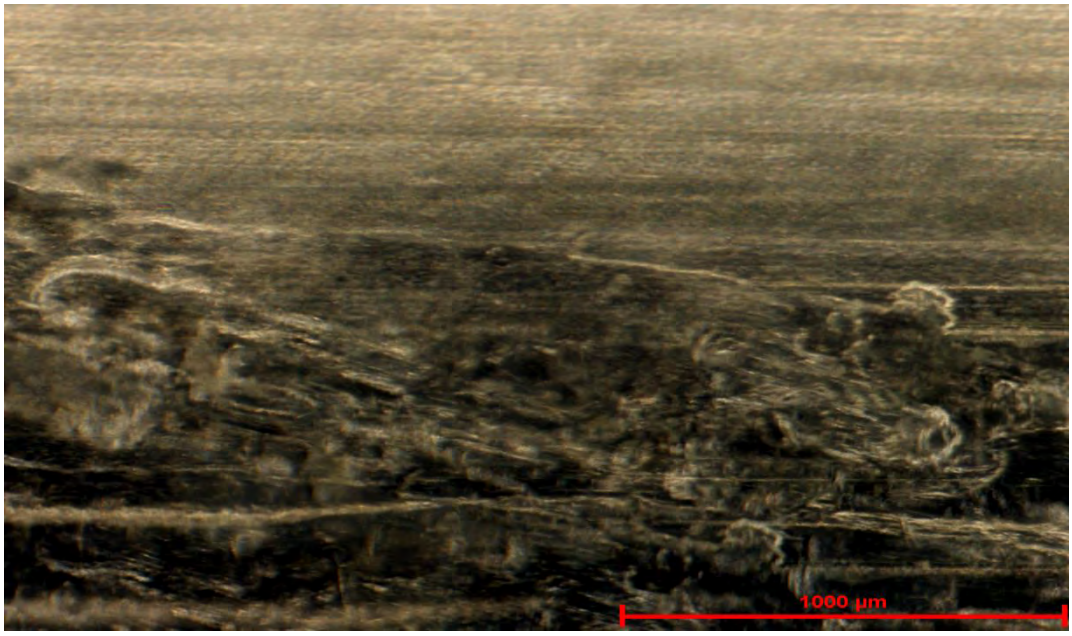


**(b) Un-staked image**

**Figure 3-2: Images from stereomicroscopy, (a) Z-staked (b) Ordinary image**

As can be seen from these images, without Z-stacking the image obtained is blurred and difficult to use for metrology or analysis. It is therefore, necessary to carry out z-stacking for better imaging.

### 3.3 Scanning electron microscopy and SEM stereomicroscopy

Scanning electron microscopy (SEM, Centaurus Detector model) was used to confirm the measurements obtained from the stereo-microscope and also for measurement of the depth. The 3D stereomicroscopy SEM technique was used for the recovery of the third dimension (depth). SEMs capture a 2D image only from which the third dimension (height) cannot be obtained. To measure the third dimension, a method which mimics the operation of the human eye was employed. The method requires a eucentric tilting of the sample about one axis while keeping all other settings constant. The technique requires two images for analysis, the normal and the tilted image respectively. While the human eye is said to operate within 5-6 degrees, the tilting angle in SEM stereomicroscopy is kept lower to avoid losing reference points and having too blurred an image after tilting. Both images must be analyzed at the same magnification and working distance. The theory behind this technique is illustrated in figure 3-4 below and figure 3-3 shows the SEM used.

**Figure 3-3: Scanning Electron Microscope (SEM)**

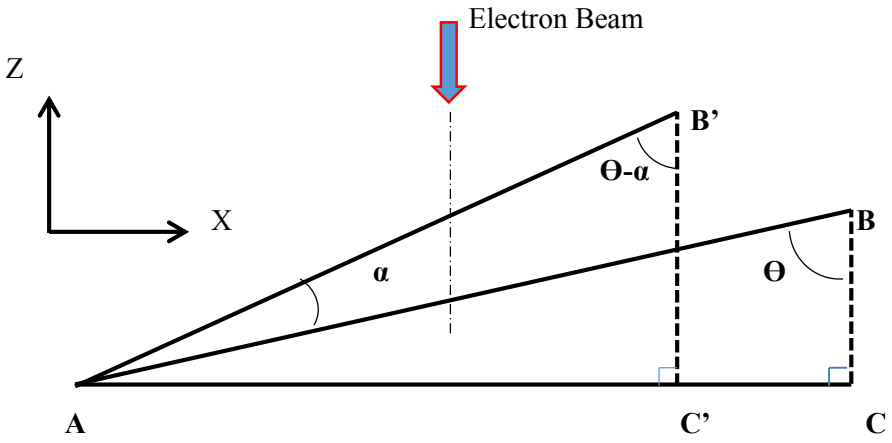


**Figure 3-4: 3D Stereomicroscopy**

The projection of line AB on the focal plane will be AC. After tilting the sample an angle α, point B moves to B' while point A remains still. This is tilting about the Y axis. Then the projection of line AB' on the focal plane will be changed to AC', which is observed as the displacement of point B in two stereo pair images. This is called parallax movement. From Figure 3-4, the following geometrical relationships can be derived:

From the sine rule of triangles and trigonometrical rations:

$$\frac{L_{AC}}{\sin\theta} = \frac{L_{AC'}}{\sin(\theta-\alpha)} \quad \text{and} \quad \frac{L_{AC}}{L_{BC}} = \tan\theta \tag{11}$$

$L_{AC}$ and $L_{AC'}$ can be measured on the SEM images and the tilt angle is a known value. The relative height $L_{BC}$ can be expressed as:

$$L_{BC} = \frac{L_{AC}\cos\theta - L_{AC'}}{\sin\alpha} \tag{12}$$

When the tilt angle is small, Eq. (12) can be simplified as:

$$L_{BC} = \frac{L_{AC} - L_{AC'}}{2\sin(\frac{\alpha}{2})} = \frac{P}{2\sin(\frac{\alpha}{2})} \tag{13}$$

Where, P is called the Parallax value.

Figure 3-5 below shows a cross section of the strand and the measured depth.

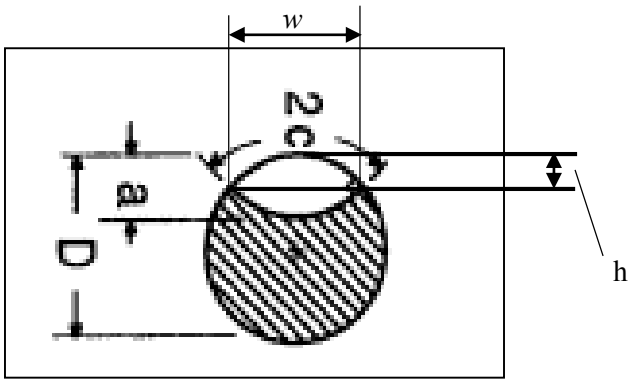


**Figure 3-5: Fret mark depth**

From the figure 3-5, it can be shown that, h is given by the equation:

$$h = R_w\sqrt{\left\{1 - \left(\frac{w}{2R_w}\right)^2\right\}} \tag{14}$$

Where;

$R_w$ is the radius of the strand

*w* is the width of the fret mark

Figure 3-6 shows some of the micrographs used in third dimension (height) recovery.

The depth,'*d*' measured by the SEM stereomicroscopy is then;

$$d = a - h \tag{15}$$

Where *'a'* is the interference on one strand.

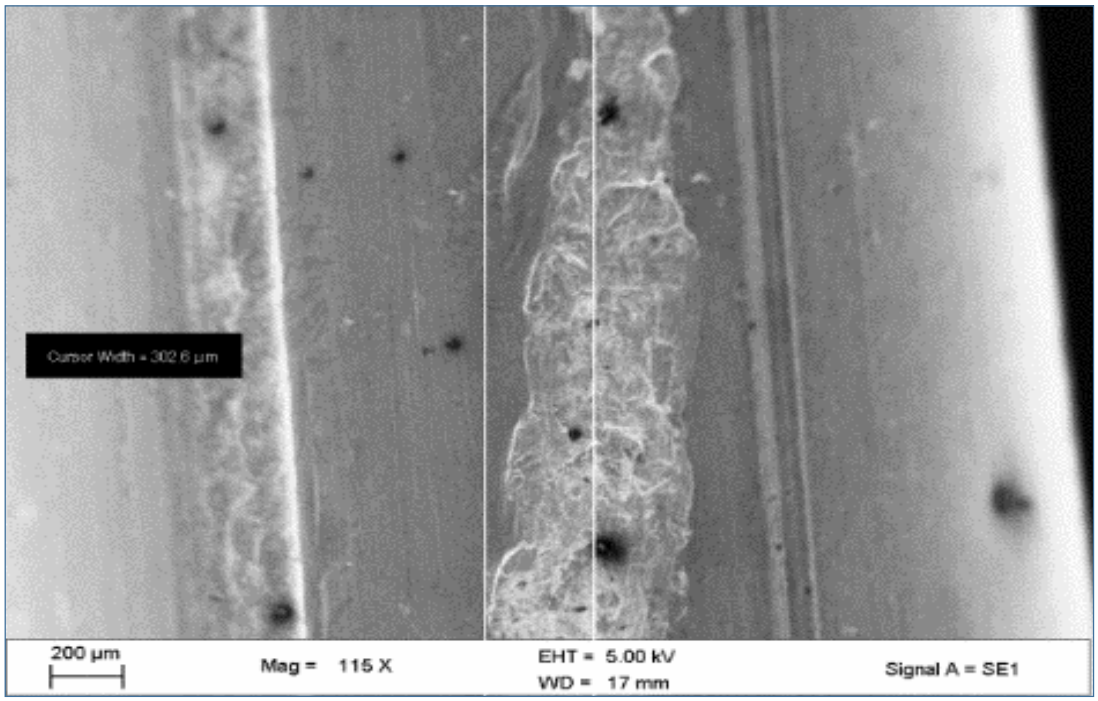


**(a) Original position, 302.6microns**

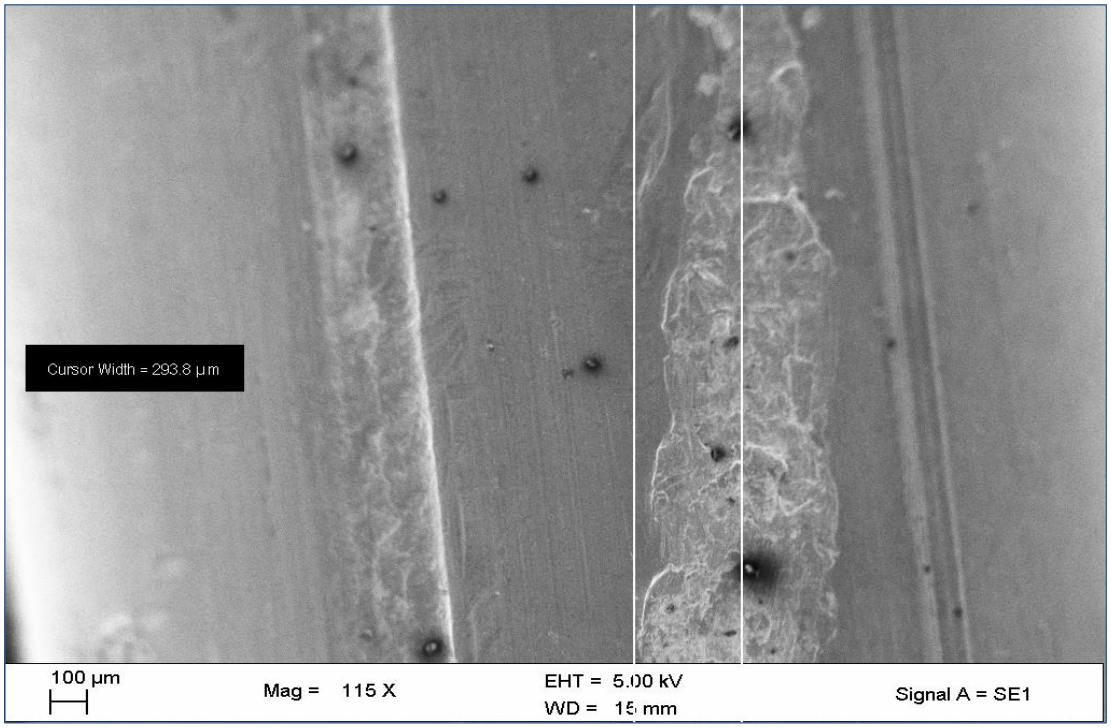


**(b) Tilted position, 293.8micron**

**Figure 3-6: Micrographs used in Depth Measurement**

### 3.4 Energy dispersive spectroscopy

Energy Dispersive Spectroscopy makes use of the X-ray spectrum emitted by a solid sample bombarded with a focused beam of electrons to obtain a localized chemical analysis. All elements from atomic number Z 4 (Be) to 92 (U) can be detected in principle, though not all instruments are equipped for 'light' elements (Z < 10). Qualitative analysis involves the identification of the lines in the spectrum and is fairly straightforward owing to the simplicity of X-ray spectra. Quantitative analysis (determination of the concentrations of the elements present) entails measuring line intensities for each element in the sample and for the same elements in calibration Standards of known composition.

By scanning the beam in a television-like raster and displaying the intensity of a selected X-ray line, element distribution images or 'maps' can be produced. Also, images produced by electrons collected from the sample reveal surface topography or mean atomic number differences according to the mode selected. The scanning electron microscope (SEM), which is closely related to the electron probe, is designed primarily for producing electron images, but can also be used for element mapping, and even point analysis, if an X-ray spectrometer is added. There is thus a considerable overlap in the functions of these instruments.

In this research, EDS was extensively used to determine the elemental composition of the fret mark surfaces before and after the fatigue testing.

#### 3.4.1 Sample preparation

The samples used in EDS analysis, were not cleaned in any way so as to avoid rubbing off any elements form the surfaces. The strand was cut into smaller pieces (less than 1cm long) and fitted onto stubs. The samples where mounted on the stabs using the double sided tape. The stubs were then mounted into the FEGSEM and screwed to prevent them from failing in case of tilting. Eight (08) stubs were loaded in the FEGSEM per cycle. Figure 3-7 shows the microanalysis of the fret mark surfaces.

For each fret mark, at least two points were analyzed for elemental composition and the results from each scan averaged. This was done in order to get a true reflection of the elements present on the surfaces. The report generated with the highest number of elements was used as the reference spectrum. For other spectra with some of the elements not picked automatically, the missing elements were manually picked and then, the percentages calculated.

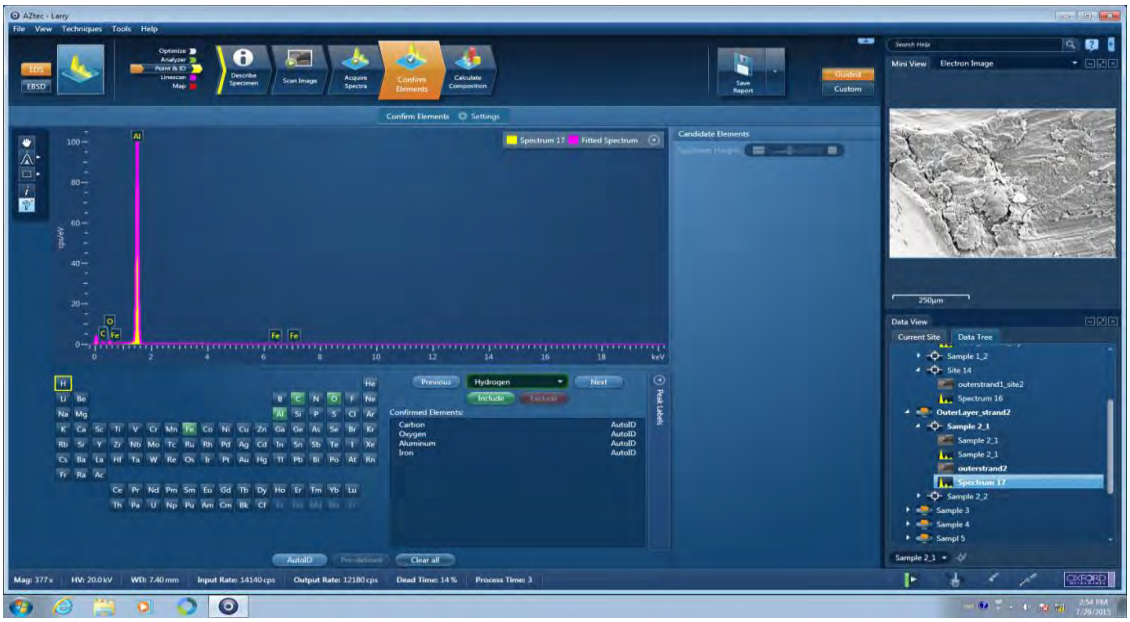


**Figure 3-7: EDS on fret mark surfaces**

Figure 3-8 shows the FEGSEM used for the EDS analysis.

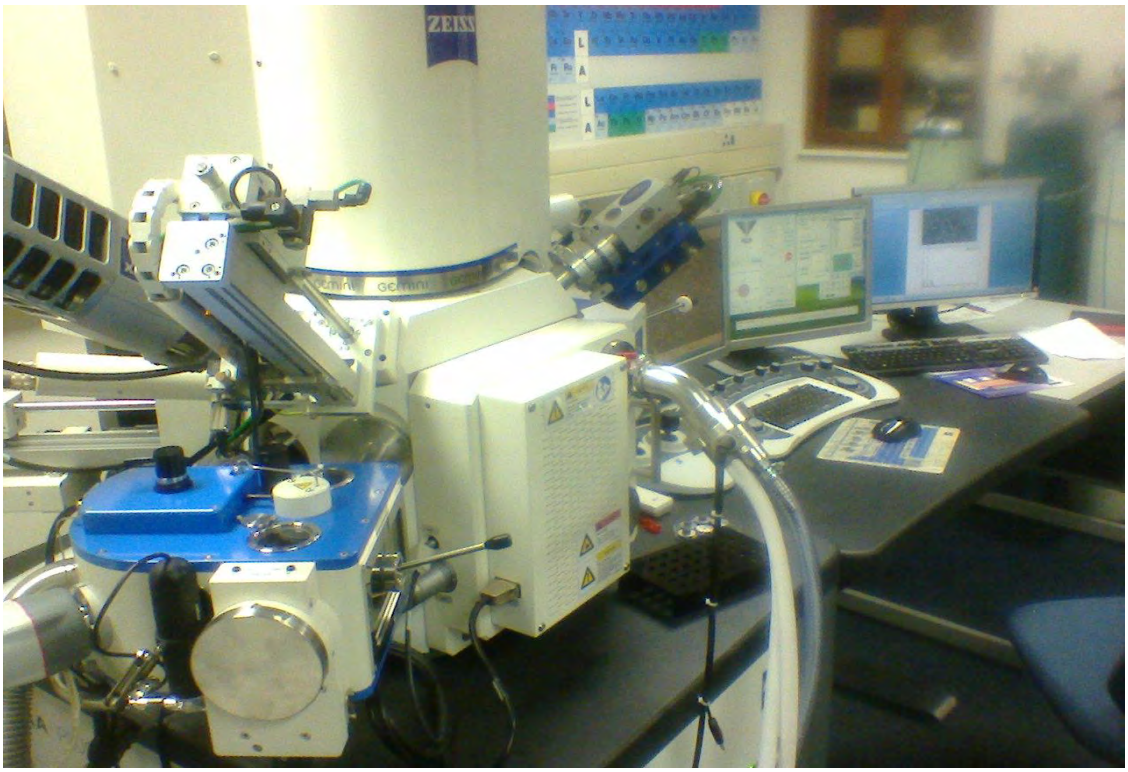


**Figure 3-8: FEGSEM for Energy Dispersive Spectroscopy (EDS) Analysis**

### 3.5 Tensile testing

Before starting the fatigue, the strands of the conductor samples were subjected to a tensile test conducted at preformed line products (PLP). The certificate of the test results is attached in annexure A.

### 3.6 Fatigue testing

The existing test rig of 95m long and suitably designed for the testing of the effectiveness of dampers and conductor self-damping was used for the fatigue tests. The rig is equipped with square faced conductor clamps. For fatigue testing of conductors, the test rig was modified to suit the recommendations given by the following organisations and standards with regards to fatigue testing:

(i) Cigre' Working Group 11, Study Committee B2 Task force B2.11.07
(ii) Electrical Power Research institute(EPRI) Transmission lines Reference Book
(iii) International Electrotechnical Commission (IEC) 62568
(iv) IEEE 563
(v) The Planning, Design and Construction of overheard lines, Eskom Power Series

From all these references the following points were taken into consideration and employed for the design of the test rig;

I. The use of a standard short (salvi) suspension clamp. The suspension clamp was tilted at an angle between 5˚ and 10˚ in order to simulate the conductors exit angle due to sagging at the suspension clamp in actual lines. The rig was designed with the tilt angle set at 7˚. This angle was measured and confirmed with a protractor
II. The distance from the dead end of the conductor to the suspension clamp measured horizontally must not be less than 2m. This is to ensure that the load is uniformly distributed in the conductor strands.
III. The suspension clamp must be restricted from articulation during the tests to avoiding its rocking motion in order to simplify the analysis.
IV. The distance of the point of attachment of the shaker to the conductor must be greater than five (05) free vibrating loops from the suspension clamps to ensure uniform solicitation of the strands in the area where fretting fatigue takes place.
V. The length of the active span of the conductors must be such that the wavelength of the induced waveform is relatively bigger than the length of the clamp.
VI. The frequency of the shaker was chosen such that it excites the resonant mode of a taut conductor.

VII. Characteristic catenary constant of Eskom power transmission lines. The tension was maintained within ±2.5%.

With these conditions taken into consideration and using the following data for an ACSR-Tern conductor, the design parameters for the test rig can be established.

**Table 3-2 ACSR Tern Conductor Standard Parameters**

| Item Description | Unit of Measure | Quantity |
|---|---|---|
| **Ultimate Tensile Stress** | kN | 98.7 |
| Mass per metre | Kg/m | 1.34 |
| Diameter | mm | 27.0 |
| Number of aluminium wires | - | 45 |
| Number of Steel wires | | 7 |
| Diameter of aluminium wires | mm | 3.38 |
| Diameter of Steel wires | mm | 2.25 |
| Modulus of Elasticity of Steel | MPa | 210,000 |
| Modulus of Elasticity for Aluminium(E-grade) | MPa | 70,000 |

The design of the test rig entailed the determination of the following parameters using the data from table 3-2 and meeting all the standard requirements;

(i) Resonant frequency(f)
(ii) Span Length(L)
(iii) Mode of the vibration(n)

These parameters were determined based on bending amplitude of ***0.2mm -0.3mm***.

These quantities are related by the Eq. (16):

$$f_n = \frac{n}{2L}\sqrt{\frac{T}{m}} \tag{16}$$

Where:

$T$ is the Tension

$m$ is the linear mass

The Tension (T) is the Every Days Stress (EDS) in the conductor. This stress is determined based on the conductor unit weight and a design constant called the catenary constant ($C$).

$$C = \frac{T}{w} \tag{17}$$

$$\text{w is the weight per meter of the conductor in } \mathrm{N/m}$$

For phase conductors, Eskom uses a Catenary constant of 1800m. For a tern conductor this will result in an EDS of 23.66kN (**23.97%** of UTS).

Inserting this data into eq. (16) yields:

$$f_n = \frac{n}{2L}\sqrt{\frac{23660}{1.34}} = \frac{66.439n}{L} \tag{18}$$

$$f_n = \frac{66.439n}{L}\ , \frac{n}{L} = 0.9031 \tag{19}$$

The relationship between the wavelength, span and mode of a standing wave is given by Eq. (20):

$$\frac{n}{L} = \frac{2}{\lambda} \tag{20}$$

From Eq. (19) and Eq. (20) we get:

$$\lambda \leq 2.214m$$

Taking the wavelength to be 2.2m, then n/L = 0.9091, giving a frequency of ***60.4Hz*** from Eq. (20).

The shaker must be positioned within the first loop of the standing wave. This implies that it must be within the 1.1m. The span length was then experimentally determined by using the shaker sweep control function to establish a resonance frequency of 60.4Hz at bending amplitude of 0.2mm at the 89mm point from the last point of contact (LCP). The designed test bench is shown in figure 3-9.

During the fatigue testing the temperature was maintained to below 21℃ at all times. The lab is equipped with air conditioners and thermocouples to regulate the temperature to the required value.

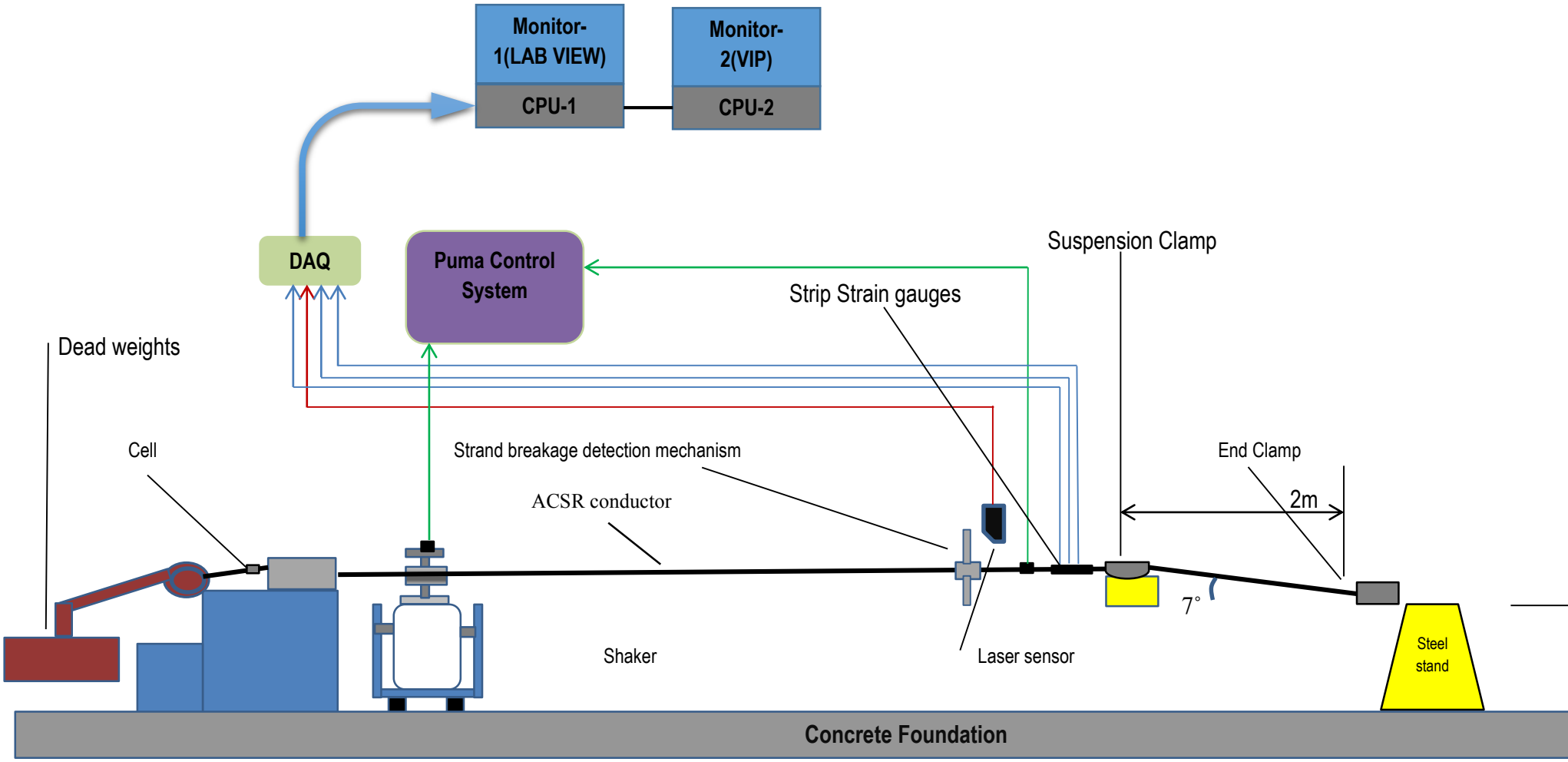


**Figure 3-9: (a) Resonance fatigue testing bench**

**Figure 3-9: (b) Fatigue test set-up at VRTC-UKZN**

### 3.6.1 Conductor Sample preparation

The samples used in this research were supplied by Aberdare to Eskom. Some of the drums were rejected by Eskom due to quality issues and were then forwarded to the Vibration Research and Testing Centre (VRTC) for analysis.

The conductors samples were pulled into the lab from the backyard. End fittings (compression type) were then fitted to the conductors using a crimping machine. The correct dies for the Tern conductor were selected from the crimping chart.

The Tern conductor sample was then strung onto the test bench. The sag angle on the clamp was set to 7° and the tension adjusted to 23.66kN. The bolts on the clamp were tightened to the recommended 40kN-m for the Salvi clamp.

### 3.6.2 Bending amplitude measurement

The bending amplitude is an important parameter in fatigue testing of transmission line conductors. It is a parameter which is commonly used to benchmark the performance of the conductor. In this research, it was required that the bending amplitude be kept with the endurance capability of multilayer ACSR conductors, which is 0.2mm-0.3mm at a point 89mm from the last point of contact between the conductor and the clamp(LCP).

The bending amplitude was measured with a Linear Variable Differential Transformer (LVDT) and confirmed with a Laser sensor. Both sensors give a 0-10V analogue voltage output from the amplifier. The Laser sensor has a built in signal conditioner and requires no extra instrumentation while the LVDT is wired to the National Instruments Data Logger (NI cDAQ) through the P55 amplifier module. Figure 3-10 shows the instrumentation at the suspension clamp.

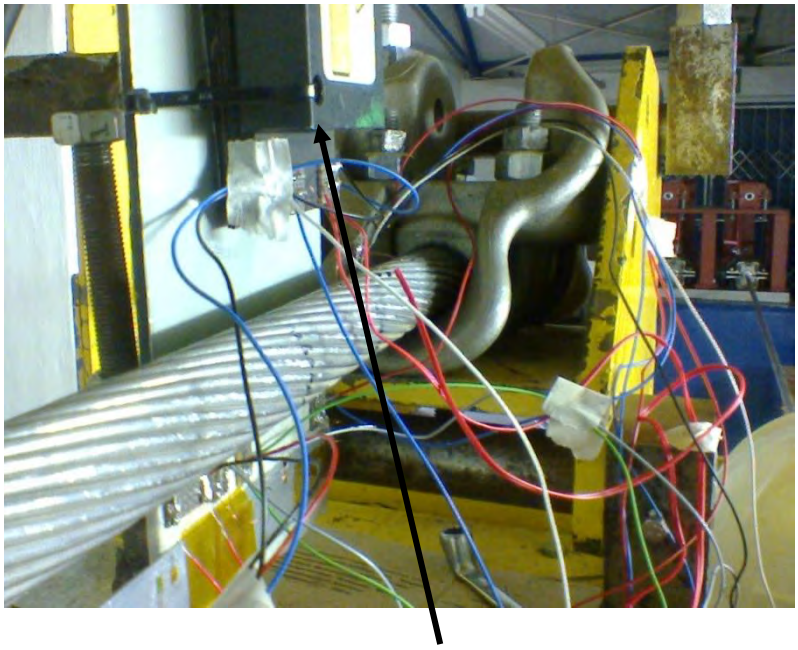


**Figure 3-10: Laser Sensor at the suspension clamp for measuring bending amplitude**

### 3.6.3 Strain measurement

Figure 3-11 below shows the instrumentation at the conductor in the clamp region which was the area of interest in this research. Four strain gauges were mounted on the conductor. The strain gauges were all wired using the Quarter Bridge type II circuit shown in fgure 3-12.

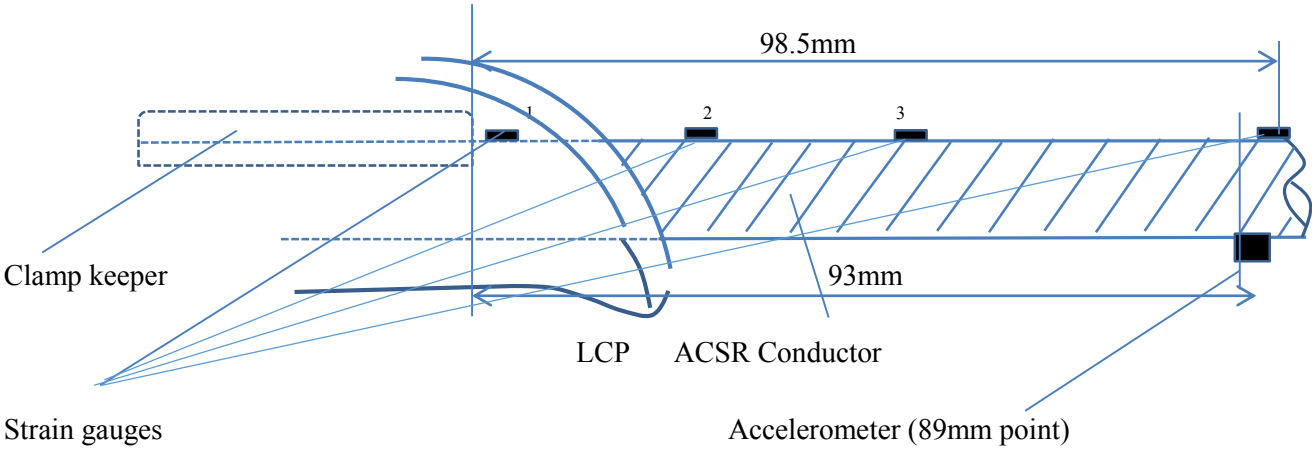


**Figure 3-11: Arrangement of strain gauges at the mouth of the clamp**

The diagram above, the first strain gauge was positioned at 15.2mm from the clamp keeper. The second, third and fourth were positioned at; 32.9mm, 62.1mm and 95.6mm from the first one respectively. On the upper part of the conductor, four gauges were installed. An accelerometer was mounted at 89mm point from the LCP on the bottom side of the conductor. The accelerometer was first mounted on a calibrator and it sensitivity tested in both the upward and downward positions at both 41Hz and 69Hz. The accelerometer did not show any sensitivity change with regards to the mounting directions. The output from the gauges was logged by a data logger and analysed with Microsoft excel and Matlab in graphical form. The results from the strain gauges were used to plot the stress distribution in the clamp region and compare with available theoretical models. Figure 3-12 below show the quarter bridge type II.

The characteristics of the strain gauges used in the analysis are shown in table 3-3.

The quarter bridge type two configuration uses a single active, plus a passive or "dummy" gauge mounted transverse to the active gauge or on another piece of material as the component whose strain is to be measured. The dummy gauge does not measure any strain but is provided for the purposes of temperature compensation only. The applied strain will have very little influence on the dummy gauge as it is mounted perpendicular to the active gauge. Temperature changes will however have the same effect of both the active and dummy strain gauges and will cancel each other out in the balanced Wheatstone bridge. The strain measured by this bridge configuration is given by:

$$\varepsilon = -4V_r * \frac{1 + \frac{R_l}{R_g}}{[GF * (1 + 2V_r)]} \quad (21)$$

Where:

$R_l$ is the Lead wire resistance

$R_g$ is the Nominal strain gauge resistance

GF is the Gauge factor of the strain gauge and is defined as the relationship between the resultant fractional change in gauge resistance to the applied strain (fractional change in length). It is given by the equation below:

$$GF = \frac{\frac{\Delta R}{R}}{\frac{\Delta l}{l}} = \frac{\frac{\Delta R}{R}}{\varepsilon} \quad (22)$$

$\varepsilon$ is the measured strain (in micro-strains)

$V_r$ is given by:

$$V_r = \frac{V_{0\,(strained)} - V_{0(unstrained)}}{V_{ex}} \quad (23)$$

$V_0$ (strained) is the bridge output voltage for a strained component

$V_0$ (Unstrained) is the bridge output voltage for an unstrained component

$V_{ex}$ is the excitation voltage.

The strain measurement with this bridge type is independent of the poison's ratio.

The resistances given in table 3-3 is the series sum of individual resistance of active gauge and the dummy (each gauge has a resistance of 350 Ohms).

In the set-up used in this research, the dummy gauges were mounted separately on an aluminium bar which was then suspended in the vicinity of the suspension clamp.

Before connecting the strain gauges to the system, calibration was carried out. The calibration is aimed at ensuring that the system resistor, $R_1$ and $R_2$ are equal and of the correct value.

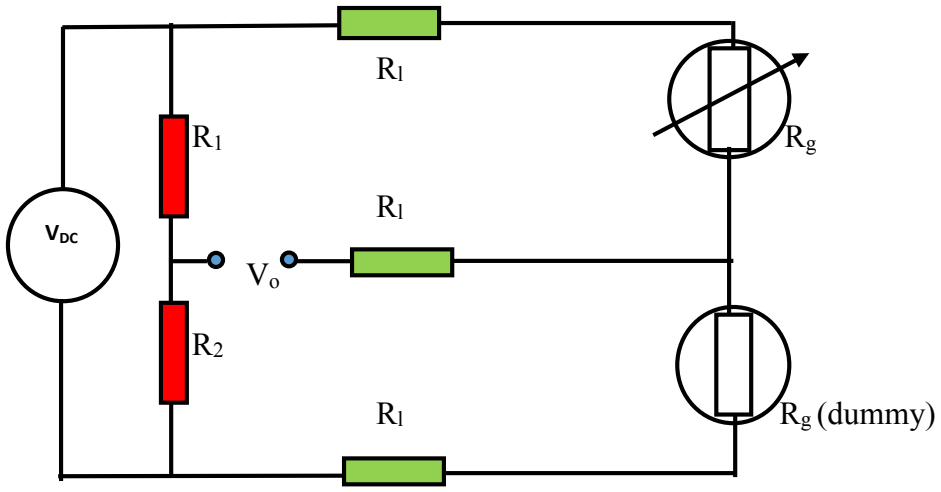


**Figure 3-12: Quarter bridge configuration**

**Table 3-3 Characteristics of the strain gauges**

| Strain Gauge No. | Initial Resistance(Ohms) | K(Sensitivity) |
|---|---|---|
| 1 | **700** | **2.07** |
| 2 | **699** | **2.15** |
| 3 | **699** | **2.15** |
| 4 | **700** | **2.07** |

### 3.6.4 Strand breakage detection mechanism

The strand breakage detection mechanism employed a non-contact displacement detection sensor and National Instruments (cDAQ) data logger. This system basically operates based on the torsional effects of stranded conductors. Depending on the lay direction of the layer in which the broken strand is located, the conductor will rotate through a certain angle due to the redistribution of the tangential component of the conductor tension in the strands. The direction of rotation the conductor of the mechanism also indicates the layer in which the strand has failed (broken). An aluminium blade was attached to the conductor by means of

bolting it to the clamp which was then bolted on the conductor. The laser sensor was used to measure the distance of the aluminium strip from the sensors per cycle and the signal sent to the data logger. The recorded signal was a plot of displacement versus time. If any strand breaks, the conductor will twist through some angle and the aluminium strip will change its position. The laser sensor will pick this abrupt change as a spike and change in average value in the output signal. The data logger used had enough memory to store up to 100 million cycles. The entire assembly was designed in such a way that its weight had minimal effect on the entire conductor-clamp vibrating system.

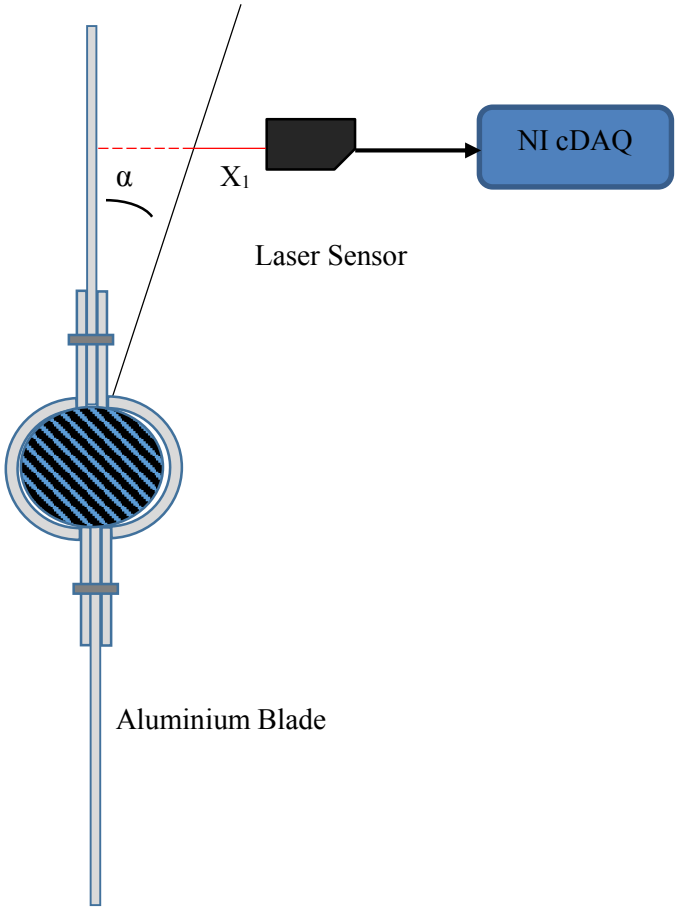


**Figure 3-13: Strand breakage detection mechanism**

When a strand breaks, the entire assembly will rotate about the longitudinal axis of the conductor so that the vertical axis is shifted through some angle α. The non-contact displacement sensor will record a new displacement($x_1$). The mechanism was clamped to the conductor at the node so that it experiences minimal vibration. A laser sensor model LG5B65PU (borrowed from Aberdare) was used for this mechanism.

### 3.6.5 Frequency sweep

To determine the actual resonant frequency, a frequency sweep was done from 0 to 100Hz. Two resonance frequencies were identified, 41 Hz and 69Hz. The 41 Hz frequency corresponded to the frequency calculated from the Eq. (8) with a wind speed of 6m/s as Aeolian vibrations occur for wind speeds between 1-6m/s for single conductors (High Voltage Overhead Power Lines- Theoretical Calculations and Formulae for Conductor Installations, 2009) and was therefore used to test sample number 1, in order to try and simulate the natural conditions. The second sample was tested at 69Hz in order to reduce the testing time. Figure 3-14 shows a sample frequency sweep for conductor sample number 1. The frequency sweep was run using the PUMA control system.

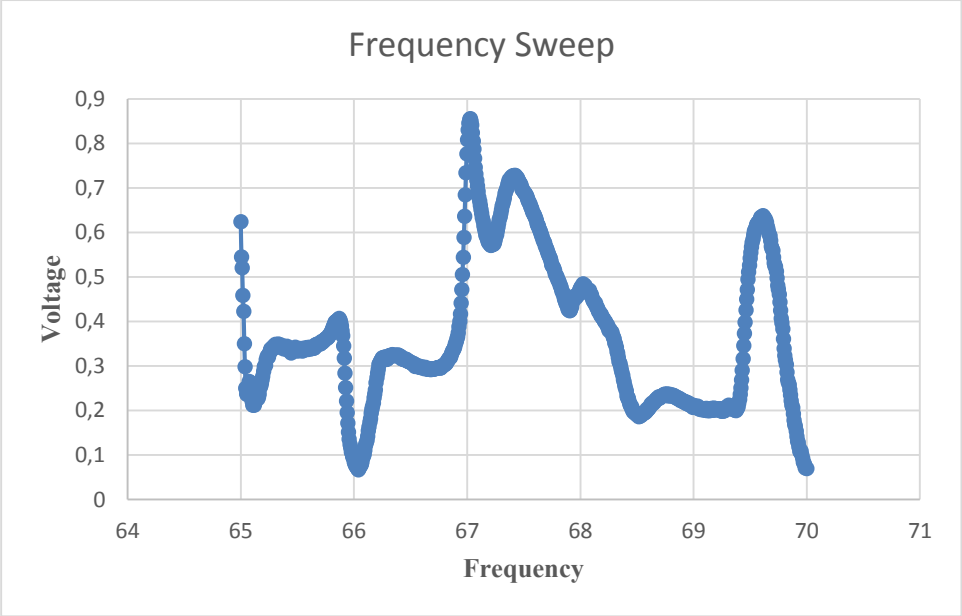


**Figure 3-14: Frequency sweep**

### 3.6.6 Fatigue testing

A LabVIEW program, shown in figure 3-15 below, was used to log all the required data and for monitoring the bending amplitude. The following data was logged:

- The bending amplitude
- Acceleration at the 89mm point
- Strain measurements from all strain gauges
- Displacement from strand breakage mechanism

The Butterworth low pass filters were used to filter the signals and frequency measured using a tone block. The control of the bending amplitude was done manually. An indicator which

showed a green light when the bending amplitude is within the correct value and red when it is out of range was designed into the circuit for easy monitoring of the bending amplitude. The PUMA control system as well as the Vibration interactive program were used to counter check the measurements obtained using LabVIEW.

The temperature in the clamp region was constantly monitored using a FLIR thermos-camera to ensure that it were below 100°C, the temperature at which annealing is expected to occur for aluminium strand.

A screen shot of the data logged is shown in figure 3-16.

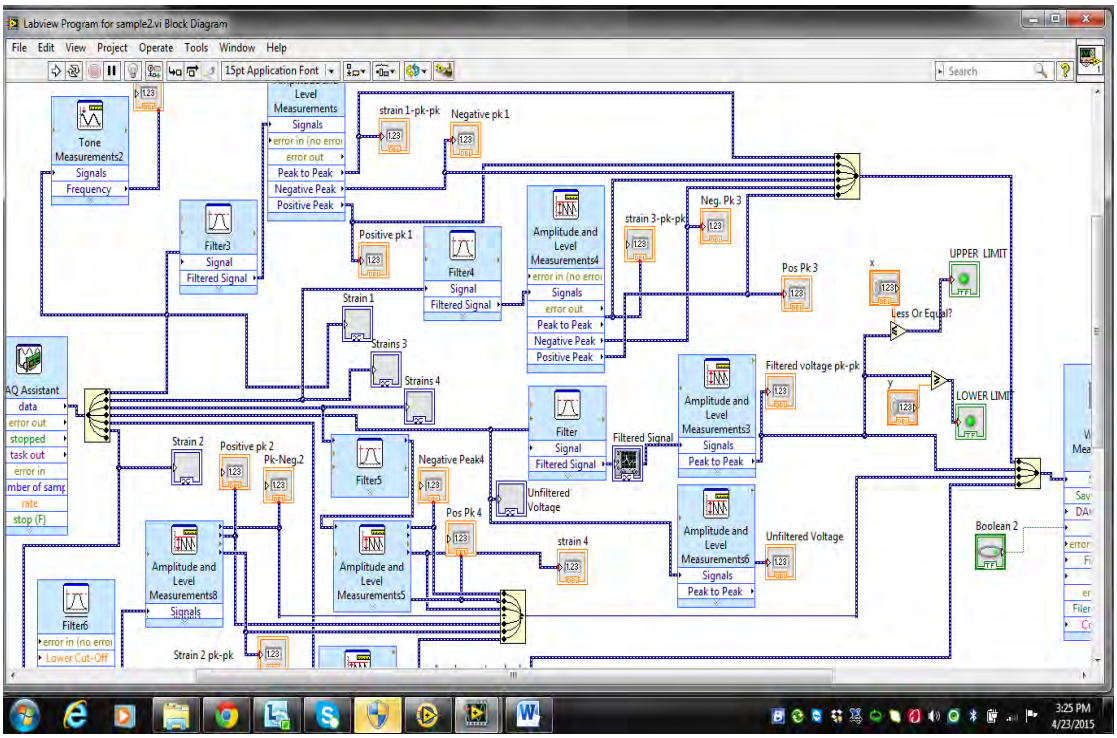


**Figure 3-15: LabVIEW program**

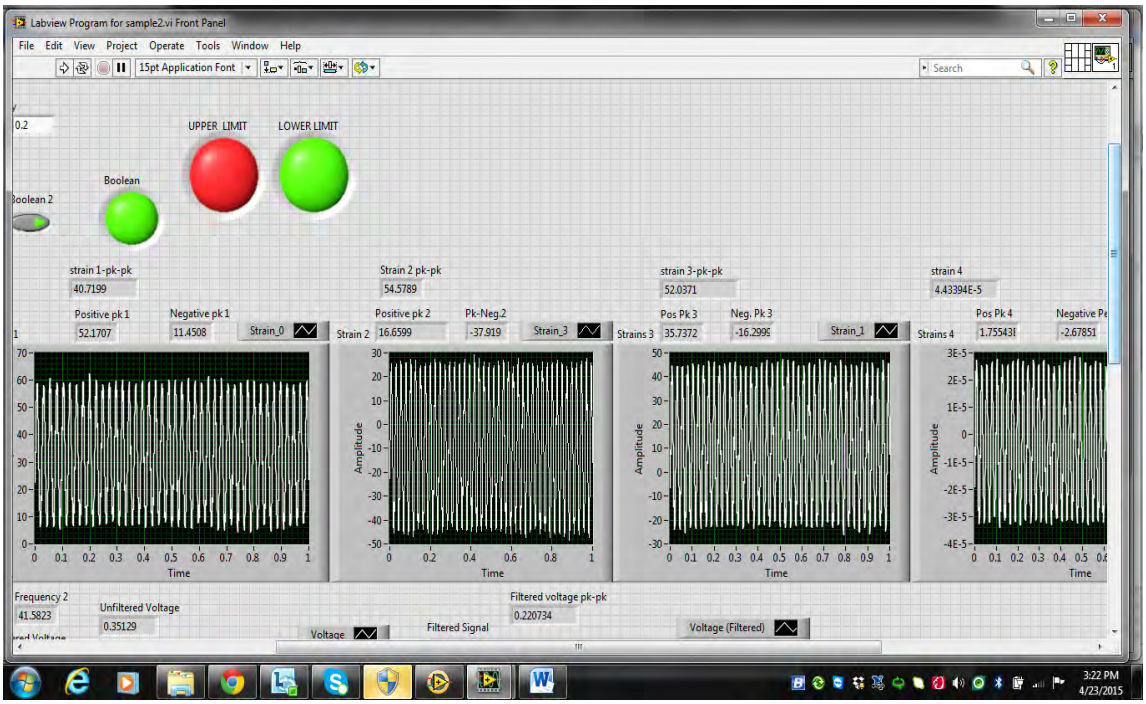


**Figure 3-16: Indicators for Amplitude monitoring**

## 3.7 Fractography

After the fatigue testing of the conductor samples, fractographic analysis was carried out to establish whether the cracks had nucleated and the sites from where they nucleated. During this analysis the stands were not cleaned in order to avoid rubbing off micro-cracks. A conductor sample from the last point of the clamp keeper on the dead end side to the first antinode was cut and subjected to fractographic analysis.

### 3.7.1 Stereomicroscopy

The strands were first checked for any cracks using stereomicroscopy. After identification of fractured surfaces or cracked surfaces, the points of interest were cut into smaller specimens and mounted on the stub for detailed analysis in the SEM. Before being cut into smaller pieces, the distance of the cracks of interest from the front end of the clamp keeper was measured and recorded. The distance measure was the linear distance as the strands were straightened. The actual distance can be calculated by making use of the equation for calculating the length of a helix given as:

$$l = \sqrt{(\pi D)^2 + P^2} \tag{24}$$

This is the length of one turn of a helix. If the measured linear distance for the location of the crack is '$x$', then the actual distance ($x'$) is given by:

$$x' = \frac{x}{l} * P \tag{25}$$

Where:

D is the mean diameter or pitch

P is the lay length

### 3.7.2 Scanning Electron Microscopy

The scanning electron microscope was used to measure the sizes of the cracks which had nucleated and propagated.

### 3.7.3 Energy Dispersive microscopy

The Field Emission Gun Scanning Electron microscope (FEGSEM) was used for determining the elemental composition of the fractured surfaces. The target element was oxygen which would prove the presence of aluminium oxide, which is associated with the fretting fatigue of aluminium conductors.

# 4. Data Collection, Collation and Analysis

### 4.1 Stereomicroscopy and scanning electron microscopy

From the surface characterization carried out using stereomicroscopy and electron microscopy, the dimensions of the fret marks were collected and collated in table 4-1.

In this table, the layer from which the strands were selected is indicated. The strand number and fret mark numbers are also indicated. For the middle and inner layer, the fret mark position is also specified i.e. top or bottom.

The initial depth is the calculated depth, *h* shown in figure 3-5 and is dependent on the width of the fret mark. The length $L_1$ and $L_2$ refer to the measured length in the tilted and un-tilted position of the specimen. The tilt angle is the angle through which the specimen is rotated at constant working distance and magnification for recovery of the third dimension.

As can be seen from the table, some depths appear as negative values. This is because the method used for depth measurement measures the relative depth between two points. Therefore if the reference point is above the point of interest, a positive value results otherwise a negative value will result. All the negative values were converted to a positive value called the mod depth (modulus).

Four points were analyzed per strand and the strands sampled as per SANS 182-2. For strands with fret marks on both the top and bottom sides, this resulted into eight points per strand.

The challenge with using the SEM method for depth measurement was mostly the identification of the same key features in both the normal and the tilted specimen. If the features are slightly missed, the results will be out of range and it depends on the experience and skill of the individual carrying out the experiment to judge whether the result is valid or invalid.

The other challenge with this method is that it is time consuming and would require the equipment dedicated to it. On average, it took about 30 minutes to successfully analyze a single fret mark on the SEM.

The total depth is the overall indentation depth on the strand. The relative depth is a ratio between the total depth and diameter of the strand. The measured conductor parameters are given in the analysis section. Figure 4-1 shows micrographs from the SEM.

## Table 4-1: Results from SEM and stereomicroscopy for sample 1

| | | | | | 3D SEM Stereomicroscopy | | | | | | | |
|---|---|---|---|---|---|---|---|---|---|---|---|---|
| Layer | Strand No. | Mark | Length | Width | L1 | L2 | Tilt Angle | Depth | Mod Depth | Initial Depth | Total Depth | Relative Depth |
| Outer | 1 | 1 | 1449 | 298,3 | 171,9 | 179,2 | 4,7 | 89,017 | 89,017 | 3,297 | **92,314** | 0,027 |
| | | 2 | 706,6 | 266,7 | 125 | 177,1 | 4,7 | 635,310 | 635,310 | 2,635 | **637,946** | 0,189 |
| | | 3 | 2169,3 | 652,08 | 183,4 | 182,9 | 2 | -14,325 | 14,325 | 15,785 | **30,110** | 0,009 |
| | | 4 | 1867 | 460,1 | 380,9 | 387,1 | 2,4 | 148,025 | 148,025 | 7,850 | **155,875** | 0,046 |
| | 2 | 1 | 1226 | 202 | 236,5 | 241,4 | 1,9 | 147,770 | 147,770 | 1,512 | **149,282** | 0,044 |
| | | 2 | 1995 | 395,4 | 289,8 | 296,6 | 1,4 | 278,302 | 278,302 | 5,795 | **284,097** | 0,084 |
| | | 3 | 2290 | 465,4 | 217,7 | 220,6 | 1,7 | 97,744 | 97,744 | 8,032 | **105,775** | 0,031 |
| | | 4 | 2080 | 498,8 | 462,2 | 470,1 | 2 | 226,331 | 226,331 | 9,227 | **235,558** | 0,070 |
| | 3 | 1 | 1953 | 413,8 | 219,6 | 229,2 | 7,6 | 72,427 | 72,427 | 6,348 | **78,775** | 0,023 |
| | | 2 | 2997 | 506,2 | 279,1 | 293,8 | 5 | 168,504 | 168,504 | 9,504 | **178,007** | 0,053 |
| | | 3 | 2227 | 311,4 | 1101 | 1131 | 2,7 | 636,681 | 636,681 | 3,593 | **640,274** | 0,190 |
| | | 4 | 1638 | 355 | 922,3 | 939 | 2,1 | 455,665 | 455,665 | 4,671 | **460,336** | 0,136 |
| | 4 | 1 | 2217 | 505,9 | 390,8 | 393,7 | 2,3 | 72,248 | 72,248 | 9,492 | **81,740** | 0,024 |
| | | 2 | 1554 | 274,2 | 170,5 | 173,3 | 2,9 | 55,326 | 55,326 | 2,786 | **58,112** | 0,017 |
| | | 3 | 2804 | 485 | 490,3 | 477 | 2 | -381,038 | 381,038 | 8,723 | **389,761** | 0,115 |
| | | 4 | 3141 | 487,8 | 175,9 | 170,5 | 2,7 | -114,603 | 114,603 | 8,824 | **123,427** | 0,037 |
| Mid-Layer | 1-Bottom | 1 | 2379 | 499,6 | 1113 | 1098 | 2 | -429,742 | 429,742 | 9,257 | **438,999** | 0,130 |
| | | 2 | 2241 | 418 | 276 | 273,4 | 2,4 | -62,075 | 62,075 | 6,477 | **68,553** | 0,020 |
| | | 3 | 2551 | 391,7 | 1365 | 1352 | 2,1 | -354,709 | 354,709 | 5,687 | **360,397** | 0,107 |
| | | 4 | 1652 | 504,6 | 894,3 | 885,9 | 1,8 | -267,392 | 267,392 | 9,444 | **276,836** | 0,082 |
| | 1-top | 1 | 2117 | 266,1 | 159,8 | 165,8 | 2,6 | 132,233 | 132,233 | 2,624 | **134,856** | 0,040 |
| | | 2 | 2713 | 335,1 | 563 | 553 | 1,4 | -409,267 | 409,267 | 4,162 | **413,429** | 0,122 |
| | | 3 | 2817 | 552,5 | 908,8 | 904,8 | 2,1 | -109,141 | 109,141 | 11,325 | **120,466** | 0,036 |
| | | 4 | 2428 | 446,3 | 1189 | 1208 | 2,4 | 453,626 | 453,626 | 7,385 | **461,012** | 0,136 |
| | 2-Top | 1 | 2068 | 421,9 | 195,3 | 197,9 | 2,6 | 57,301 | 57,301 | 6,599 | **63,900** | 0,019 |
| | | 2 | 2090 | 516,2 | 205,6 | 208,9 | 2,5 | 75,637 | 75,637 | 9,883 | **85,520** | 0,025 |
| | | 3 | 3331 | 649,3 | 369,2 | 394,7 | 2,5 | 584,465 | 584,465 | 15,651 | **600,116** | 0,178 |
| | | 4 | 1759 | 278,9 | 175,2 | 178,6 | 2,2 | 88,554 | 88,554 | 2,882 | **91,436** | 0,027 |
| | 2-Bottom | 1 | 2910 | 518,8 | 328,5 | 332,3 | 2,6 | 83,747 | 83,747 | 9,983 | **93,731** | 0,028 |
| | | 2 | 2122 | 362,5 | 402,8 | 413,2 | 2,2 | 270,870 | 270,870 | 4,870 | **275,741** | 0,082 |
| | | 3 | 2207 | 359,5 | 690,5 | 699,6 | 2,1 | 248,297 | 248,297 | 4,790 | **253,087** | 0,075 |
| | | 4 | 2175 | 268,7 | 151,5 | 158,9 | 2,6 | 163,087 | 163,087 | 2,675 | **165,762** | 0,049 |
| | 3-Top | 1 | 1288 | 300,5 | 254,9 | 263,5 | 2,3 | 214,252 | 214,252 | 3,346 | **217,598** | 0,064 |
| | | 2 | 3155 | 616,1 | 505,2 | 500 | 4,4 | -67,730 | 67,730 | 14,088 | **81,818** | 0,024 |
| | | 3 | 2881 | 556,7 | 368,8 | 365,2 | 3,5 | -58,942 | 58,942 | 11,498 | **70,440** | 0,021 |
| | | 4 | 1263 | 393,8 | 112,4 | 114,6 | 2 | 63,029 | 63,029 | 5,749 | **68,777** | 0,020 |
| | 3-Bottom | 1 | 2433 | 438,6 | 593,1 | 583 | 2,1 | -275,582 | 275,582 | 7,132 | **282,714** | 0,084 |
| | | 2 | 2321 | 355,9 | 303,3 | 313,4 | 2,7 | 214,349 | 214,349 | 4,695 | **219,044** | 0,065 |
| | | 3 | 3439 | 522,3 | 290,7 | 293,4 | 2,3 | 67,265 | 67,265 | 10,119 | **77,384** | 0,023 |
| | | 4 | 3081 | 405,8 | 583 | 589,8 | 2,8 | 139,161 | 139,161 | 6,105 | **145,266** | 0,043 |
| Inner | 1-Top | 1 | 1865 | 438,6 | 1116 | 1102 | 1,9 | -422,200 | 422,200 | 7,132 | **429,333** | 0,127 |
| | | 2 | 2426 | 544,8 | 155 | 148,3 | 2 | -191,951 | 191,951 | 11,011 | **202,962** | 0,060 |
| | | 3 | 2320 | 518,9 | 252,8 | 249,4 | 2,5 | -77,929 | 77,929 | 9,987 | **87,916** | 0,026 |
| | | 4 | 1983 | 480,5 | 322,1 | 315,9 | 2,4 | -148,025 | 148,025 | 8,562 | **156,587** | 0,046 |
| | 1-Bottom | 1 | 2801 | 690,3 | 495 | 490,4 | 4 | -65,904 | 65,904 | 17,695 | **83,599** | 0,025 |
| | | 2 | 1797 | 403,2 | 109,9 | 102,9 | 1,1 | -364,616 | 364,616 | 6,027 | **370,643** | 0,110 |
| | | 3 | 2149 | 341,8 | 506,1 | 503,1 | 3,2 | -53,722 | 53,722 | 4,330 | **58,052** | 0,017 |
| | | 4 | 1827 | 367 | 339,3 | 332,5 | 1,4 | -278,302 | 278,302 | 4,992 | **283,294** | 0,084 |
| | 2-Top | 1 | 1949 | 454,2 | 140 | 143,2 | 2,3 | 79,722 | 79,722 | 7,649 | **87,371** | 0,026 |
| | | 2 | 2838 | 409,6 | 296,6 | 286,5 | 2,2 | -263,057 | 263,057 | 6,220 | **269,276** | 0,080 |
| | | 3 | 1659 | 362,8 | 464,7 | 467,9 | 2,5 | 73,345 | 73,345 | 4,878 | **78,223** | 0,023 |
| | | 4 | 1731 | 334,9 | 782 | 776,3 | 2 | -163,302 | 163,302 | 4,157 | **167,458** | 0,050 |
| | 2-Bottom | 1 | 1726 | 296 | 397,7 | 401 | 1,7 | 111,226 | 111,226 | 3,247 | **114,472** | 0,034 |
| | | 2 | 2371 | 384,2 | 961 | 972,1 | 1,8 | 353,340 | 353,340 | 5,471 | **358,811** | 0,106 |
| | | 3 | 2115 | 727,2 | 169,9 | 173,9 | 1,9 | 120,629 | 120,629 | 19,643 | **140,272** | 0,042 |
| | | 4 | 2416 | 413,1 | 242,6 | 249,4 | 2,5 | 155,857 | 155,857 | 6,326 | **162,184** | 0,048 |

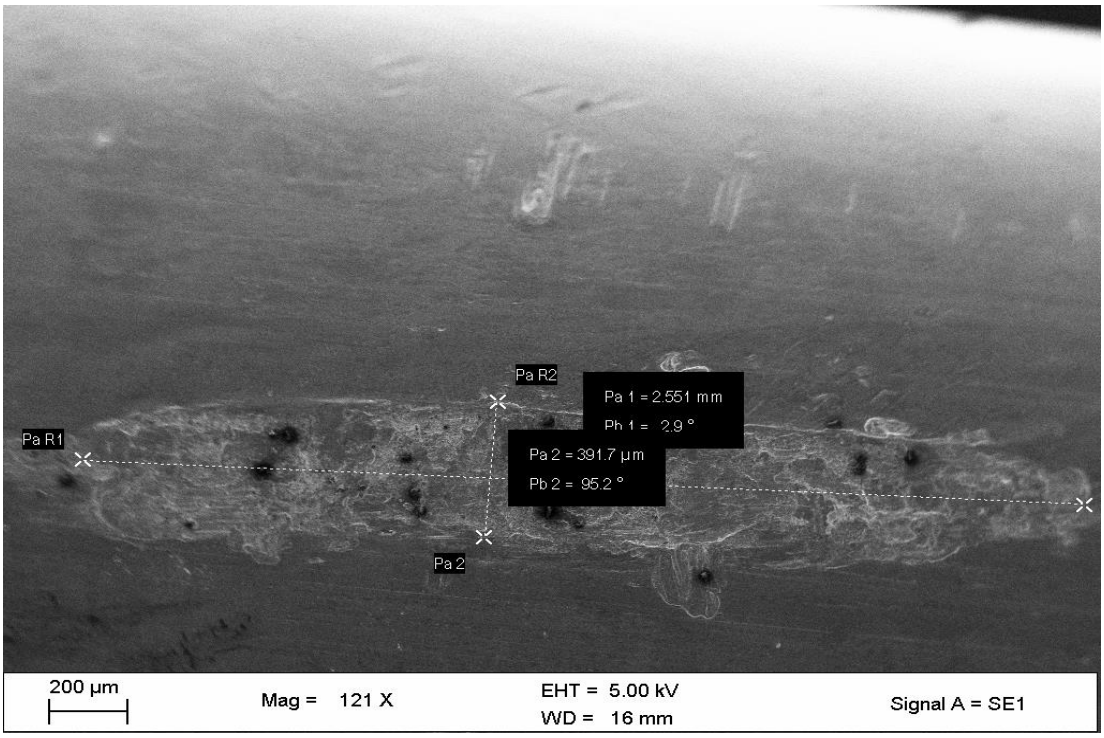


**(a) Strand 1**

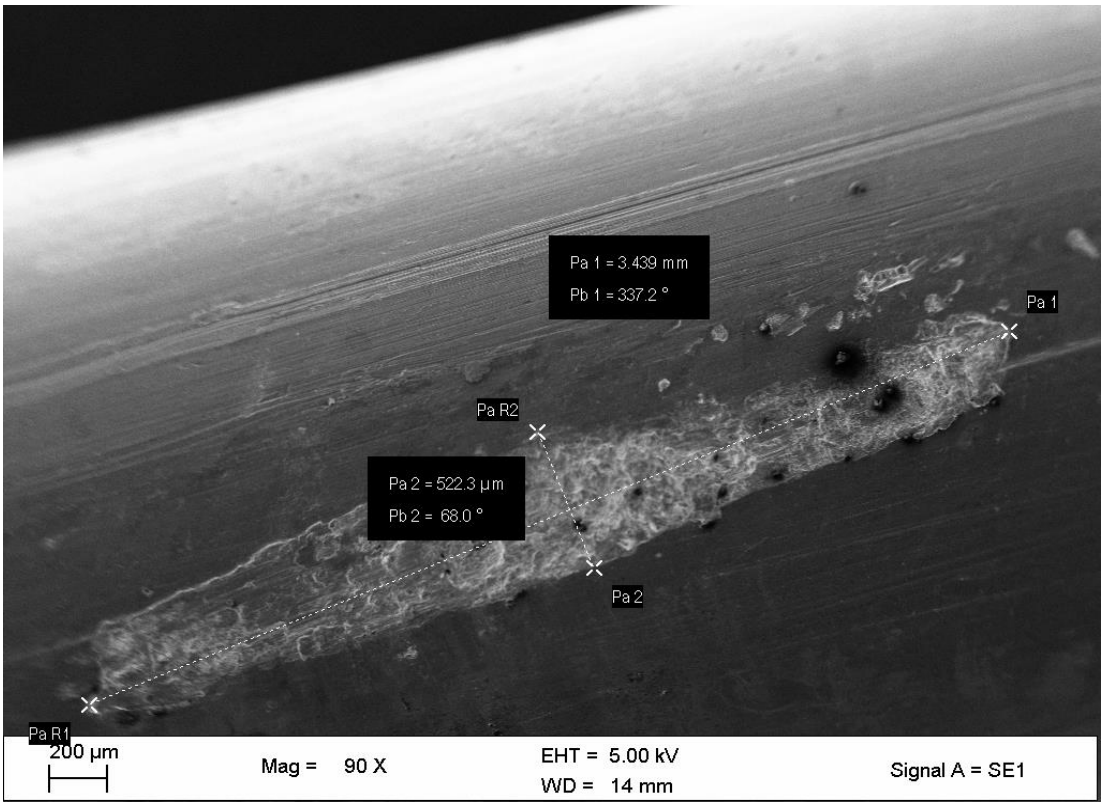


**(b) Strand 2**

**Figure 4-1: Measuring the axes of the fret marks**

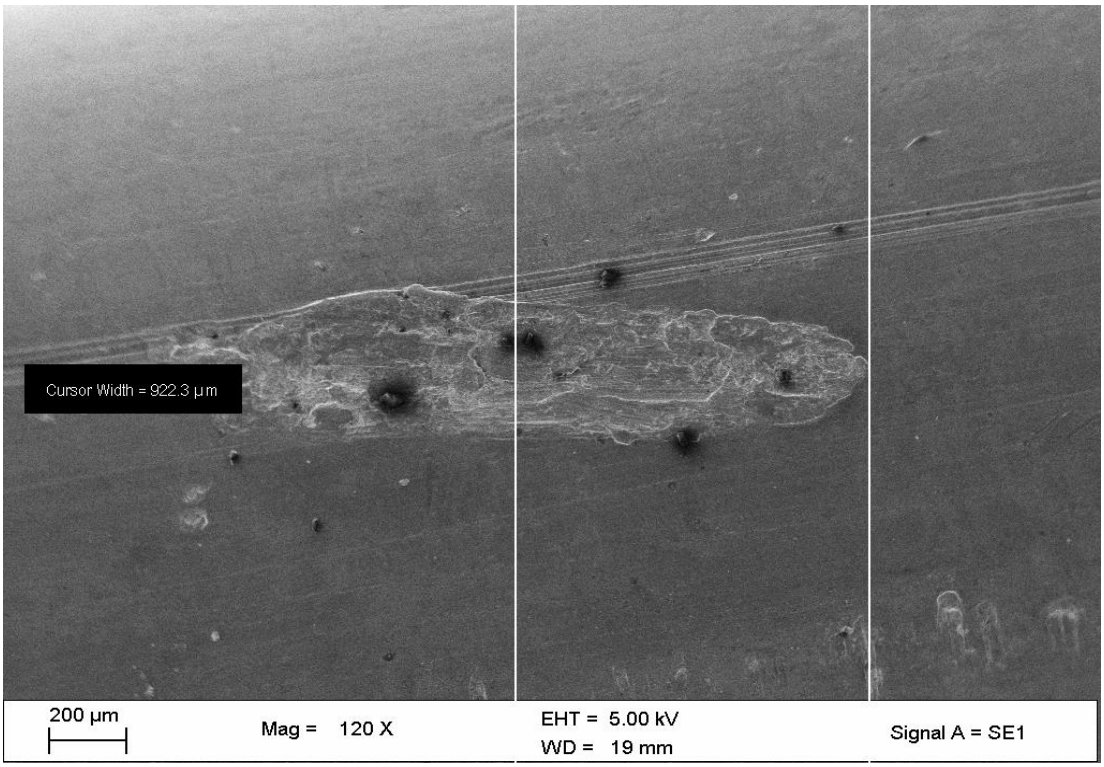


**(a) Untilted Position**

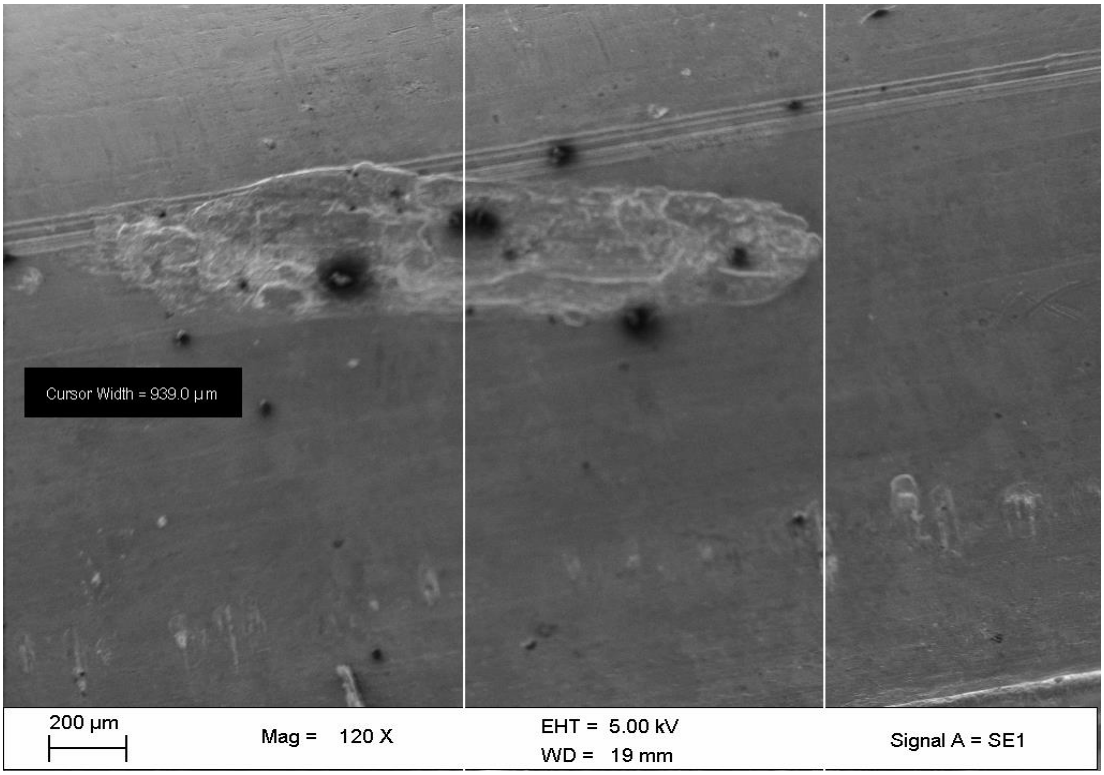


**(b) Tilted Position**

**Figure 4-2: SEM 3D Stereomicroscopy**

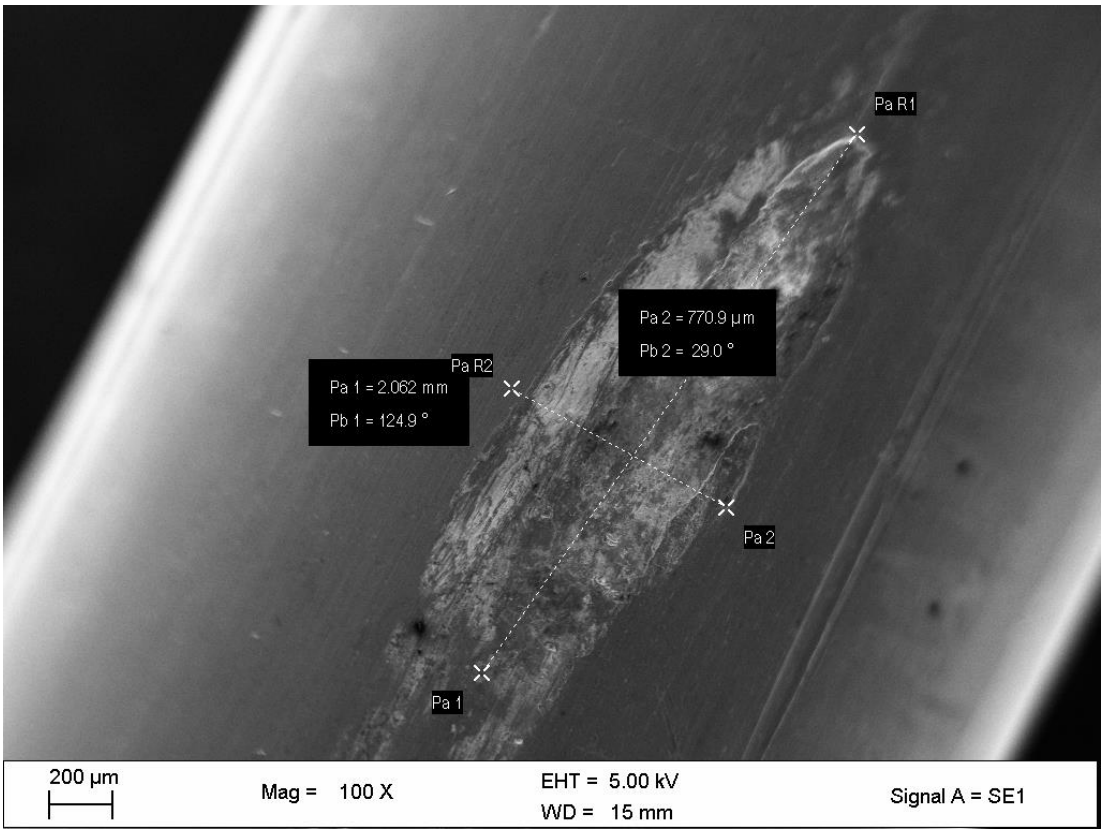


**(a) Fret mark at the core to inner layer contact**

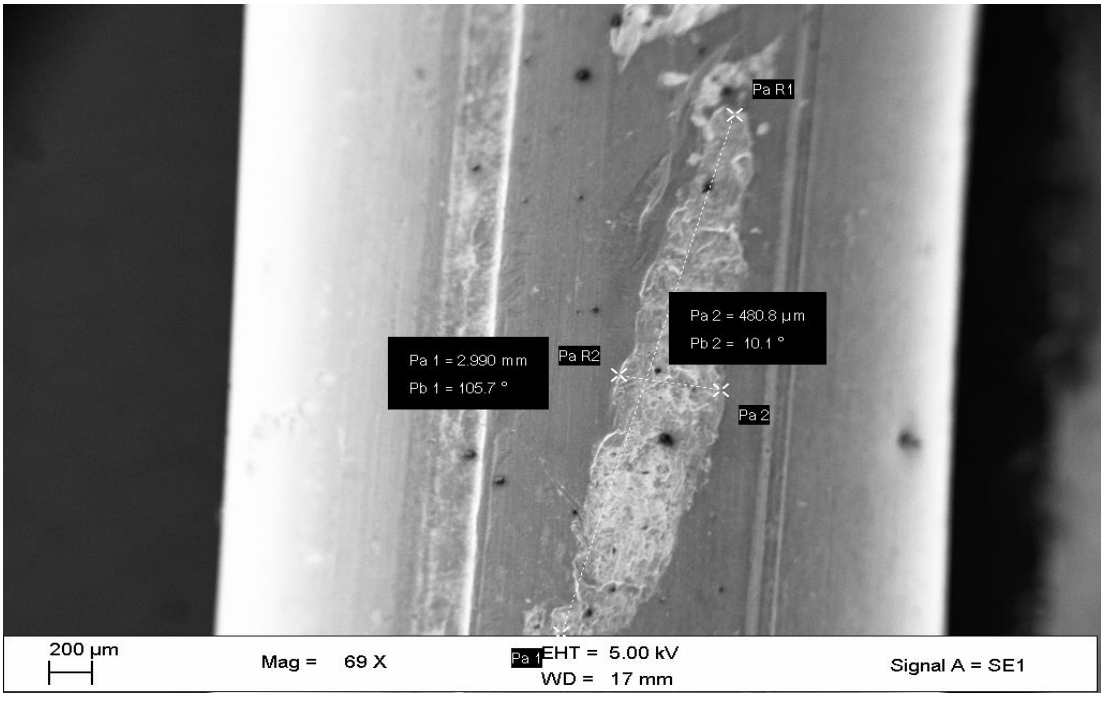


**(b) Fret mark on the outer layer**

**Figure 4-3: Micrographs used for measurements**

Table 4-2 shows a summary of the microscopy results for sample one, bottom of strand fret marks. The fret mark size (area) increases as you move into the inner layers. The marks are largest (in terms of the major and minor axes) in the middle layer bottom side of the strands. The depth is the largest in the outer layer followed by the inner layer and smallest in the middle layer for the analyzed samples. The depth on the other hand reduces progressively from the outer layer to the inner layer. The cable designer must therefore aim at reducing the depth in the outer layer and the surface area in the middle layer.

**Table 4-2 summary of fret mark dimensions for sample 1 bottom side of strands**

| | Sample 1 | | | | |
|---|---|---|---|---|---|
| **Contact pair** | **Length** | **Width** | **Depth** | **Area** | **Eccentricity** |
| **Outer/ Mid-layer** | 2019.62 | 411.13 | 231.34 | 2.61E+06 | 0.979 |
| **Mid/Inner Layer** | 2459.25 | 420.50 | 221.46 | 3.25E+06 | 0.985 |
| **Inner/Core** | 2150.00 | 450.85 | 196.42 | 3.05E+06 | 0.978 |

### 4.2 Fatigue testing results

The samples were subjected to 50 and 40 million fatigue cycles respectively. The first sample was fatigue tested at 41Hz to simulate the natural Aeolian vibration conditions in the South African environmrnent. The second sample was tested at 69 Hz. This was an accelerated fatigue test with all other conditions set as in the testing of sample 01. Annexure D shows a record of the fatigue test for sample 01.

The test took about 3.5 months to achive 50.9 million cycles at 41 Hz reprenting a life of 25 years in service. The biggest challenge was the unavailability of the laboratory after working hours. The test could only be run from 08:00 hours to 16:00 hours. The second conductor sample was exposed to 40 million fatigue cycles.

#### 4.2.1 Bending of the Conductor in the salvi clamp region

The bending strain and hence stress of the conductor in the clamp region was investigated and compared to the available models in the this section. Figure 4-4 shows the strains obtained from the experiments and the ones calculated from the PS equation.

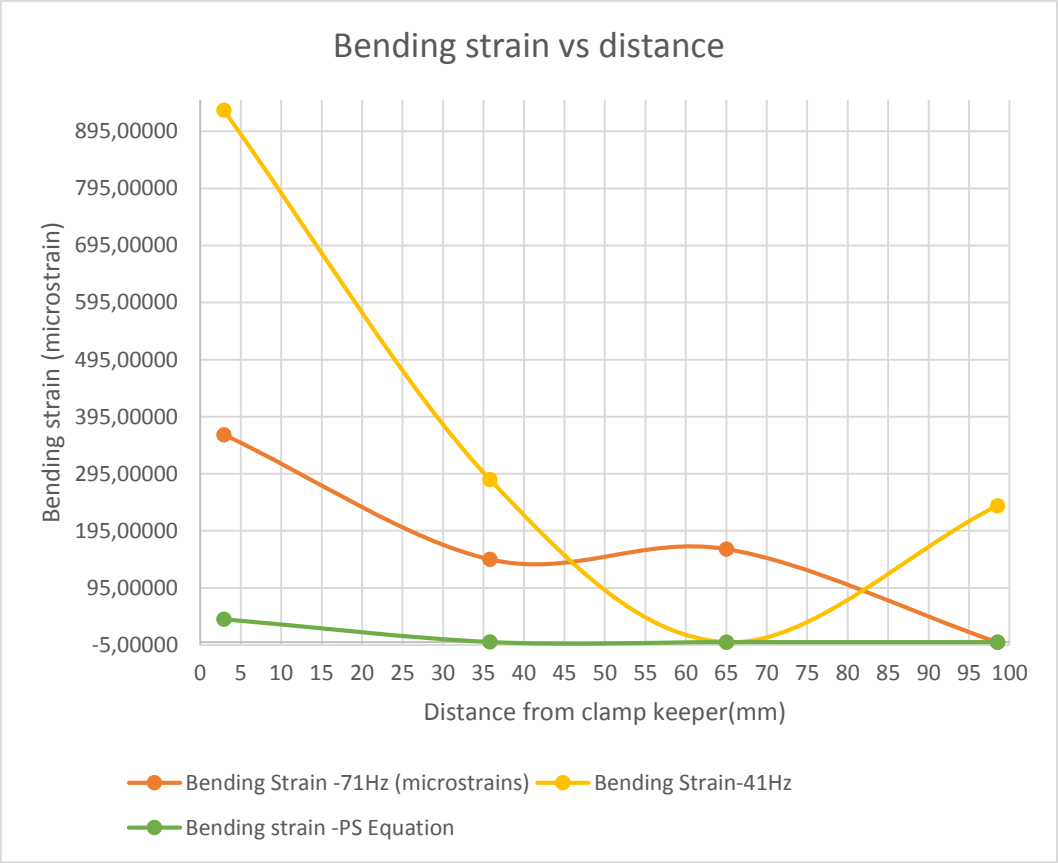


**Figure 4-4: Bending Strains on the upper surface of the conductor**

The bending strain in the clamp region of a square faced clamp is given by the equations below;

$$\sigma_b = KY_b \tag{26}$$

$$\sigma_b = E_a \varepsilon_b \tag{27}$$

The conversion factor K is given by the Poffenberger-Swart (PS) formula and is dependant upon distance from the clamp, the material and design of the conductor.

$$K = \frac{E_a dp^2}{4 * (e^{-p*x} - 1 + p * x)} \tag{28}$$

Therefore the strain is given by:

$$\varepsilon_b = \frac{d.p^2}{4 * (e^{-p*x} - 1 + p * x)} Y_b \tag{29}$$

$Y_b$ is the bending amplitude peak to peak in mm

$E_a$ is the modulus of Elastic of an outer strand wire

$\sigma_b$ is the bending stress ( 0 to peak)

$\varepsilon_b$ is the corresponding bending strain

*d* is the diameter of the outer strand

*T* is the conductor tension

*E*I* is the sum of the flexural rigidity of the individual conductor strands

$$p^2 = \frac{T}{E * I}$$

*x* is the distance of measurement from the last point of contact (LCP)

The PS equation gives strains which are lower than the measured valued for this set-up. The peak stress was however closer to that measured at 71Hz as the PS equation value has to be doubled( the PS equation calculates the peak strain while the measured strain is the peak to peak).

The bending strain at 41Hz can be approximated by a quadratic equation below with a regression constant of 0.9977:

$$\varepsilon = 0.2152x^2 - 29.266x + 1025 \quad (30)$$

The strains measured at 71Hz can be modelled by the following equation;

$$\varepsilon = 0.0021x^3 + 0.3387x^2 - 16.773x + 409.62 \quad (31)$$

**4.3 Energy dispersive spectroscopy**

The results from the Energy dispersive spectroscopy (EDS) are shown in the reports in annexure B. Each report contains a table showing the percentage weight of elements on the surafces of the fret marks, the image and the spectrum. These reports were generated on the FEGSEM.

The results from all the reports are summarized in the table 4-3. It is worth noting that there is a high Zinc content on the surfaces of the fret marks in the inner most layer. There is transfer of Zinc from the galvanized steel wires in the core to the inner layer aluminum wires.

**Table 4-3: Summary of EDS results**

| Layer | Position | Al | O | C | Si | K | Ca | Zn | Fe | Total | Trace |
|---|---|---|---|---|---|---|---|---|---|---|---|
| Inner Layer | Top | 82,8 | 15,93 | 0 | 0,55 | 0,06 | 0,07 | 0 | 0,24 | | |
| | | 28,9 | 19,04 | 7,93 | 0,08 | 0,01 | 0,01 | 44,04 | 0 | | |
| | | **55,85** | **17,485** | **3,965** | **0,315** | **0,035** | **0,04** | **22,02** | **0,12** | **99,83** | **0,17** |
| | Bottom | 64,48 | 23,36 | 0 | 0,01 | 0,03 | 0 | 11,7 | 0 | | |
| | | 34,15 | 17,04 | 0 | 0,11 | 0,01 | 0 | 48,55 | 0 | | |
| | | **49,315** | **20,2** | **0** | **0,06** | **0,02** | **0** | **30,125** | **0** | **99,72** | **0,28** |
| Mid-Layer | Top | 65,76 | 7,745 | 25,11 | 0,67 | 0,2 | 0,6 | 0 | 0,245 | | |
| | | 61,19 | 8,32 | 28,24 | 0,97 | 0,2 | 0,2 | 0 | 0,41 | | |
| | | **63,475** | **8,0325** | **26,675** | **0,82** | **0,2** | **0,4** | **0** | **0,3275** | **99,93** | **0,07** |
| | Bottom | 89,85 | 8,33 | 0 | 0,66 | 0 | 0,17 | 0 | 0,4 | | |
| | | 91,68 | 7,52 | 0 | 0,19 | 0,04 | 0 | 0 | 0,2 | | |
| | | **90,765** | **7,925** | **0** | **0,425** | **0,02** | **0,085** | **0** | **0,3** | **99,52** | **0,48** |
| Outer Layer | Bottom | 67,31 | 19,35 | 11,32 | 0,13 | 0 | 0 | 0 | 0,17 | | |
| | | 78,92 | 11,67 | 3,46 | 3,98 | 0,22 | 0,15 | 0 | 0,87 | | |
| | | **73,115** | **15,51** | **7,39** | **2,055** | **0,11** | **0,075** | **0** | **0,52** | **98,775** | **1,225** |

## 4.4 Fractography

### 4.4.1 Nucleation and propagation of cracks

The strand surfaces were examined as explained in the methodology section of this thesis. Micro cracks were observed to have nucleated but in most cases not a critical length or depth. Most of the cracks are observed to be transverse to the major axis of the fret marks. Figure 4-3 shows some of the examined surfaces after the fatigue testing. In most cases the cracks had nucleated from the fret marks. In very rare cases were the cracks observed to have nucleated from other defects such as scratches. The longest observed crack was about 14.3% of the diameter of the aluminum strand.

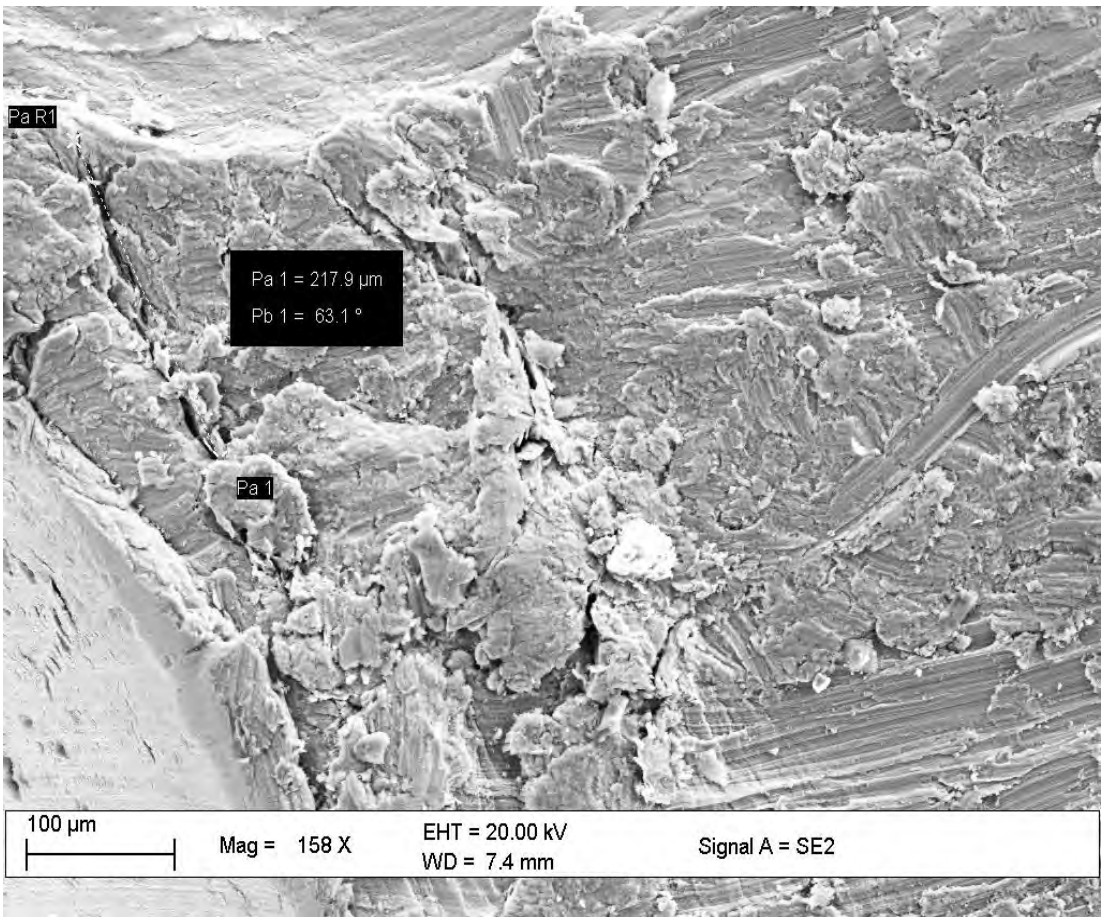


**(a) 217.9micron crack on surface**

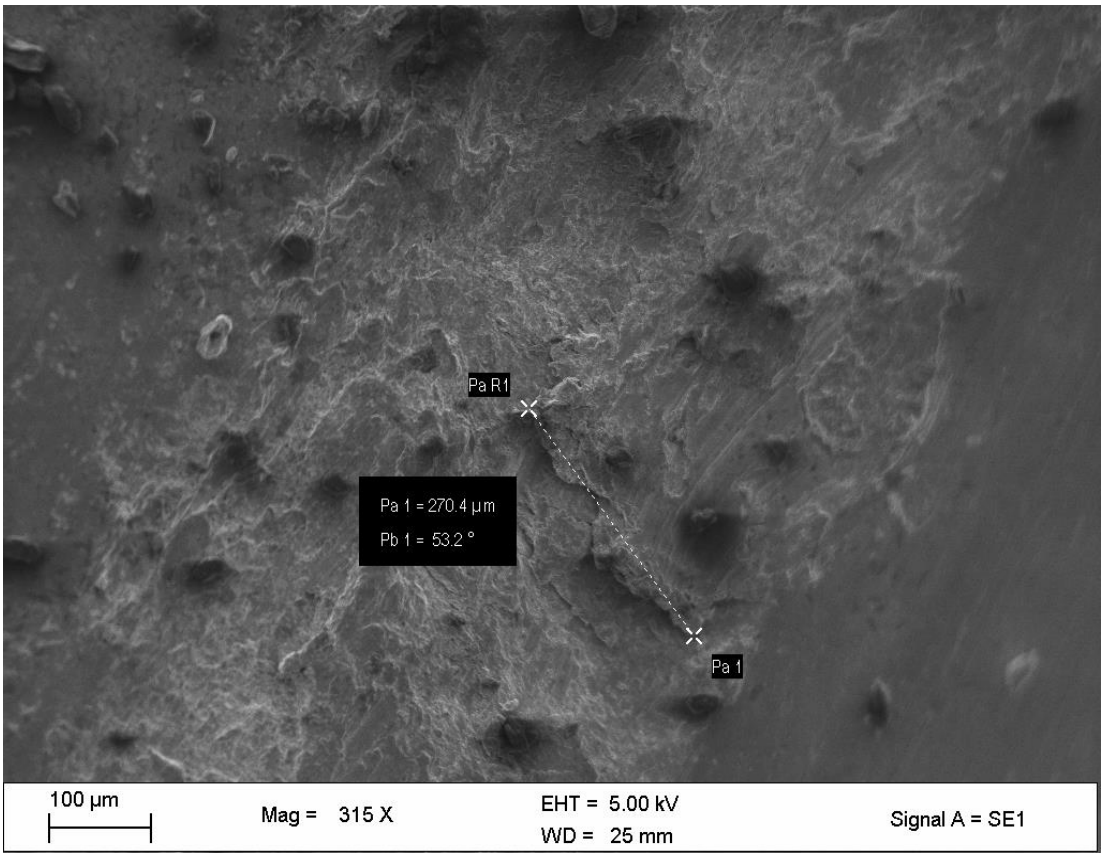


**(b) 270.4 microns crack**

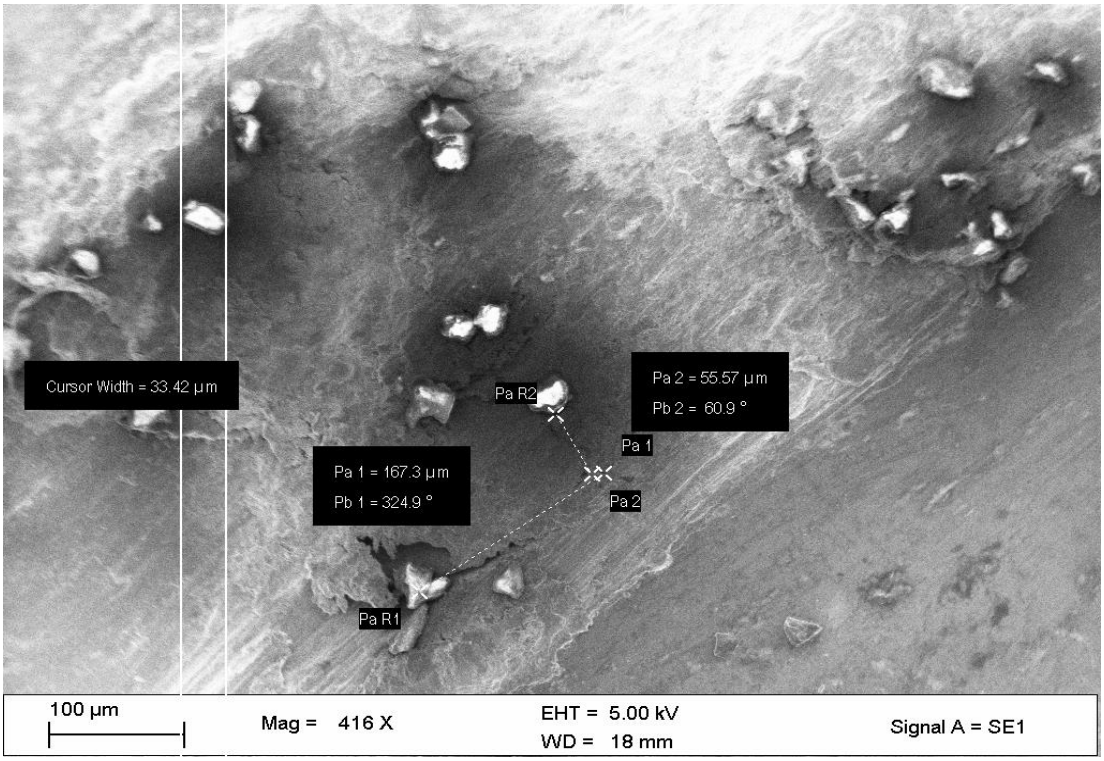


**(c ) Multiple cracks on surface of fret mark**

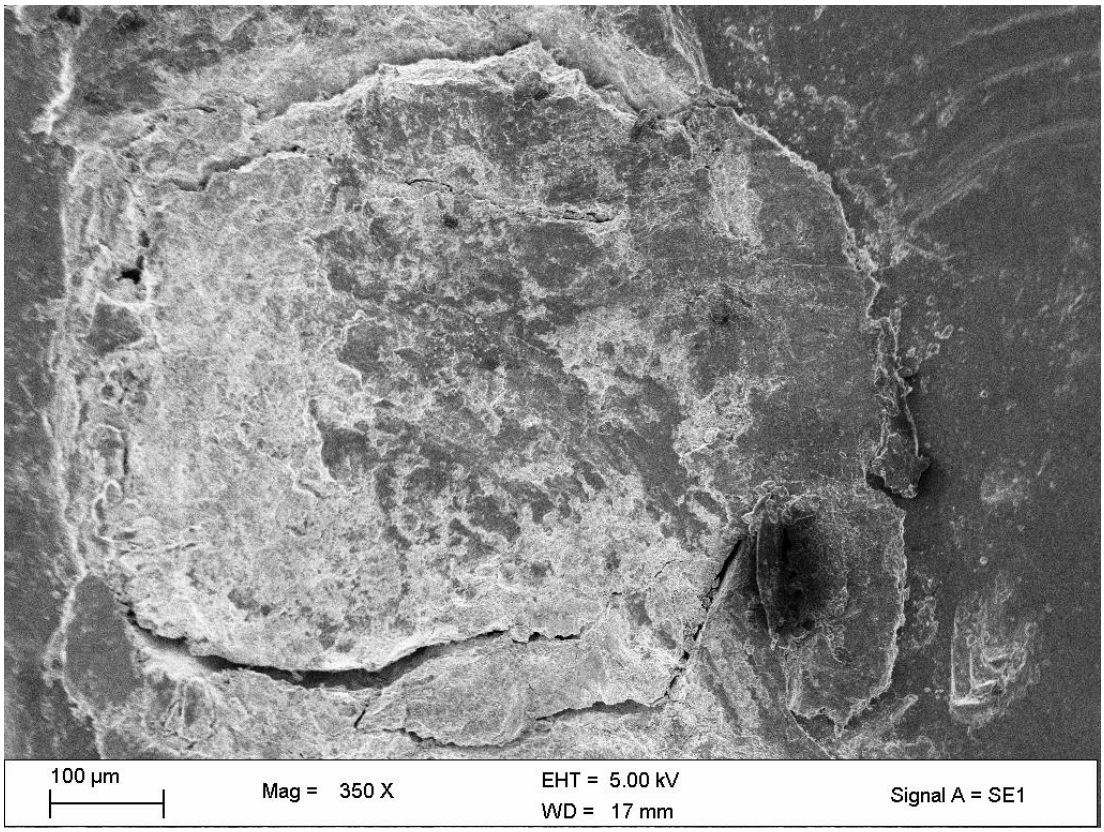


**(d) Fractured surface of the outer layer of sample 1**

**Figure 4-5 (a-d): Micrographs for fatigue tested samples**

The results of the SEM examination for sample 1 is given in table 4-4. The stresses given in the last column are based on a modulus of elastcity of 69GPa for an outer aluminium strand. The strains were extracted from figure 4-2 for sample 1 vibrating at 41Hz. Table 4-5 shows the results obtained for sample 2.

**Table 4-4: Fractographic analysis for sample 1**

| Location (Linear distance)-mm | Layer | Crack length-microns | Strain-microstrains | Stress-MPa |
|---|---|---|---|---|
| **15** | Outer Layer | 485.3 | 680 | 47.6 |
| **90** | Midlayer | 167.3 | 158 | 10.9 |
| **5** | Mid-layer | 84.33 | 895 | 61.755 |
| **45** | Mid-layer | 173.6 | 150 | 10.35 |
| **60** | Mid-layer | 222.5 | 10 | 0.69 |

| Location (Linear distance)-mm | Layer | Crack length-microns | Strain-microstrains | Stress-MPa |
|---|---|---|---|---|
| **60** | Mid-layer | 102.9 | 10 | 0.69 |
| **85** | Mid-layer | 176.8 | 115 | 7.935 |
| **80** | Mid-layer | 115.1 | 75 | 5.175 |
| **90** | Mid-layer | 81.19 | 165 | 11.385 |
| **25** | Inner Layer | 61.59 | 475 | 32.775 |
| **34** | Inner Layer | 44.87 | 315 | 21.735 |
| **60** | Inner Layer | 266.9 | 10 | 0.69 |

**Table 4-5: Fractographic analysis for sample 2**

| Location (Linear distance)-mm | Layer | Crack length-microns | Strain-microstrains | Stress-MPa |
|---|---|---|---|---|
| **5** | Outer Layer | 170.9 | 350 | 24.15 |
| **24** | Outer Layer | 97.5 | 208 | 14.352 |
| **50** | Outer Layer | 270.4 | 150 | 10.35 |
| **20** | Outer Layer | 111.0 | 238 | 16.42 |
| **47** | Outer Layer | 53.71 | 142 | 9.80 |
| **10** | Outer Layer | 60 | 310 | 21.39 |
| **37** | Outer Layer | 118.1 | 142 | 9.80 |
| **55** | Outer Layer | 147.6 | 160 | 11.04 |
| **25** | Mid-layer | 43.96 | 206 | 14.21 |
| **93(89mmpoint)** | Mid-layer | 219.1 | 30 | 2.07 |
| **7** | Mid-layer | 99.06 | 335 | 23.12 |
| **30** | Mid-layer | 105.6 | 170 | 11.73 |
| **45** | Inner Layer | 104.4 | 140 | 9.66 |
| **20** | Inner Layer | 138.0 | 238 | 16.42 |

| Location (Linear distance)-mm | Layer | Crack length-microns | Strain-microstrains | Stress-MPa |
|---|---|---|---|---|
| **21** | Inner Layer | 130.0 | 230 | 15.87 |
| **59** | Inner Layer | 44.86 | 168 | 11.59 |
| **44** | Inner Layer | 61.00 | 140 | 9.66 |
| **35** | Inner Layer | 88.74 | 142 | 9.80 |

The stress calculated in most cases is higher than the Electrical Power Research Institute (EPRI) quoted endurance capability for a multilayer conductor of 8.5N/mm$^2$. Meaning that theoretcially the conductor can not endure 500 million cycles. The bending strain measured at the 89mm point in the test carried out at 41Hz was 200 microstrains which corresponds to the IEEE recommended enduarance capability for multilayer conductors. Note that the position of gauges in the table were measured relative to the clamp keep and not the LCP. Therefore, the 89mm point is actually at 93mm from the clamp keeper. Fig. 4-2 was used for extracting the strain values.

### 4.5 EDS on fatigue tested samples

The results of the EDS on fatigue tested samples on the fret marks are presented below. Sample reports per layer are given for illustration purposes only. The results from all the reports are collated in table 4-6 below.

**Table 4-6: EDS on fatigue tested samples**

| Layer | Position | Al | O | C | Si | K | Ca | Zn | Fe | Total | Trace |
|---|---|---|---|---|---|---|---|---|---|---|---|
| Inner Layer | Top | **94,91** | **4,83** | **0** | **0,26** | **0** | **0** | **0** | **0** | **100** | **0** |
| | Bottom | 71,7 | 15,48 | 9,56 | 2,76 | 0,11 | 0 | 0 | 0,4 | | |
| | | 88,69 | 10,48 | 0 | 0,3 | 0,11 | 0 | 0 | 0,21 | | |
| | | **80,195** | **12,98** | **4,78** | **1,53** | **0,11** | **0** | **0** | **0,305** | **99,9** | **0,1** |
| Mid-Layer | Top | **76,14** | **17,37** | **0** | **5,72** | **0,15** | **0** | **0** | **0,5** | **99,88** | **0,12** |
| | Bottom | 77,51 | 7,93 | 10,15 | 0.31 | 0 | 0 | 0 | 0,2 | | |
| | | 64,86 | 11,2 | 13,88 | 0,07 | 0 | 0 | 13,45 | 0 | | |
| | | **71,185** | **9,565** | **12,015** | **0,035** | **0** | **0** | **6,725** | **0,1** | **99,625** | **0,375** |
| Outer Layer | Bottom | 74,07 | 7,65 | 17,69 | 0,23 | 0 | 0 | 0 | 0,26 | | |
| | | 90,74 | 6,92 | 0 | 1,87 | 0 | 0,02 | 0 | 0,45 | | |
| | | **82,405** | **7,285** | **8,845** | **1,05** | **0** | **0,01** | **0** | **0,355** | **99,95** | **0,05** |

The results from the EDS analysis can be summarised in the histogram below. The analysis is carried out per layer to show the elemental changes per layer. Figure 4-4 (a) to (d)

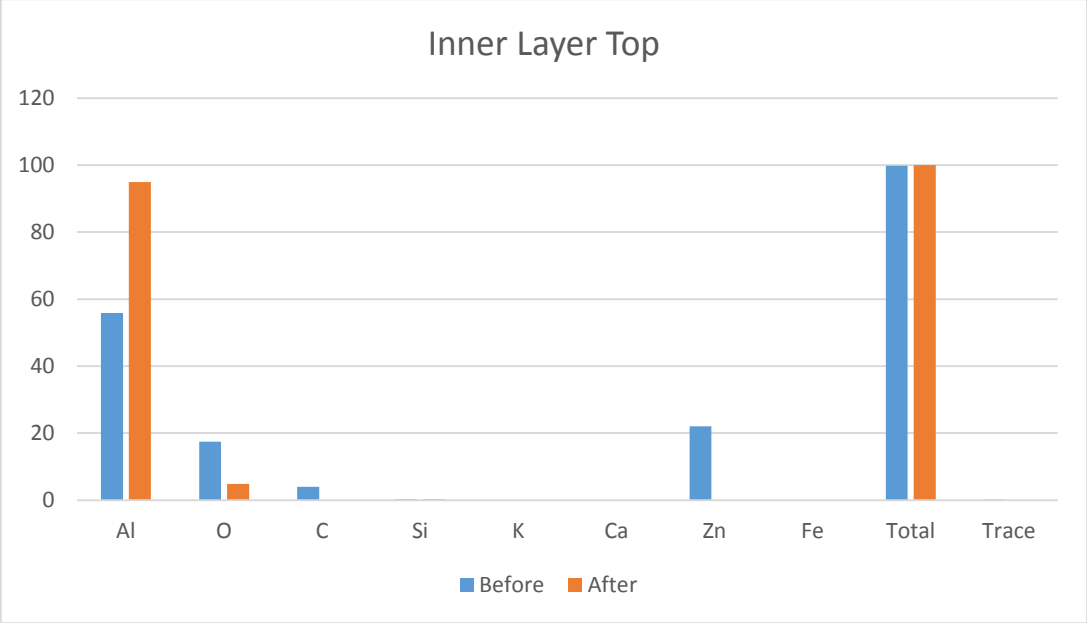


**(a) Inner Layer top fret marks**

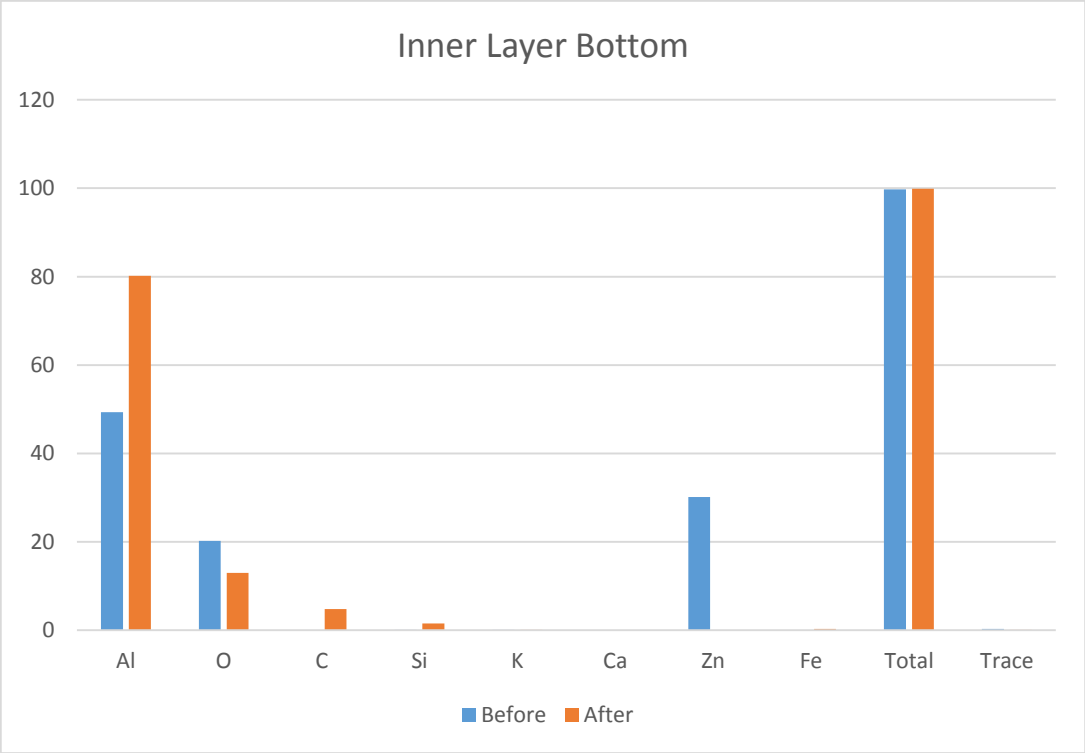


**(b) Inner Layer Bottom fret marks**

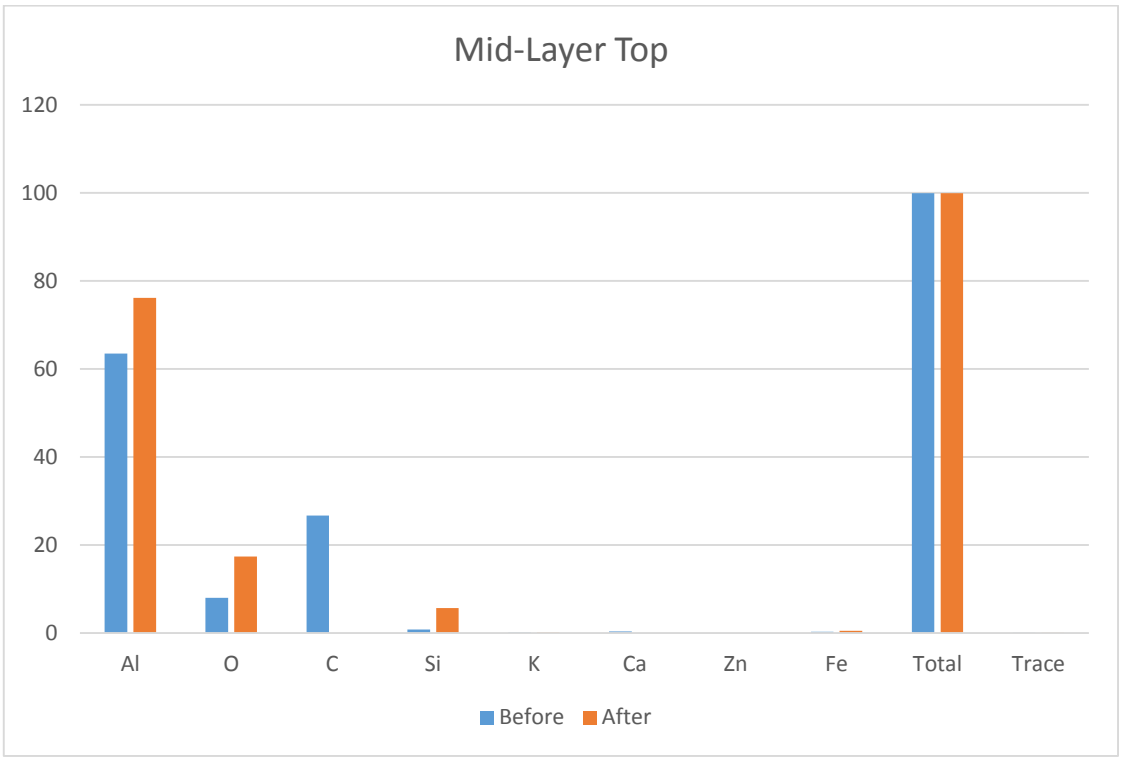


**(c) Middle layer top fret marks**

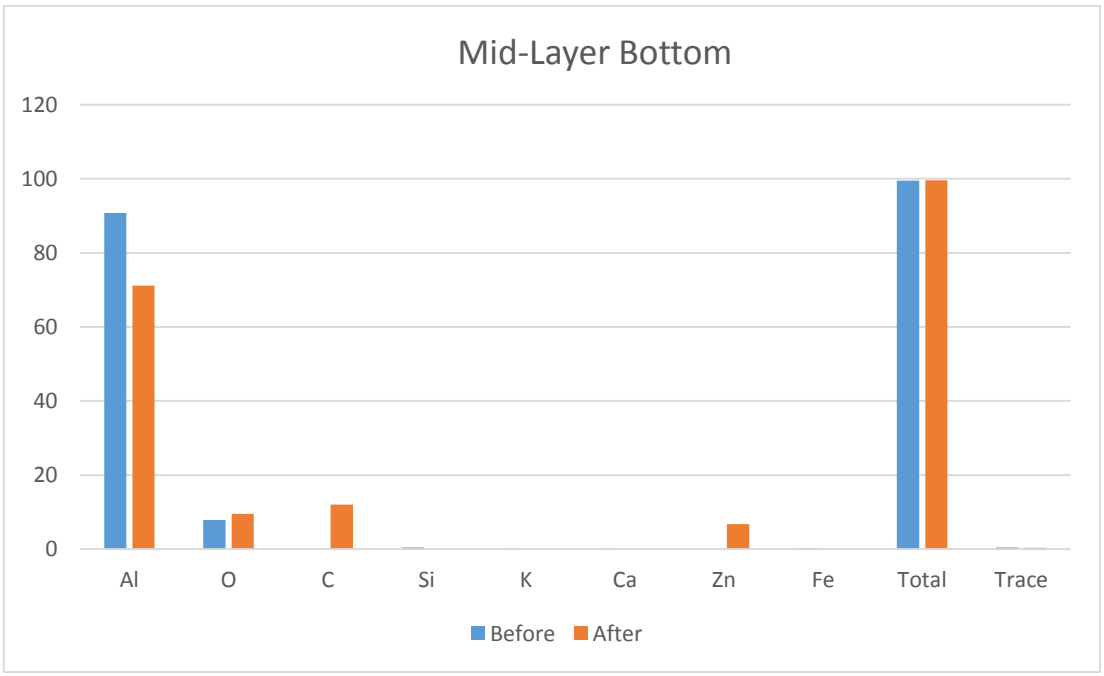


**(d) Mid-Layer Bottom fret marks**

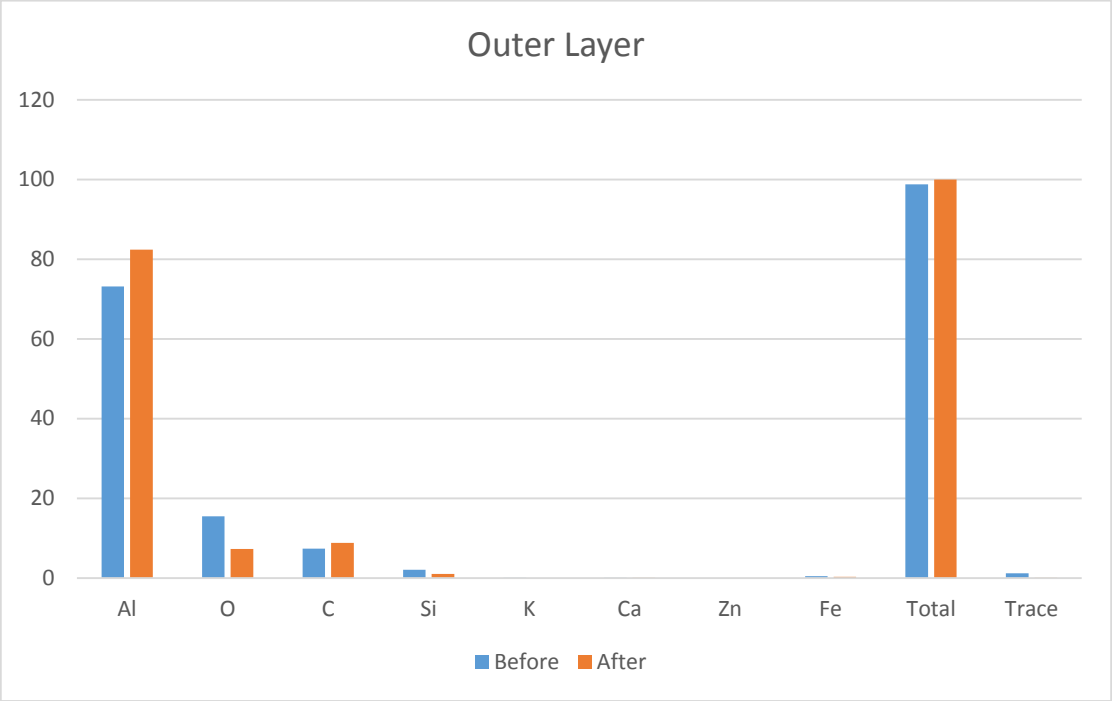


**(e) Outer Layer**

**Figure 4-6: Histograms for EDS analysis of results**

From the histograms, it can be seen that the percentage of aluminium increases after 50 million cycles of fatigue testing. This is because, before the tests, the surface of the fret mark is covered with aluminium oxide associated with fretting fatigue and after the testing, this layer is scrapped off the surface leaving mostly aluminium on the surface.

In all cases oxygen is present on the examined surfaces indicating the presence of aluminium oxide and hence the occurrence of fretting fatigue. In most instances the percentage of oxygen was seen to have increased indicating that fretting fatigue was progressively occurring as this increase corresponds to an increase in surface area which will be exposed and hence oxidised.

Another element worth noting in the analysis is Zinc. The steel wires of the core are galvanized in zinc. It is not surprising to see Zinc present on the surface of the aluminium strands in the inner layer as they are in contact with the steel wires. Attention is however paid to situations where there is Zinc present in the second layer after fatigue testing as it indicates that the steel wires are losing the galvanization. The indication of loss of galvanization at 50 million cycles means that the galvanization might not stand 100 million of fatigue cycles and hence core lubrication (case 1) presented in section 1.2.3 can be recommended for most of the conductor application. The loss of galvanization was also evidenced by the shiny spots on the contact points on the steel wires after the fatigue tests.

# 5. Contact Mechanics

The mathematical theory for the general three-dimensional contact problems was first given by Hertz (1881). There is an extensive Hertzian theory which includes both stress and strain and strain analysis together with a comprehensive bibliography has been published by Lubkin (1962).

## 5.1 General Theory

The assumption is made that the surfaces in contact are perfectly smooth, that the bodies are isotropic and linearly elastic, that the elastic limit of the materials is not exceeded and that frictional forces are absent. The finite force keeping them together will then be distributed over the common area of contact. The surfaces of the bodies will be assumed to be of second degree, implying that all the terms higher than two in the surface equations will be neglected.

If two bodies are in mathematical contact (touching but unstressed and not deformed) so that the common normal is parallel to the applied load, the common tangent plane is the plane *xy* and the common normal is the *z* as shown in figure 5-1 below.

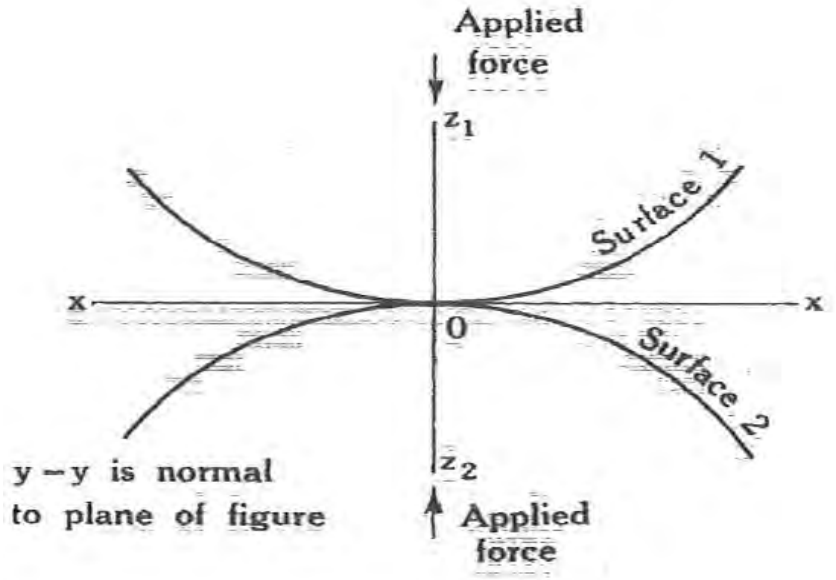


**Figure 5-1: Two dimensional bodies in mathematical contact**
**(Source: Johnson, K. L., 1985)**

The general equation of a surface of second degree is given by:

$$Ax^2 + By^2 + cz^2 + 2fyz + 2gzx + 2hxy + 2ux + 2vy + 2wz + d = 0 \quad (32)$$

At the origin,$x = y = z = 0$. Therefore, *d* = 0. Differentiating equation (32) with respect to *x:*

$$2Ax + 2cz\frac{\partial z}{\partial x} + 2fy\frac{\partial z}{\partial x} + 2gz + 2gx\frac{\partial z}{\partial x} + 2hy + 2u + 2w\frac{\partial x}{\partial x} = 0 \quad (33)$$

At the origin, $x = y = z = 0$ and $\frac{\partial z}{\partial x} = 0$ $(tangent\ plane)$

Therefore from equation (33), *u = 0.*

Similarly by differentiating with respect to *y*, it can be shown that *v = 0.*

The precise equation can therefore be written as:

$$Ax^2 + By^2 + cz^2 + 2fyz + 2gzx + 2hxy + 2wz = 0. \quad (34)$$

We can obtain an approximation to this equation by making use of the Taylor's series:

$$f[(x + \delta x)(y + \delta y)]$$
$$= f(x, y) + \delta x\frac{\partial f}{\partial x} + \delta y\frac{\partial f}{\partial y} + \frac{1}{2!}\left[\delta x^2\frac{\partial^2 f}{\partial x^2} + 2\delta x\delta y\frac{\partial^2 f}{\partial x\partial y} + \delta y^2\frac{\partial f^2}{\partial y^2}\right]$$
$$+ higher\ order\ terms\ (neglected) \quad (35)$$

Differentiating equation (33) again with respect to *x:*

$$2A + 2cz\frac{\partial^2 z}{\partial x^2} + 2c\left(\frac{\partial z}{\partial x}\right)^2 + 2fy\frac{\partial^2 z}{\partial x^2} + 2g\frac{\partial z}{\partial x} + 2g\frac{\partial x}{\partial x} + 2gx\frac{\partial^2 z}{\partial x^2} + 2w\frac{\partial^2 z}{\partial x^2} = 0 \quad (36)$$

At the origin, $\frac{\partial z}{\partial x} = 0$ and substituting in equation (36) gives:

$$2A + 2w\frac{\partial z^2}{\partial x^2} = 0;\ \frac{\partial z^2}{\partial x^2} = -\frac{A}{w} \quad (37)$$

Similarly if we differentiate (32) twice with respect to y:

$$\frac{\partial^2 z}{\partial y^2} = -\frac{B}{w} \quad (38)$$

We can similarly differentiate equation (33) with respect to y, and simplify the result at the origin to give:

$$\frac{\partial^2 z}{\partial y\partial x} = -\frac{h}{w} \quad (39)$$

Substituting into Taylor's series, equation (35) and setting *z = f(x, y):*

$$f[(x+\delta x),(y+\delta y)] = z$$
$$= f(0,0) + x\frac{\partial z}{\partial x} + y\frac{\partial x}{\partial y}$$
$$+ \frac{1}{2!}\left[\frac{x^2\partial^2 z}{\partial x^2} + \frac{2xy\partial^2 z}{\partial x \partial y} + y^2\frac{\partial^2 z}{\partial y^2}\right] \quad (40)$$

We can therefore show that:

$$z = \frac{1}{2}\left(\frac{-ax^2}{w} - \frac{2hxy}{w} - \frac{by^2}{w}\right) \quad (41)$$

Equation (41) can be written in a general form as:

$$z = Ex^2 + Fy^2 + 2Hxy \quad (42)$$

If z is constant, equation (42) is an ellipse with its principle axes rotated with respect to the coordinate axes as shown in figure 5-2.

If the coordinate axes are aligned with the principle axes (global), the xy term will varnish. This is achieved by making the transformation:

$$x = Xcos\theta - Ysin\theta \; and \; y = Xsin\theta + Ycos\theta \quad (43)$$

The angle $\theta$ is given by:

$$\tan\theta = \frac{2H}{E-F} \quad (44)$$

Substituting in equation (42):

$$z = E(Xcos\theta - Ysin\theta)^2 + F(Xsin\theta + Ycos\theta)^2$$
$$= X^2(Ecos^2\theta + Fsin^2\theta + 2Hcos\theta sin\theta)$$
$$+ Y^2(ESin^2\theta + Fcos^2\theta - 2Hcos\theta sin\theta + XY(-2Esin\theta cos\theta + 2Fsin\theta cos\theta$$
$$+ 2Hcos^2\theta - 2Hsin^2\theta) \quad (45)$$

When $\theta$ is defined as in equation (44), the xy term vanishes and the equation with respect to the new coordinate axes is:

$$z = Constant1 \times X^2 + Constant2 \times Y^2 \quad (46)$$

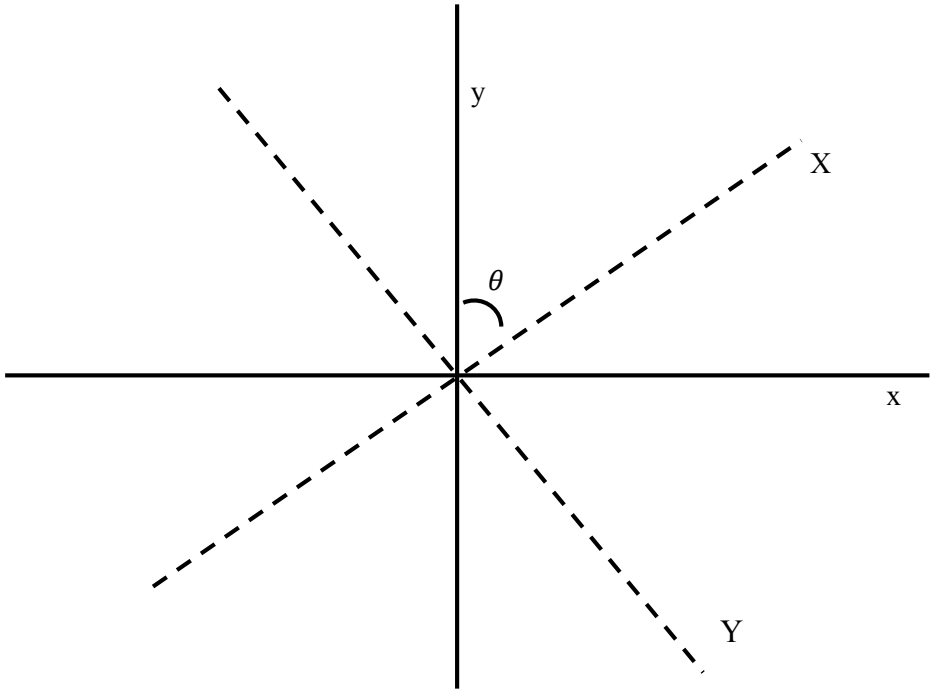


**Figure 5-2: Transformation of Axes**

We can then determine the constants in equation (46) in terms of the dimension of the respective bodies in contact. Let $R_1$ and $R_1$' be the principle radii of curvature of one of the bodies as shown in figure 5-3.

Writing equation (46) as below:

$$z = Ax^2 + By^2 \tag{47}$$

In the plane y=0, we have $Ax^2 = z$. If we assume a circular curvature in the y =0 plane, refer to figure 5-3 for illustration.

$$x^2 = 2R_1 z - z^2 \tag{48}$$

If the second order term of the small quantity z is ignored:

$$z = \frac{x^2}{2R_1} \tag{49}$$

Since also $z = Ax^2$,

$$A = \frac{1}{2R_1} \tag{50}$$

Similarly,

$$B = \frac{1}{2R'_1} \tag{51}$$

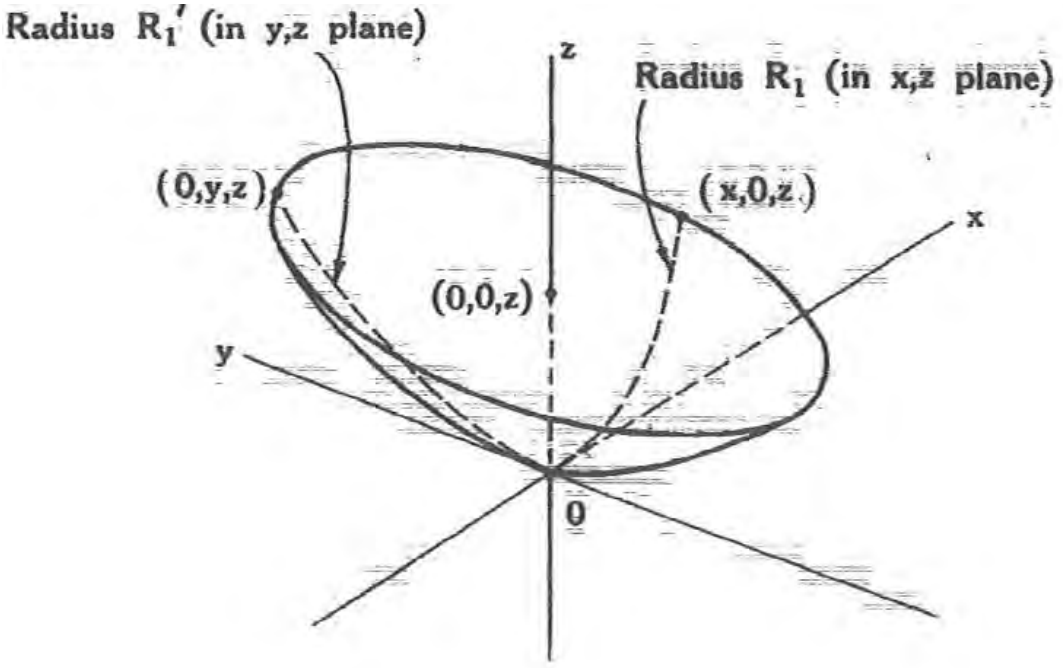


**Figure 5-3: Body with different orthogonal radii of curvature**
**(Source: Johnson, K. L., 1985)**

We can therefore write the equation of two body 1 and 2 in contact by substituting in equation (47):

$$z_1 = A_1{x_1}^2 + B_1{y_1}^2 = \frac{{x_1}^2}{D_1} + \frac{{y_1}^2}{D'_1} \tag{52}$$

$$z_2 = A_2{x_2}^2 + B_2{y_2}^2 = \frac{{x_2}^2}{D_2} + \frac{{y_2}^2}{D'_2} \tag{53}$$

$D_1$, $D'_1$, and $D_2$, $D'_2$ being twice the principle radii of curvature of the bodies respectively.

In order to obtain the compression effect between the two bodies, i.e. their mutual approach under an applied force, it is necessary to transform the coordinate axes of the two bodies to a

single coordinate system with different signs for the z axes and then combine equations (52) and (53).

Assuming a new common coordinate axes (normal to the z- axes) to be (***X, Y***), making the angles $\beta_1$ and $\beta_2$ with the independent axes $x_1$ and $x_2$ respectively, such that $\beta_1 + \beta_2 = w$. This is shown in figure 5-4 below.

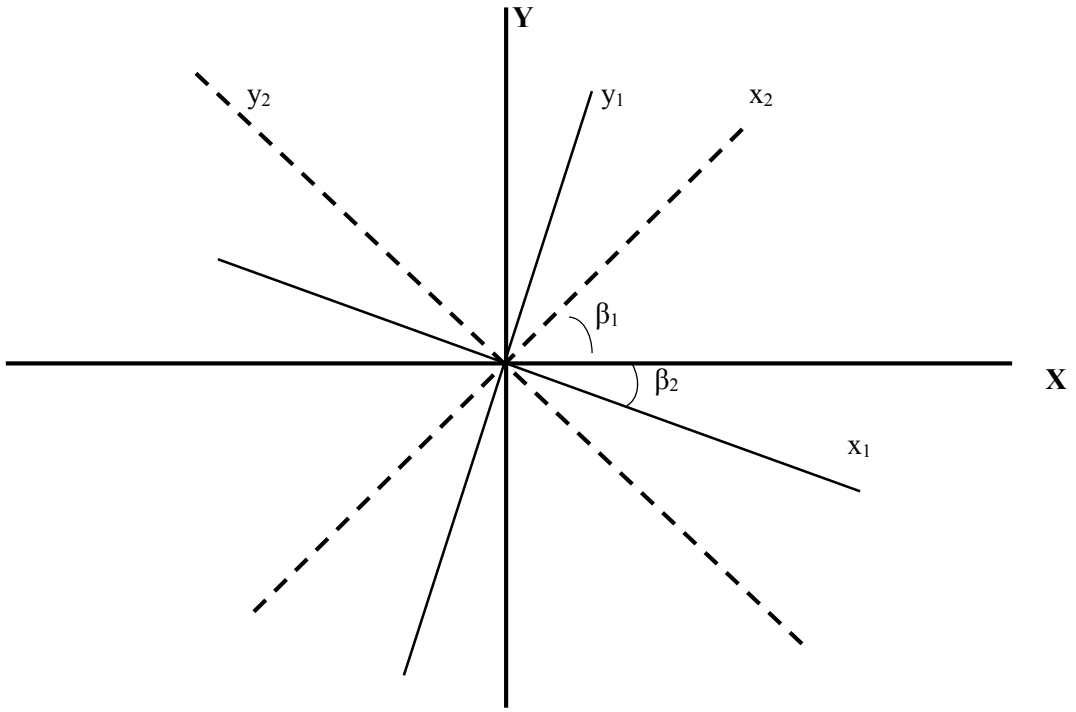


**Figure 5-4: Transformation of axes for deformation analysis**

$$x_1 = Xcos\beta_1 - Ysin\beta_1$$

$$y_1 = Xsin\beta_1 + Ycos\beta_1$$

$$x_2 = Xcos\beta_2 + Ysin\beta_2$$

$$y_2 = -Xsin\beta_2 + Ycos\beta_2 \quad (54)$$

Substituting in equations (52) and (53) we obtain:

$$z_1 = A_1(Xcos\beta_1 - Ysin\beta_1)^2 + B_1(Xsin\beta_1 + Ycos\beta_1)^2 \quad (55)$$

$$z_2 = A_2(Xcos\beta_2 - Ysin\beta_2)^2 + B_2(Xsin\beta_2 + Ycos\beta_2)^2 \quad (56)$$

Adding equations (55) and (56) and expanding the bracket terms gives:

$$z_1 + z_2 = X^2(A_1cos^2\beta_1 + A_2cos^2\beta_2 + B_1sin^2\beta_1 + B_2sin^2\beta_2) + 2XY(-A_1cos\beta_1sin\beta_1 + B_1sin\beta_1cos\beta_1 + A_2cos\beta_2sin\beta_2 - B_2sin\beta_2cos\beta_2) + Y^2(A_1sin^2\beta_1 + A_2sin^2\beta_2 + B_1cos^2\beta_1 + B_2cos^2\beta_2) \quad (57)$$

Now writing the coefficients of $X^2$ and $Y^2$ as A and B:

$$A = (A_1cos^2\beta_1 + A_2cos^2\beta_2 + B_1Sin^2\beta_1 + B_2sin^2\beta_2) \quad (58)$$

$$B = (A_1sin^2\beta_1 + A_2sin^2\beta_2 + B_1cos^2\beta_1 + B_2cos^2\beta_2) \quad (59)$$

Adding (58) and (59):

$$A + B = A_1 + A_2 + B_1 + B_2$$

Subtracting we get:

$$A - B = A_1cos2\beta_1 - B_1cos2\beta_1 + A_2cos2\beta_2 - B_2cos2\beta_2 = (A_1 - B_1)cos2\beta_1 + (A_2 - B_2)cos2\beta_2 \quad (60)$$

Equation (57) can be simplified further if the cross product (*xy*) in equation (57) is made to disappear yielding:

$$-(A_1 - B_1)sin2\beta_1 + (A_2 - B_2)sin2\beta_2 = 0 \quad (61)$$

Squaring equation (60) and (61) and adding:

$$(A - B)^2 = (A_1 - B_1)^2 + (A_2 - B_2)^2 + 2(A_1 - B_1)(A_2 - B_2)cos2\omega \quad (62)$$

Where $\omega = 2(\beta_1 + \beta_2)$.

Equation (57) may therefore be written as:

$$z_1 + z_2 = AX^2 + BY^2 \quad (63)$$

Where

$$A + B = \frac{1}{D_1} + \frac{1}{D'_1} + \frac{1}{D_2} + \frac{1}{D'_2} \quad (64)$$

$$(A - B)^2 = \left(\frac{1}{D_1} - \frac{1}{D'_1}\right)^2 + \left(\frac{1}{D_2} - \frac{1}{D'_2}\right)^2 + 2\left(\frac{1}{D_1} - \frac{1}{D'_1}\right)\left(\frac{1}{D_2} - \frac{1}{D'_2}\right)cos2\omega \quad (65)$$

Where ω is the angle between the original x-axes of the two bodies.

## 5.2 Contact modelling of the TERN conductor

The contact modelling of the TERN conductor was modelled using the theory of contact mechanics given above. The strands were modelled as circular helical curves contacting one another. The outer layer of the two contacting layers was taken as a convex surface, hence negative radius of curvature.

### 5.2.1 Equation of helical curves

The lay of strands in the ACSR tern conductor can be considered to be laid on a right circular cylinder. The surfaces of a cylinder can be developed into a plane enabling the development of some relationship between the centroid axis and other parameters.

The parametric equation of a circular helix is given by the equations:

$$x_s = R_s cos\theta_s$$

$$y_s = R_s sin\theta_s$$

$$z_s = R_s \theta_s tan\alpha \tag{66}$$

Where; $R_s$ is the mean radius of the strand about the helix centroid, $\alpha$ is the lay angle and $\theta_s$ is the angle of rotation. The lay angle is given by the equation:

$$tan\alpha = \frac{2\pi R_s}{P} \tag{67}$$

P is the lay length of the layer.

### 5.2.2 Strand to strand contact modelling

For modelling and drawing purposes in CAD software such as inventor fusion, the rotation angle is expressed in terms of a parameter,'t'. This parameter varies between 0 and 1 for one complete turn in a layer. The equation of the helix can then be written as:

$$x(t) = Rcos(2\pi t + \phi), y(t) = Rsin(2\pi t + \phi), z(t) = Pt \tag{68}$$

Where $R$ is radius about the helix axis, $P$ is the lay length and $\phi$ is the phase angle. Figure 5-5 shows the outer and mid-layer strand contact and the local and global coordinate systems. $\alpha_1$ and $\alpha_2$ are the lay angles for the inner and outer layer respectively of the contacting pair under consideration.

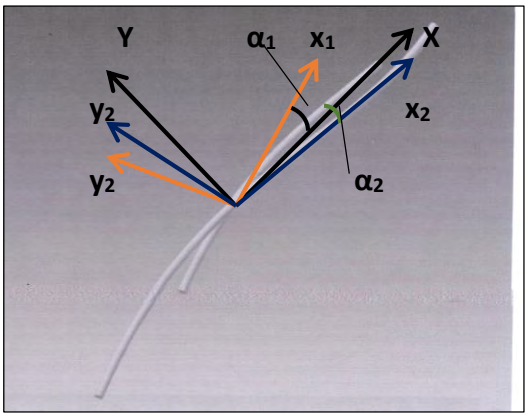


**Figure 5-5 Global and local axes for contact analysis**

The contact in this case is elliptical and each body can be described locally with orthogonal radii of curvature. We can find a radius ($R_c$) which to first order will represent a sphere in contact with plane as;

$$R_c = \sqrt{(R_a R_b)} \tag{69}$$

$R_a$ and $R_b$ are the major and minor axes of an equivalent toroid in contact with a flat plane respectively.

$$R_a = \frac{1}{(A+B)-(B-A)} \text{ And } R_b = \frac{1}{(A+B)+(B-A)} \tag{70}$$

$$A + B = \frac{1}{2}\left(\frac{1}{R_{1xx}} + \frac{1}{R_{1yy}} + \frac{1}{R_{2xx}} + \frac{1}{R_{2yy}}\right) \quad and$$

$$(B-A)^2 = \frac{1}{2}\left\{\left(\frac{1}{R_{1xx}} - \frac{1}{R_{1yy}}\right)^2 + \left(\frac{1}{R_{2xx}} - \frac{1}{R_{2xx}}\right)^2 + 2\left(\frac{1}{R_{1xx}} - \frac{1}{R_{2yy}}\right)\left(\frac{1}{R_{2xx}} - \frac{1}{R_{2yy}}\right)\cos(\alpha_1 + \alpha_2)\right\}$$

Where $A$ and $B$ are constants.

The curvature of a helix given by;

$$\rho = \frac{R}{sin\alpha} = \frac{1}{R_{xx}} \tag{71}$$

Substituting the wire radius and Equation (71) into (70) and taking the outer strand as a convex (negative curvature) we get:

$$A + B = \frac{sin^2\alpha_1}{2R_1} - \frac{sin^2\alpha_2}{2R_2} + \frac{1}{d_{w1}} + \frac{1}{d_{w2}} \text{ And } B - A = \left\{\left(\frac{sin^2\alpha_1}{2R_1} - \frac{1}{d_{w1}}\right)^2 + \left(\frac{sin^2\alpha_2}{2R_2} - \frac{1}{d_{w2}}\right)^2 + 2\left(\frac{sin^2\alpha_1}{2R_1} - \frac{1}{d_{w1}}\right)\left(\frac{sin^2\alpha_2}{2R_2} - \frac{1}{d_{w2}}\right) cos^2(\alpha_1 + \alpha_2)\right\}^{1/2} \tag{72}$$

Where, $R_{xx}$ and $R_{yy}$ are the orthogonal radii of curvature in the local x and y axes.

A Matlab ™ code was developed to calculate the equivalent radius $R_c$ for varying conductor parameters.

Conductor parameters such as lay length, lay cylinder outer radius, wire diameters, lay ratios and lay angles were measured for the conductor samples used in this research. The equivalent radius was then calculated using the developed Matlab™ code.

To explore the effects of the variation of these parameters above on the size of the fret marks and other contact mechanics parameters, the parameters were varied between their maximum value and minimum values and the equivalent radius calculated in each case.

Table 5-1 shows the value of the calculated equivalent radius for the various cases considered.

Equation (41) was used to calculate the equivalent radius for interlayer contact of the conductor samples analyzed and the standard TERN sample as per Aberdare Tern Design Specification (Refer to table 5-1 for design parameters values).

Table 5-1shows the calculated values of the equivalent radius for the two conductor samples and the Aberdare Cables recommended specification. For sample 01, exploratory calculation were also performed for various lay ratios recommended by SANS 182-2:2008 and BS 215 to further understand the effect of variation in lay ratio on the size of fret marks. In this exploratory study various combinations of the lay ratios for contacting layers were studied. For instance in the first row under exploratory investigations in table 1, Outer/Mid_Layer (Min/Max), shows the contact between the outer and mid layer with the lay ratios set to minimum and maximum recommended values in SANS 182-2:2008 for the outer and middle layer respectively. Table 5-2 givens the recommended ratios for various layers of ACSR conductors. An equivalent radius is then computed used in the FE simulations. Where, $\gamma$ is the

lay ratio. The terms $D_1$ and $P_1$ and $D_2$ and $P_2$, represent the mean diameter and the lay length for the convex and concave layer respectively. $R_c$ is the equivalent radius for the contacting pair, which is a theoretical radius of a deformable sphere in mathematical contact with a rigid flat plane**.**

**Table 5-1: Equivalent radii for different layers and lay ratios**

| | **Convex Layer** | | | **Concave Layer** | | | |
|---|---|---|---|---|---|---|---|
| **Sample1** | **$D_1$** | **$P_1$** | **$\gamma_1$** | **$D_2$** | **$P_2$** | **$\gamma_2$** | **$R_c$** |
| Outer/Mid_Layer | 23.500 | 293.000 | 10.902 | 16.733 | 249.775 | 12.425 | **7.956** |
| Mid/Inner_Layer | 16.733 | 249.775 | 12.425 | 10.120 | 189.000 | 14.000 | **10.303** |
| Inner/Core | 10.120 | 189.000 | 14.000 | 4.500 | 102.000 | 15.224 | **10.734** |
| **Sample 1 Exploratory** | | | | | | | |
| Outer/Mid_Layer(Min/Max) | 23.500 | 268.750 | 10.000 | 16.733 | 281.442 | 14.000 | **8.584** |
| Outer/Mid_layer(Min/Min) | 23.500 | 268.720 | 9.999 | 16.733 | 201.030 | 10.000 | **6.627** |
| Outer/Mid_layer(Max/Max) | 23.500 | 376.250 | 14.000 | 16.733 | 281.460 | 14.001 | **9.092** |
| Mid/Inner_Layer(Min/Max) | 16.733 | 201.030 | 10.000 | 10.120 | 202.500 | 15.000 | **8.308** |
| Mid/Inner_layer(Min/Min) | 16.733 | 201.000 | 9.999 | 10.120 | 135.000 | 10.000 | **7.360** |
| Mid/Inner_layer(Max/Max) | 16.733 | 301.545 | 15.000 | 10.120 | 202.514 | 15.001 | **10.901** |
| **Sample 2** | | | | | | | |
| Outer/Mid_Layer | 23.700 | 300.000 | 11.082 | 16.800 | 233.000 | 11.552 | **7.496** |
| Mid/Inner_Layer | 16.800 | 233.000 | 11.552 | 10.100 | 191.000 | 14.174 | **10.466** |
| Inner/Core | 10.100 | 191.000 | 14.174 | 4.150 | 126.000 | 19.688 | **19.718** |
| **Aberdare Sample Spec** | | | | | | | |
| Outer/Mid_Layer | 23.530 | 292.140 | 10.856 | 16.810 | 237.480 | 11.762 | **7.616** |
| Mid/Inner_Layer | 16.810 | 237.480 | 11.762 | 10.090 | 181.600 | 13.482 | **7.785** |
| Inner/Core | 10.090 | 181.600 | 13.482 | 4.500 | 102.000 | 15.111 | **11.217** |

**Table 5-2: Recommended lay ratios (SANS 182-2:2008)**

| Number of Wires in conductor | Lay Ratios | | | | | | | |
|---|---|---|---|---|---|---|---|---|
| | 6-wires layer | | 12-wire layer | | 18 wire layer | | 24-wire layer | |
| | min | max | min | max | min | max | min | max |
| 7 | 14 | 10 | - | - | - | - | - | - |
| 19 | 16 | 10 | 14 | 10 | - | - | - | - |
| 37 | 17 | 10 | 16 | 10 | 14 | 10 | - | - |
| 61 | 17 | 10 | 16 | 10 | 15 | 10 | 14 | 10 |

The variation in the equivalent radius for the two conductor samples examined and the one calculated from the Aberdare design specification are presented in the histogram below.

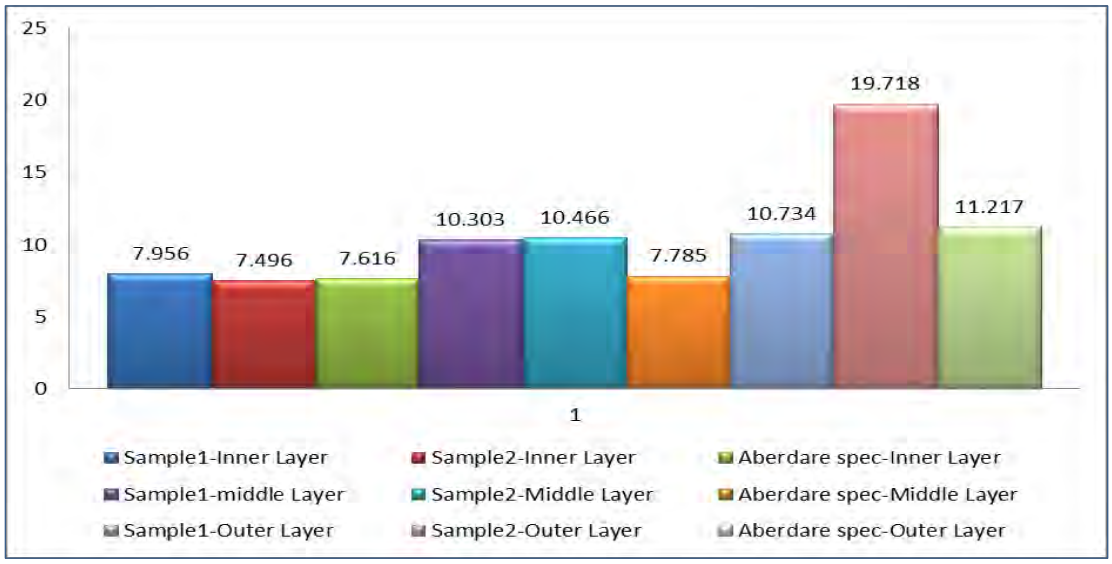


**Figure: 5-6: Variation of the equivalent radius in the conductor samples examined**

Despite the differences in actual conductor such as the lay ratio being small, the equivalent radius will reflect a significant difference which can be used to analyze how these changes can affect conductor quality.

As the lay ratios for the outer and mid layer of the sample 1 increase relative to those of the standard Aberdare specification, the equivalent radius also increases. A large equivalent radius results in a large and shallow contact surface and vice versa. This was evident from the observed fret marks which increased in size as you move from the outer layer going into the conductor inner layer. This relation can also be expressed by the equation below:

$$tan\alpha = \pi\left[\frac{1}{\gamma} - \frac{2R_w}{P}\right] \qquad \frac{-\pi}{2} < \alpha < \frac{\pi}{2} \tag{73}$$

From Equation (73) as the lay ratio increases, the lay angle reduces hence increasing the contact surface. Figure 8 shows the sizes for fret marks in different layers of the conductor. From Equation (73) and the table we can conclude that winding conductor layers such that there lay ratios are close to each other and both closer to the recommended maximum lay ratio with result in a high value of the equivalent radius. Winding the same layers with lay ratios close together but closer the minimum recommended lay ratio with will result in a smaller equivalent radius.

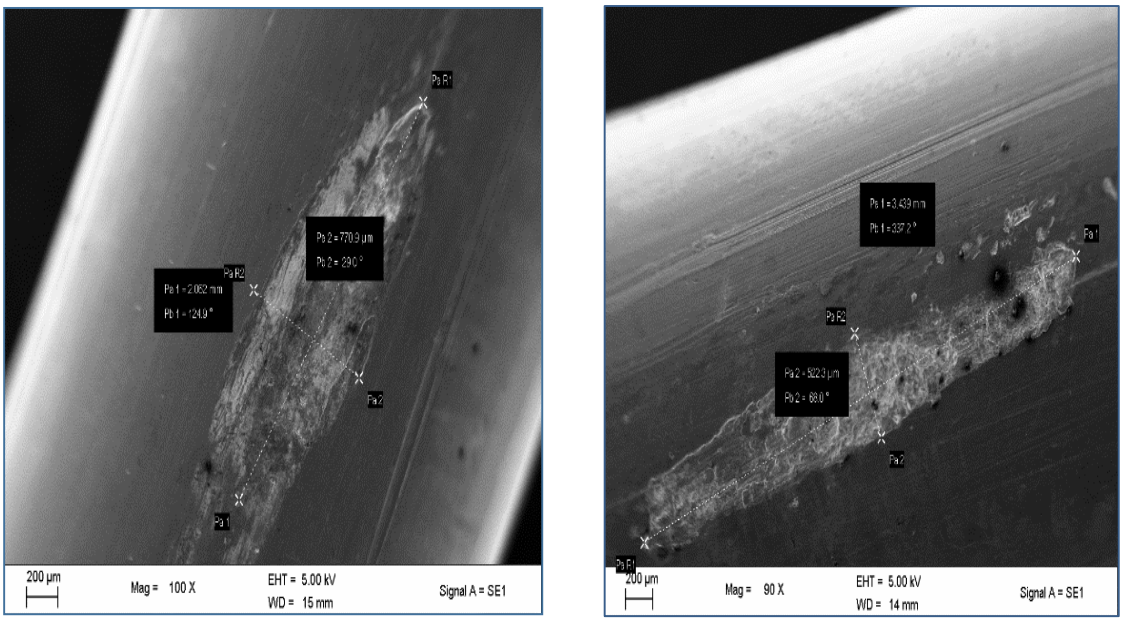


**(a)** **(b)**

**Figure 5-7: (a) Large and shallow mark for inner layer (b) Relatively smaller and deeper Fret mark for mid Layer**

### 5.2.3 Finite Element Analysis (FEA)

The equivalent sphere of radius $R_c$ was used for modeling in MSC Marc Mentat. A hemisphere was modeled as being in mathematical contact with a rigid flat plane. Both linear elastic and nonlinear analysis are presented. The quadrilateral element type 11 was used with large strain in plain strain and Von Mises failure criterion. For the nonlinear simulation the actual stress

strain and not the engineering stress-strain curve was used for the material properties. Figure 5-9 shows the stress-strain curve for aluminum alloy 6063 series (Atlas of Stress-Strain Curves, 2002).

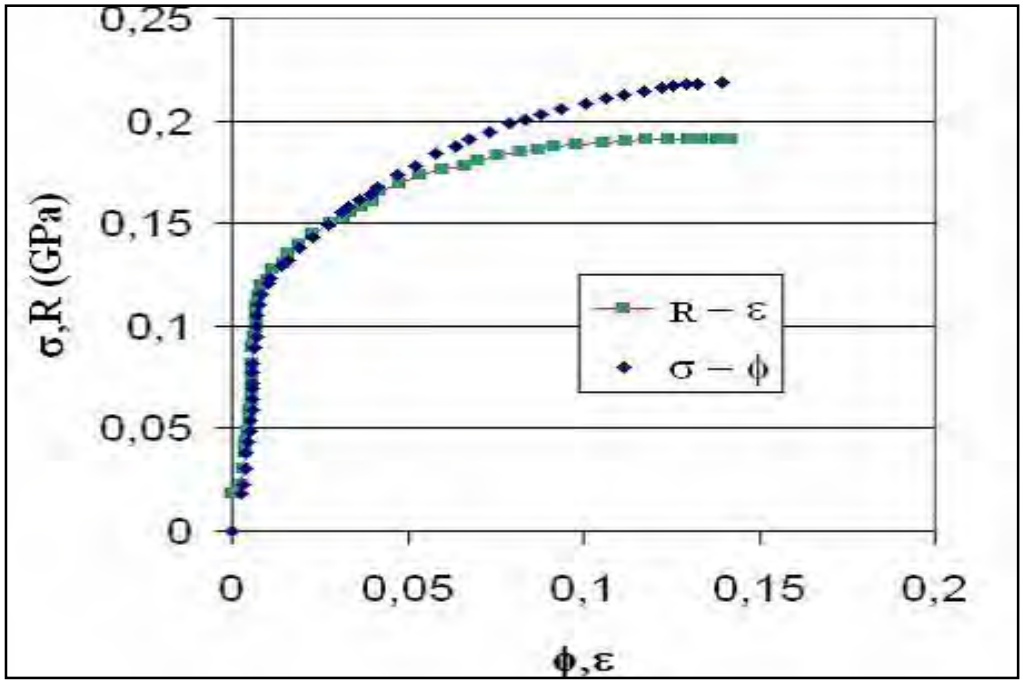


**Figure 5-8: 6063 Aluminum Alloy Stress-strain curve**

R-ε and ϕ-ε are the Engineering and Actual stress-strain curves respectively. The equivalent plastic stress can be expressed as:

$$\sigma_p = \sigma_y + K\epsilon^n \tag{74}$$

Where $\sigma_p$ is the plastic stress, $\sigma_y$ is the yield stress; $K$ is the strength factor, $\varepsilon$ is the strain and $n$ is the work hardening index. The Engineering stress-strain curve gives stress values which are slightly less than those obtained from the actual stress-strain curve. The linear curve on the other hand will give stress values which are too high relative to the actual curve.

The contact modulus is calculated from equation below:

$$\frac{1}{E_c} = \frac{1-v^2}{E_1} + \frac{1-v^2}{E_2} \tag{75}$$

Where $E_1$ and $E_2$ are the modulus of elasticity for the bodies in contact.

When $E_1$ is equal to $E_2$ we get:

$$E_c = \frac{E}{2(1-v^2)} \tag{76}$$

$E_c$ is the Contact modulus, $E$ is the Modulus of Elasticity for Aluminum (69GPa) and $v$ is the Poisson's ratio (0.31).With these values, a best fitting curve was fitted in equation (74) and plotted in MSC Marc Mentat as shown in figure 5-10. The best fitting equation was expressed as:

$$\sigma = \frac{35(1 + 8.543\varepsilon^{0.044})N}{mm^2} \tag{78}$$

The hemisphere used in the contact modelling was given the load boundary conditions shown in figure 5-9. The hemisphere was constrained by a fixed point on its top most point. The hemisphere was subjected to a ramping load imposed by moving flat plane. The displacement of the flat plane was set equal to the maximum interference observed in the outer and middle layer contacting pair.

A job was created for large strain analysis. Figure 5-10 shows the job set-up.

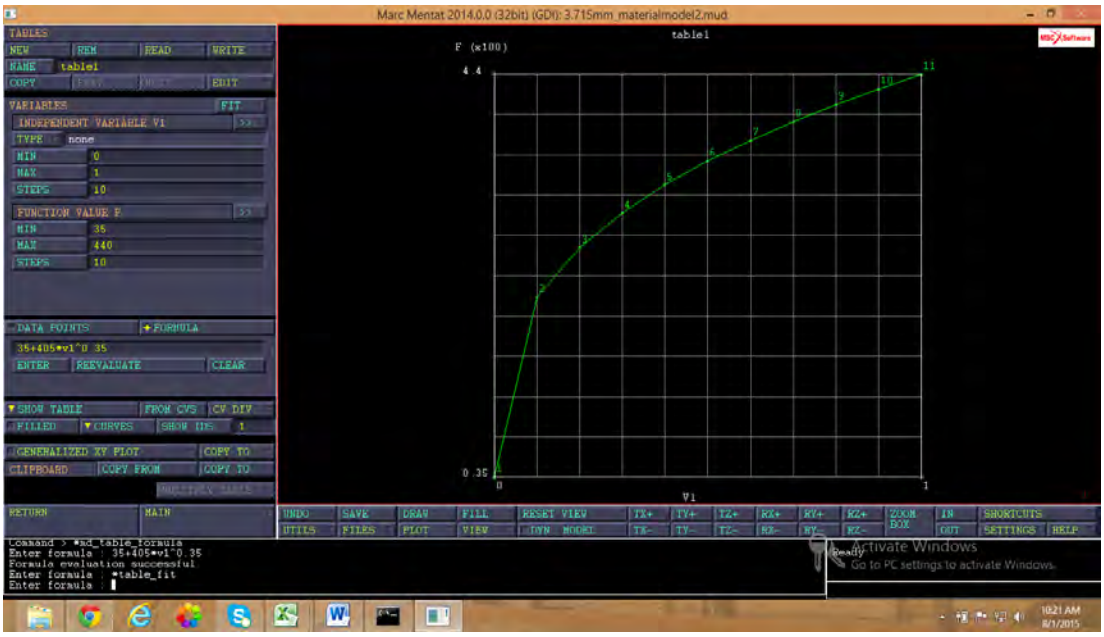


**Figure 5-9: Material properties in MSC Marc**

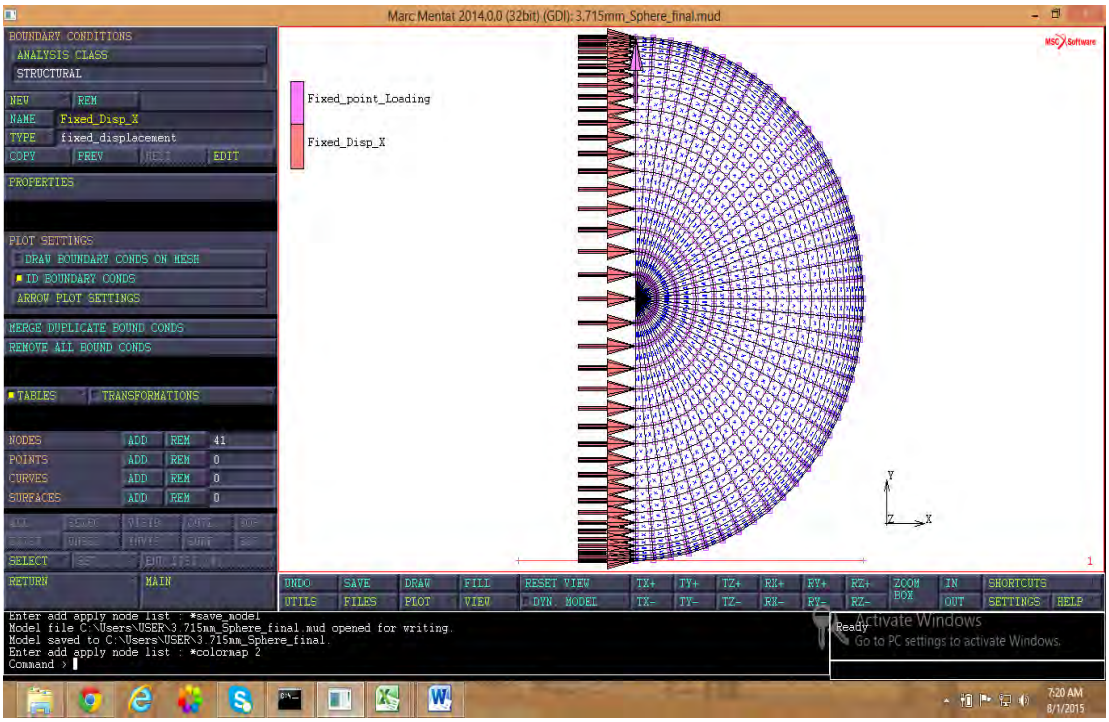


**Figure 5-10: Boundary Conditions (BCs)**

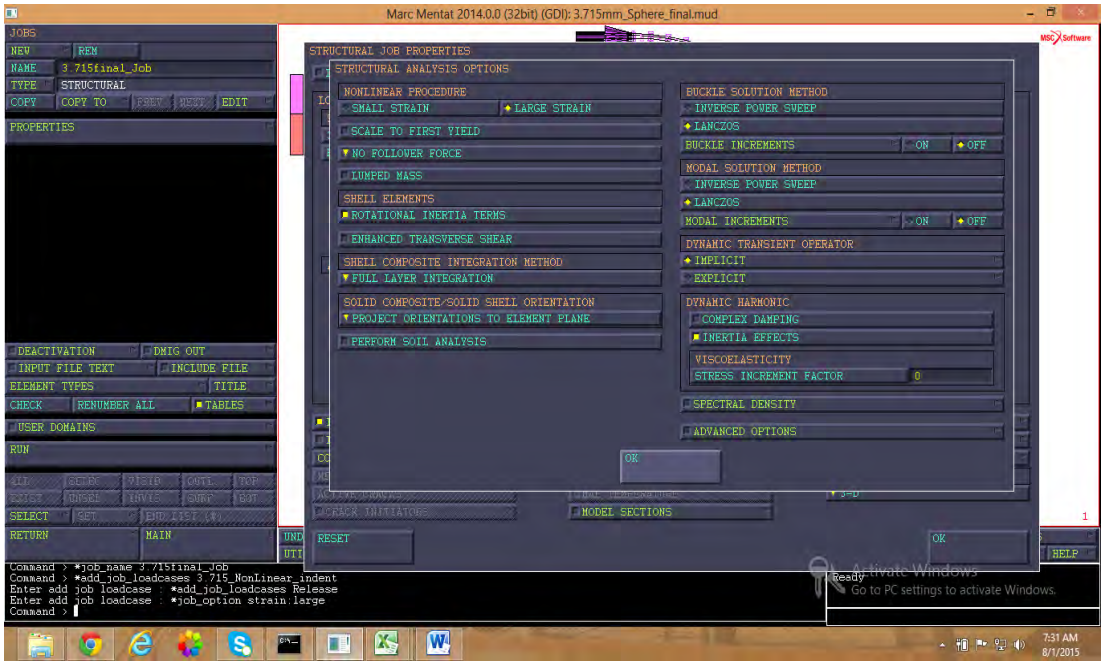


**(a) Job set-up**

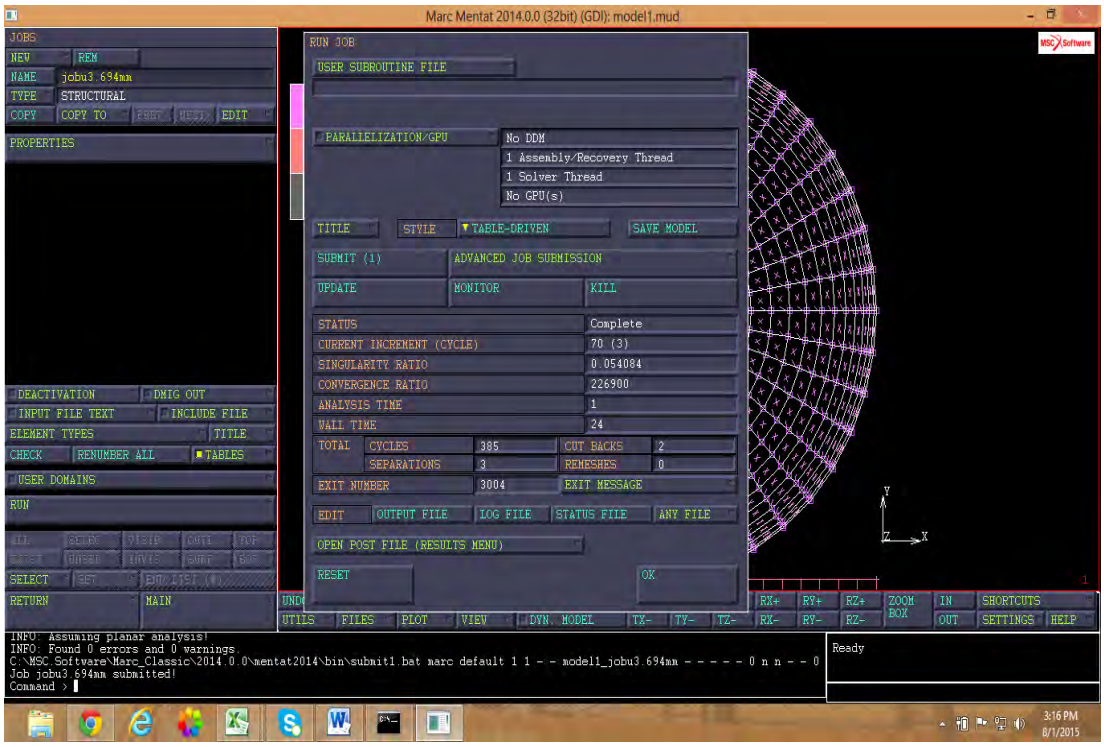


**(b)**

**Figure 5-11: Successful completion of a job**

The results from the post processing are shown in figure 5-13 (a) to (c).

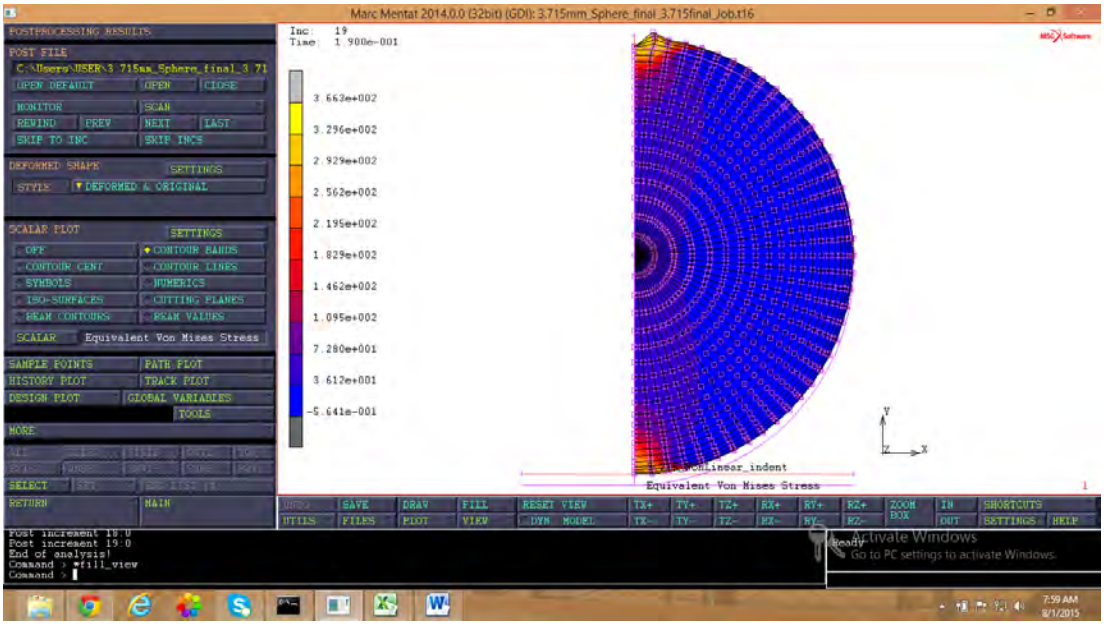


**(a) Equivalent Von Mises stress**

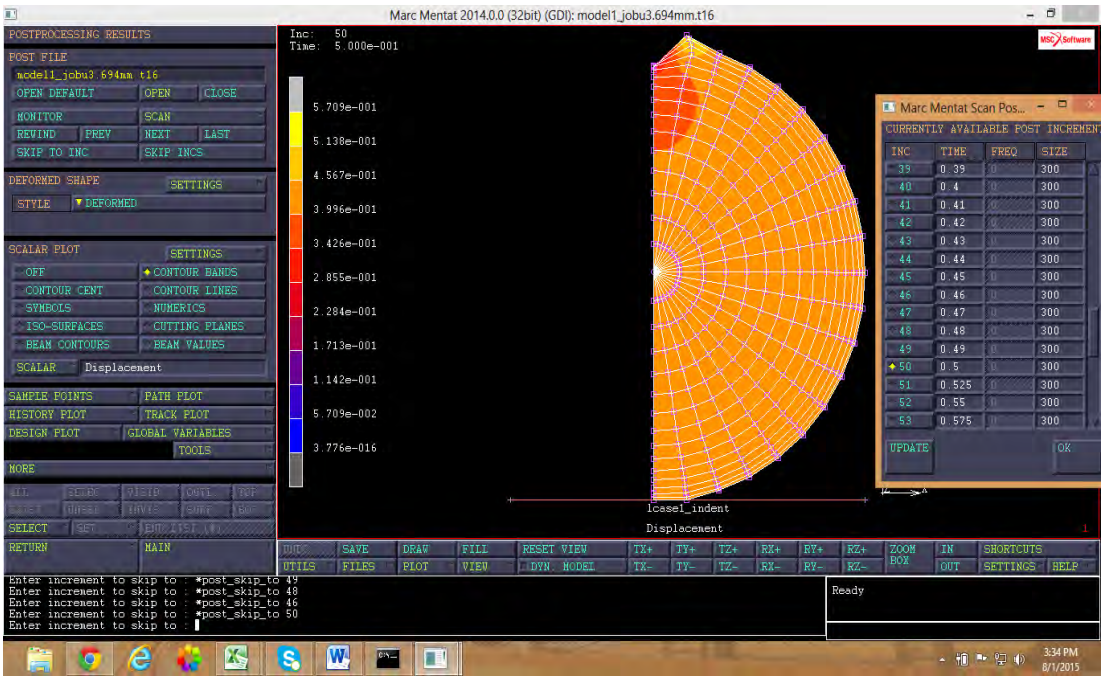


**(b) Displacement**

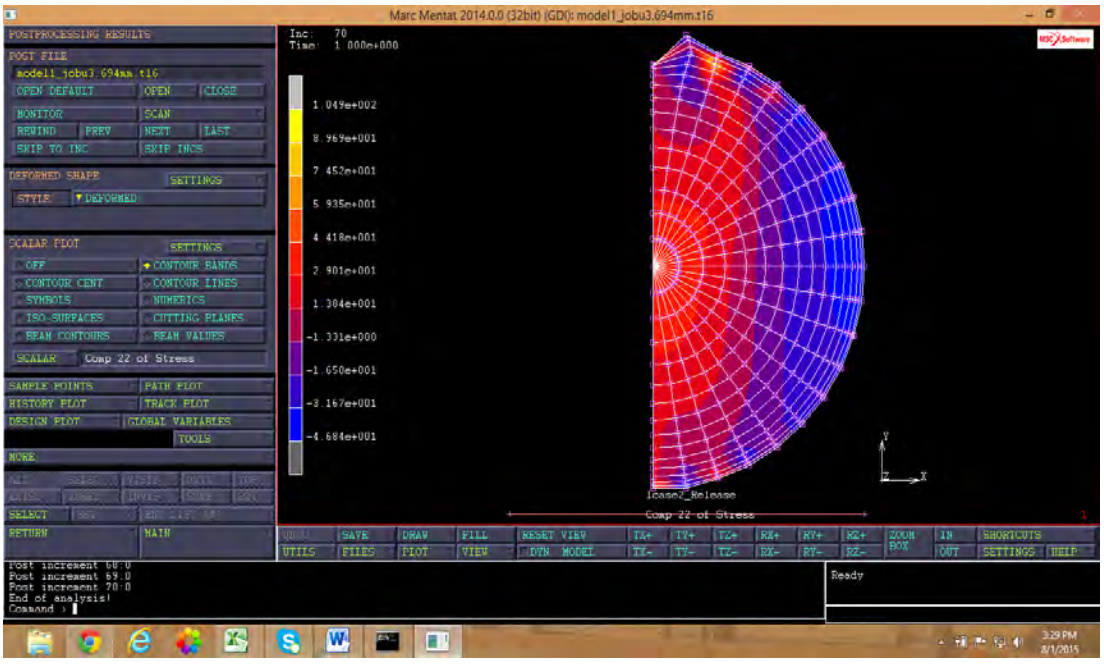


**(c) Hoop stress**

**Figure: 5-12: Results from the simulations**

The results of the simulations are summarized in the tables below. The simulations were carried out in 50 steps for the loading and 20 steps for the unloading. The tables only show the 50 loading steps.

**Table 5-3: Simulation results for sphere of equivalent radius of 7.956mm**

| Increment | Normal Contact force(N) | Stress(MPa) | Plastic strain |
|---|---|---|---|
| 1 | 28.37 | 42.25 | 1.297E-3 |
| 2 | 42.01 | 54.00 | 4.33E-3 |
| 3 | 49.95 | 62.05 | 7.793E-3 |
| 4 | 55.61 | 68.3 | 1.152E-2 |
| 5 | 60.13 | 73.52 | 1.535E-2 |
| 6 | 63.95 | 73.52 | 1.535E-2 |
| 7 | 67.28 | 82.07 | 2.321E-2 |
| 8 | 70.25 | 85.72 | 2.72E-2 |
| 9 | 72.95 | 89.07 | 3.123E-2 |
| 10 | 75.43 | 92.18 | 3.527E-2 |
| 11 | 77.73 | 95.09 | 3.935E-2 |
| 12 | 79.87 | 97.38 | 4.344E-2 |
| 13 | 81.89 | 100.4 | 4.755E-2 |
| 14 | 83.79 | 102.9 | 5.169E-2 |
| 15 | 85.59 | 105.2 | 5.584E-2 |
| 16 | 87.3 | 107.5 | 6.002E-2 |
| 17 | 88.94 | 109.7 | 6.421E-2 |
| 18 | 90.21 | 112.6 | 7.015E-2 |
| 19 | 90.49 | 116.4 | 7.833E-2 |
| 20 | 90.75 | 120.0 | 8.658E-2 |
| 21 | 90.98 | 123.5 | 9.49E-2 |
| 22 | 91.18 | 126.8 | 1.033E-1 |
| 23 | 91.36 | 129.9 | 1.118E-1 |
| 24 | 91.52 | 132.9 | 1.203E-1 |
| 25 | 91.66 | 135.8 | 1.29E-1 |
| 26 | 91.79 | 138.7 | 1.377E-1 |
| 27 | 91.90 | 141.4 | 1.464E-1 |
| 28 | 92.0 | 144.1 | 1.553E-1 |
| 29 | 92.02 | 146.7 | 1.642E-1 |
| 30 | 92.17 | 149.2 | 1.733E-1 |
| 31 | 92.23 | 151.7 | 1.826E-1 |
| 32 | 92.29 | 154.1 | 1.92E-1 |

| Increment | Normal Contact force | Stress | Plastic strain |
|---|---|---|---|
| 33 | 92.35 | 156.5 | 2.015E-1 |
| 34 | 92.39 | 158.8 | 2.111E-1 |
| 35 | 92.43 | 161.1 | 2.208E-1 |
| 36 | 92.46 | 163.4 | 2.306E-1 |
| 37 | 92.49 | 165.7 | 2.405E-1 |
| 38 | 92.51 | 167.9 | 2.505E-1 |
| 39 | 92.53 | 170.1 | 2.606E-1 |
| 40 | 92.54 | 172.3 | 2.708E-1 |
| 41 | 92.55 | 174.4 | 2.811E-1 |
| 42 | 92.56 | 176.5 | 2.915E-1 |
| 43 | 92.56 | 178.6 | 3.02E-1 |
| 44 | 92.56 | 180.7 | 3.126E-1 |
| 45 | 92.55 | 182.8 | 3.233E-1 |
| 46 | 92.55 | 184.8 | 3.342E-1 |
| 47 | 92.54 | 186.8 | 3.451E-1 |
| 48 | 92.53 | 188.9 | 3.562E-1 |
| 49 | 92.53 | 190.9 | 3.675E-1 |
| 50 | 92.51 | 192.9 | 3.789E-1 |

Table 5-4 shows the simulation for an equivalent sphere radius of 7.616mm corresponding to the Aberdare design specification. The table also gives the equivalent Von Mises stress for a linear elastic simulation to show how it compares to the nonlinear results. Refer to Annexure C for the data obtained for the other simulations of a different radius.

**Table 5-4: Linear elastic (LE) and nonlinear (NL) simulation results for a sphere of radius 7.616mm**

| Increment | Normal Contact force (NL) | Normal Contact force (LE) |
|---|---|---|
| 1 | 28.37 | 33.97 |
| 2 | 42.01 | 67.97 |
| 3 | 49.95 | 102.0 |
| 4 | 55.61 | 136.1 |
| 5 | 60.13 | 170.1 |

| Increment | Normal Contact force (NL) | Normal Contact force (LE) |
|---|---|---|
| 6 | 63.95 | 204.3 |
| 7 | 67.28 | 238.4 |
| 8 | 70.25 | 272.6 |
| 9 | 72.95 | 306.8 |
| 10 | 75.43 | 341.0 |
| 11 | 77.73 | 375.3 |
| 12 | 79.87 | 409.6 |
| 13 | 81.89 | 443.9 |
| 14 | 83.79 | 478.2 |
| 15 | 85.59 | 512.6 |
| 16 | 87.3 | 547 |
| 17 | 88.94 | 581.4 |
| 18 | 90.21 | 615.9 |
| 19 | 90.49 | 650.4 |
| 20 | 90.75 | 684.9 |
| 21 | 90.98 | 719.4 |
| 22 | 91.18 | 754 |
| 23 | 91.36 | 788.6 |
| 24 | 91.52 | 823.2 |
| 25 | 91.66 | 857.8 |
| 26 | 91.79 | 892.5 |
| 27 | 91.90 | 927.2 |
| 28 | 92.0 | 961.9 |
| 29 | 92.09 | 996.7 |
| 30 | 92.17 | 1031 |
| 31 | 92.23 | 1066 |
| 32 | 92.29 | 1083 |
| 33 | 92.35 | 1098 |
| 34 | 92.39 | 1113 |
| 35 | 92.43 | 1128 |
| 36 | 92.46 | 1143 |
| 37 | 92.49 | 1158 |
| 38 | 92.51 | 1174 |
| 39 | 92.53 | 1189 |

| Increment | Normal Contact force (NL) | Normal Contact force (LE) |
|---|---|---|
| 40 | 92.54 | 1204 |
| 41 | 92.55 | 1219 |
| 42 | 92.56 | 1234 |
| 43 | 92.56 | 1249 |
| 44 | 92.56 | 1264 |
| 45 | 92.55 | 1280 |
| 46 | 92.55 | 1295 |
| 47 | 92.54 | 1310 |
| 48 | 92.53 | 1325 |
| 49 | 92.53 | 1340 |
| 50 | 92.51 | 1356 |

Notice the large difference in the contact force between the linear elastic and the nonlinear simulation results. This difference can also be seen from figure 5-14. The deformation can be seen to be more in the nonlinear simulation (a). The linear elastic simulation used 50 increments for the simulation and not the 70 used for the nonlinear. This is because for the linear elastic the deformation can only be seen as the load is applied, which is the first 50 increments and will regain its original shape when the load is removed in the last 20 steps

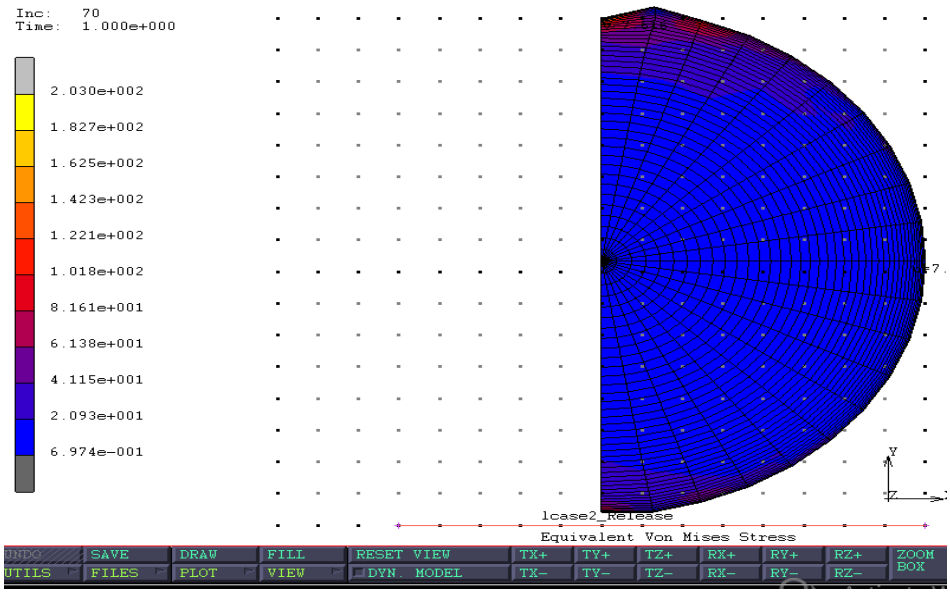


**(a) Nonlinear simulation result**

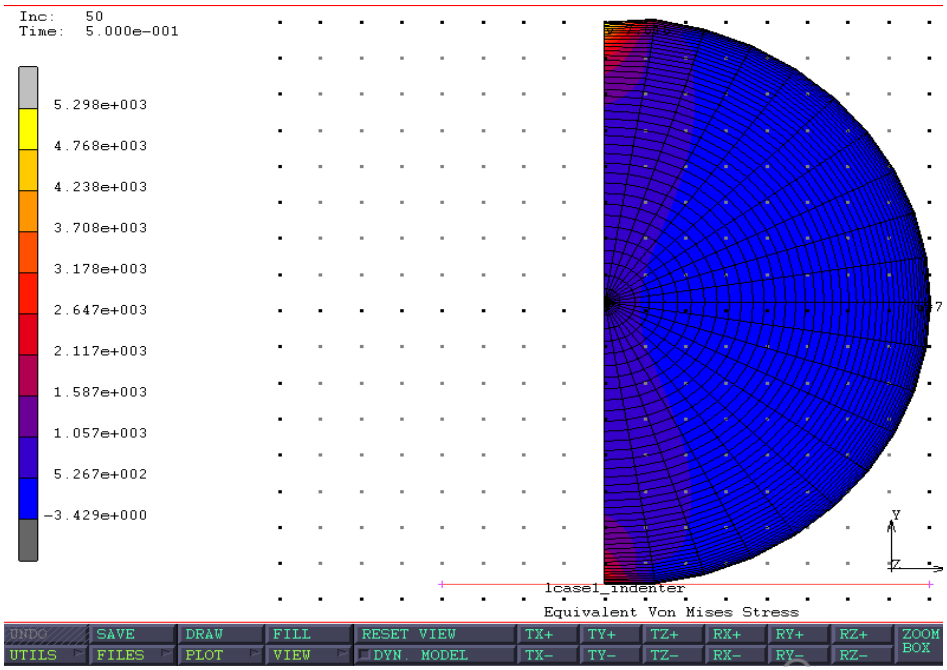


**(b) Linear elastic simulation result**

**Figure 5-13: (a) Nonlinear result (b) linear Elastic result**

The relationship between the equivalent sphere radius and the Von Mises stress, plastic strain, fret mark dimensions and the normal contact force for the nonlinear simulation are explained below.

### 5.2.3.1 Total equivalent plastic strain

A plot of the equivalent radius versus the total equivalent plastic strain is shown in figure 5-14. There is very strong linear correlation between the equivalent radius and the plastic strain with a correlation constant of 0.915. The plastic strain decreases linearly with the increase in the equivalent radius. This results implies very deep fret marks for a lower value of the equivalent radius. This supports the observation presented above.

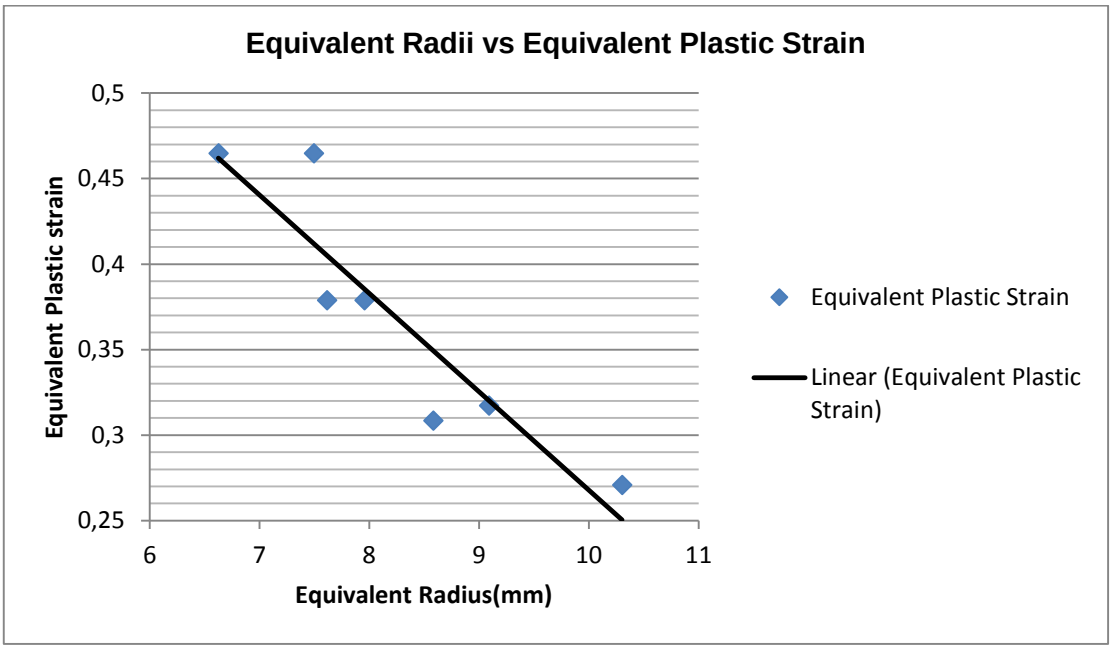


**Figure 5-14: Equivalent radius vs Total Equivalent plastic strain**

### 5.2.3.2 Von Mises stress

The Von Mises stress shows a strong linear correlation with the equivalent radius. It decreases linearly with an increase in the equivalent radius. The correlation constant is 0.926. This implies that for a smaller equivalent radius, there is more stress at the contact surfaces which will result in high plastic strain and hence more deformation. For the simulated outer layer, there exist a theoretical equivalent radius of 26.74mm which will result in zero contact stress and hence zero plastic strain. Winding the conductor such that the equivalent radius is closer to this value will result in better conductor quality. Fig. 5-15 shows how the Von Mises stress varies with the equivalent radius.

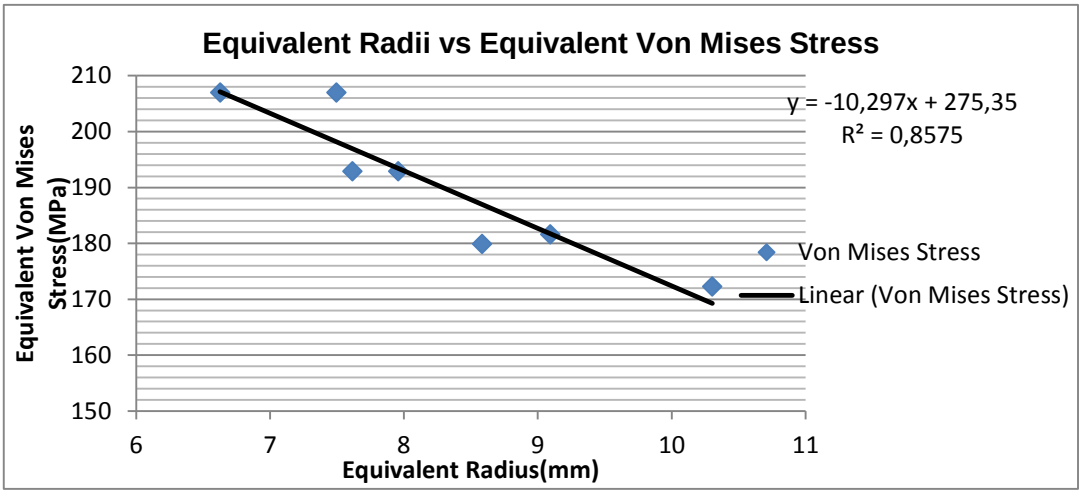


**Figure 5-15: Equivalent radius vs Equivalent von mises stress**

### 5.2.3.3 Normal contact force

The normal contact force increase linearly with increase in the equivalent radius. The relationship is however dependant upon the value of interference. Strong correlation exist between the two variables with least correlation constant being 0.949. A small equivallent radius results in a high normal contact force. Figure 5-16 shows the relationship bewteen the normal contact force and the equivalent radius.

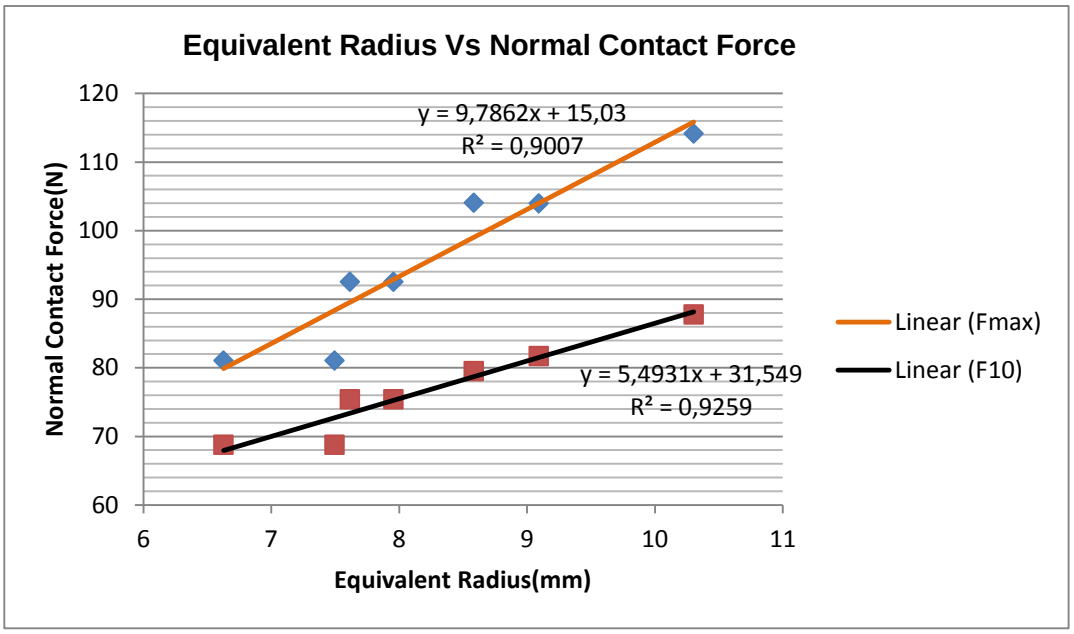


**Figure 5-16: Equivalent Radius vs Normal contact force**

### 5.2.3.4 Effect of equivalent radius on the normal contact force

As the equivalent radius increases, the normal normal contact force reduces for the same displacement (interference). Figure 5-17 shows this relationship. A higher equivalent radius is therefore desirable to reduce the contact force and hence the plastic strain for better conductor quality. The linaer elastic model gives very high values such that it can not be used accuracy.

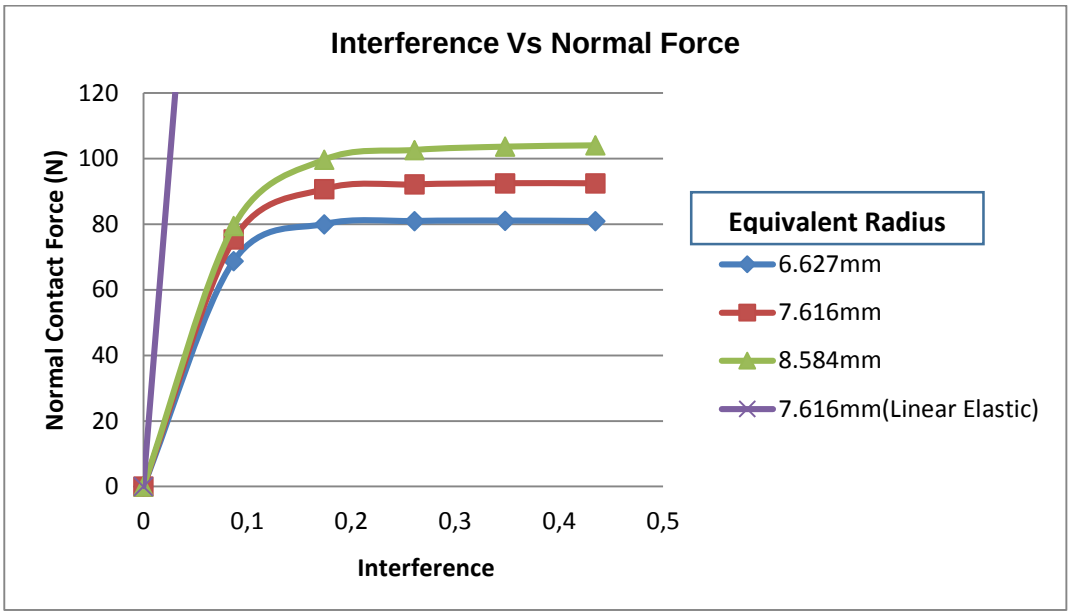


**Figure 5-17: Inference per layer vs. Normal contact force**

### 5.2.3.5 Fret mark dimensions versus equivalent radius

The relationship between the fret mark and the equivalent radius has a parabolic appearance with a correlation constant of 0.947. This relationship suggests that there exist a maximum fret mark length which can be obtained for a given tension for a particular set-up. Refer to figure 5-19. A straight line can also be fitted on this data although it gives a weaker correlation.

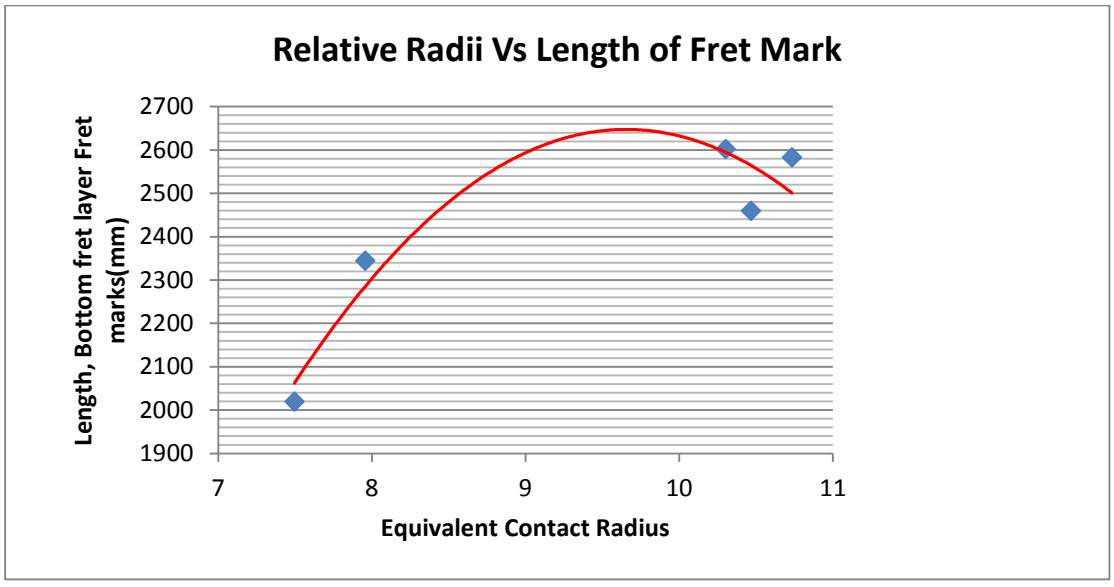


**Figure 5-18: Equivalent Radius vs. Length of fret mark**

The depth of the fret marks decreased as the equivalent radius increased. This is depicted in figure 5-20. If the two outlying points are neglected based on the assumption that there was an error in measurement, a strong linear correlation is observed between the equivalent radius and the depth of the fret marks with a correlation constant of 0.9996. From this linear regression, a hypothetical equivalent radius of 12.772mm would result in zero indentation depth at the winding tension used for this conductor sample. If however the points are taken into account, the data shows a large scatter and no simple relationship can be established.

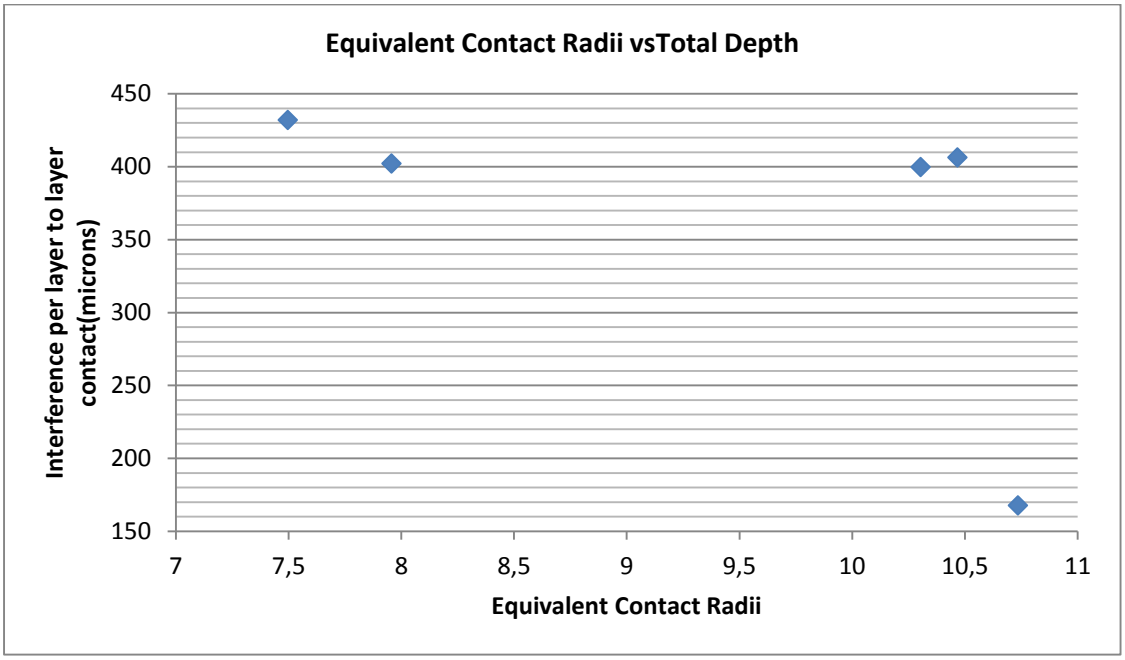


**Figure 5-19: Equivalent Radius versus fret mark depth**

From the results, it can be seen that the outer layer will have the deepest marks as it has the smallest equivalent radius. The equivalent radius is directly proportional to the difference between the curvatures (reciprocal of equivalent radii of curvature) of the contacting surfaces. Because the lay angles are generally small, the size of the curvature can be said to be inversely proportional to the radius of the helix about the conductor axis as given in Eq. (9). Therefore the outer layer having the largest value or the helix radius will have the smallest curvature and hence would give the smallest equivalent radii. The middle layer is more susceptible to failure as it has mark on both sides. On average the middle layer has total depth in excess of 420microns, which is the sum of depths of the marks on either side (top and bottom) for the samples analyzed. This reduces the effective length of crack propagation by 12%. This implies that the crack has a shorter cross section of the strand to propagate before it reaches the critical length.

### 5.3 Inner conductor contact model

The normal contact force from the FE model was used to calculate the tension applied to the conductor wire to obtain the observed average interference. The inner conductor contact mechanics is model as massless strands connected by springs. Figure 5-21 shows the model used to calculate the tension. In figure 5-21 (a), *K* is the vertical component of the radial contact stiffness *k*. The forces pushing each layer downwards are designated as $F_1$, $F_2$, $F_3$, $F_4$ and the corresponding displacement as $X_1$, $X_2$, $X_3$ and $X_4$. Using the finite element method, the stiffness and the forces causing the displacement can be expressed in matrix form:

$$F = KX \tag{79}$$

Where F is the force, K is the stiffness and X is the displacement. In terms of the vertical stiffness, K, the matrix equation is:

$$\begin{bmatrix} K_1 & -K_1 & 0 & 0 \\ -K_1 & K_1+K_2 & -K_2 & 0 \\ 0 & -K_2 & K_2+K_3 & -K_3 \\ 0 & 0 & -K_3 & K_3 \end{bmatrix} \begin{bmatrix} X_1 \\ X_2 \\ X_3 \\ X_4 \end{bmatrix} = \begin{bmatrix} F_1 \\ F_2 \\ F_3 \\ F_4 \end{bmatrix} \tag{80}$$

At Equilibrium $X_4$ is zero. The interference per layer is given by the difference in displacements i.e. for $a_1$ (outer vs. middle layer); $a_1 = X_1 - X_2$

In figure 5-21(b) the symbols; $S_1$, $S_2$ and $S_3$ denote the strands of the outer layer that are contacting the layer beneath. The radial contact force and displacement are resolved and their vertical components expressed as an equivalent stiffness.

Figure 5-21 shows the outer layer strands contacting the layer underneath. $\phi_i$ is the angle between the strands in the layer and for compact packing is given by ;

$$\emptyset_i = \frac{2\pi}{n_i} \tag{81}$$

Where $n_i$ is the number of strands in the layer, *i* is layer number with *i*=1 being the outer layer. Resolving all the radial stiffness in the vertical direction, we can obtain the following value of total vertical stiffness for a finite length of the conductor, for $K_1$;

$$K_{1total} = K_1 + K_1 cosn\emptyset_1 + K_2 cos\emptyset_2 + \cdots + K_{ni} cos\emptyset_{ni} \tag{82}$$

Where $K_{1total}$ is the total vertical stiffness in the vertical direction for a finite length of the conductor. Equation (47) can be expressed in compact form as:

$$K_{1total} = K_1 \sum_{0}^{ni} cosn_i \emptyset_{ni} \tag{83}$$

All the three radial stiffness can be expressed in a similar form and substituted in equation (45) to give:

$$\begin{pmatrix} F_1 \\ F_2 \\ F_3 \\ F_4 \end{pmatrix} = \begin{bmatrix} K_1 \sum_{0}^{n_{i1}} cosn\emptyset_1 & -K_1 \sum_{0}^{n_{i1}} cosn\emptyset_1 & 0 & 0 \\ -K_1 \sum_{0}^{n_{i1}} cosn\emptyset_1 & K_1 \sum_{0}^{n_{i1}} cosn\emptyset_1 + K_2 \sum_{0}^{n_{i2}} cosn\emptyset_2 & -K_2 \sum_{0}^{n_{i2}} cosn\emptyset_2 & 0 \\ 0 & -K_2 \sum_{0}^{n_{i2}} cosn\emptyset_2 & K_2 \sum_{0}^{n_{i2}} cosn\emptyset_2 + K_3 \sum_{0}^{n_{i3}} cosn\emptyset_3 & 0 \\ 0 & 0 & -K_3 \sum_{0}^{n_{i3}} cosn\emptyset_3 & K_3 \sum_{0}^{n_{i3}} cosn\emptyset_3 \end{bmatrix} \begin{bmatrix} X_1 \\ X_2 \\ X_3 \\ X_4 \end{bmatrix}$$

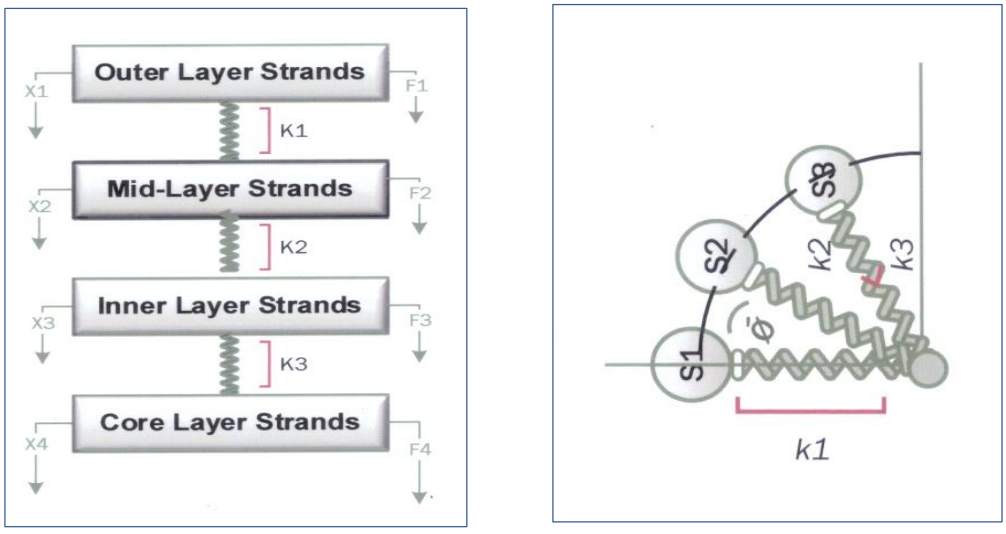


**(a)** **(b)**

**Figure 5-20: Inner Conductor contact mechanics model**

From this matrix equation:

$$F_1 = (X_1 - X_2)K_1 \sum_0^{n_{i1}} cosn\emptyset_1 \tag{84}$$

$$F_2 = K_1 \sum_0^{n_{i3}} cos\emptyset_2 \, (X_3 - X_2) + K_3 X_3 \sum_0^{n_{i3}} cos\emptyset_3 \tag{85}$$

$$K_4 X_3 \sum_0^{n_{i3}} cos\emptyset_3 = F_4 \tag{86}$$

If we consider a finite length of the conductor, *L*, the ratio of the number of wires in each layer in this length is:

$$\frac{sin\alpha_1}{d_1} : \frac{sin\alpha_2}{d_2} : \frac{sin\alpha_3}{d_3}$$

For $n_x$ wire in the outer layer, the contact force per fret mark ($_{F1c}$) is given by;

$$F_{1c} = (F_1)\left(\frac{d_2 sin\alpha_1}{n_x d_1 sin\alpha_2}\right) \quad \text{With } n_{il} = n_x \tag{87}$$

$F_1$ is the normal contact force per fret mark obtained from the FEA simulations.

From the inner conductor contact model by Hruska, 1953 the Tension conductor is given by:

$$T = \frac{f_i(AE)}{A_i E_i cos^2\alpha_i},\ f_i = \frac{F_{1c}}{\sin\alpha} \text{ and } AE(axial\ Stiffness) = E_c A_c + \sum_1^m n_i A_i E_i cos^3\alpha_i \tag{89}$$

Where *m* is the layer number, *A* is cross section area and *E* is modulus of elasticity. To calculate the force per aluminum wire one needs to find the tension in the core alone given by:

$$F_c = \frac{A_c E_c}{(AE)} T \tag{90}$$

Where; $A_c$ and $E_c$ are the cross section area and the Young Modulus of the core respectively.

# 6. Fatigue crack propagation

Determination of the fatigue crack propagation curve is an essential part of the fracture mechanics design approach. Residual strength calculations do have shortcomings, but the prediction of crack propagation is even less accurate, despite the vast amount of research conducted in this subject (Broek D., 1986). For compound structures such as the transmission line conductors very little data is available for the prediction of the crack growth. This chapter is therefore dedicated to modelling of the fatigue data using Linear Elastic Fracture Mechanics (LEFM).

## 6.1 Crack growth and the stress intensity factor

In the elastic case the stress intensity factor is sufficient parameter to describe the whole stress field at the tip of the crack. When the size of the plastic zone is small compared to the crack length, the stress intensity factor is a good indication of the stress environment of the crack tip. If two different cracks have the same stress environment, they will behave in the same manner and show equal crack growth rate. The rate of fatigue crack growth is then governed by the stress intensity factor. This can be expressed mathematically as shown in equation (91).

$$\frac{da}{dN} = f(\Delta K) = f\{(S_{max} - S_{min})\sqrt{\pi a} \tag{91}$$

Where:

$\Delta K$ is the Stress intensity factor range

$S_{min}$ and $S_{max}$ are the minimum and maximum stresses in the cycle

$a$ is the crack length

$N$ is the number of fatigue cycles

Paris, Gomez and Anderson where the first to point this out (Broek D, 1986). Equation (91) is sometimes expressed as a simple power function:

$$\frac{da}{dN} = C(\Delta K)^n \tag{92}$$

In this equation, C and n are supposed to be material constants. A double logarithmic plot of $\frac{da}{dN}$ versus $\Delta K$ would then be a straight line. In this law.

Equation (92) is a case of LEFM and does not fully represent reality. Actual fatigue data falls on an S-Shaped curve which can be broken down into three regions.

- **Region 1-**Non continuum behaviour

  In this region, the behaviour of the crack is largely influenced by the following:

  I. Microstructure
  II. Mean stress
  III. Environment

- **Region 2-**Continuum behaviour

  This region is the linear part of the double logarithmic plot the power law (Paris law). For a failed metallic material in this region, there are usually striations on the failed surface. This region is characterized by the following:

  I. Small to large influence of the microstructure depending on the material
  II. Large influence of a certain combinations of the environment, mean stress, and frequency.

- **Region 3**:- Static mode behaviour

  This is the unpredictable region in the curve and it's associated with features such as cleavage, intergranular and dimples. This region has the following characteristics:

  I. Large influence of the microstructure, mean stress and thickness
  II. Little influence of the environment

In region 1, there exist a threshold stress intensity factor $\Delta K_{TH}$ at which cracks propagate at a very slow rate or do not propagate at all. Above this value of the stress intensity factor, the crack propagates relatively rapidly with increasing stress intensity factor range.

In region 2 the crack growth rate, *da/dn* is a power function of $\Delta K$. Finally in region 3, the crack growth curve raises rises to an asymptote where maximum stress intensity factor, $K_{max}$ becomes equal to the critical stress intensity factor $K_{c,}$ the fracture toughness of the material.

Many equations have been proposed to try and describe the crack growth curve. The mostly widely known is the Paris equation:

$$\frac{da}{dN} = C(\Delta K)^m \tag{93}$$

Forman proposed the following well known improved equation:

$$\frac{da}{dn} = \frac{C(\Delta K)^m}{(1-R)K_c - \Delta K} \tag{94}$$

$R$ is the ratio of the maximum stress to the minimum stress.

Many variations of the Paris equation, exist but the analysis used in this research was based on the Paris law itself.

### 6.2 Modelling of the fatigue data

The modelling of the fatigue data was based on the assumption of centre crack on an infinite specimen as most of the cracks were observed to be transverse to the direction of the fret marks measured on the major axis. In this case the stress intensity factor range can be calculated using as:

$$\Delta K = \Delta\sigma\sqrt{\pi a}\sqrt{\frac{D}{\pi a}}\tan\left(\frac{\pi a}{D}\right) \tag{95}$$

Where:

$\Delta\sigma$ is the stress range

$D$ is the diameter of the strand

$a$ is the crack length.

This equation holds for the condition:

$$\frac{a}{D} < 0.25$$

Using the fatigue crack data from tables 4-3 and 4-4 respectively, the stress intensity factor was calculated and used in the modelling of the fatigue data. Table 6-1 shows the values of the calculated stress intensity factors.

**Table 6-1: Stress Intensity factors for sample 1**

| Location (Linear distance)-mm | Layer | Crack length-microns | Strain-microstrains | Stress-MPa | Actual Stress | Delta K | logK | lg(da/dn) |
|---|---|---|---|---|---|---|---|---|
| **15** | Outer Layer | 485,3 | 680 | 47,60 | 35,7 | 1444,606986 | 3,159749711 | -11,01296 |
| **90** | Midlayer | 167,3 | 158 | 10,90 | 8,175 | 188,1912549 | 2,274599438 | -11,475474 |
| **5** | Mid-layer | 84,33 | 895 | 61,76 | 46,31625 | 754,6976203 | 2,877772981 | -11,772988 |
| **45** | Mid-layer | 173,6 | 150 | 10,35 | 7,7625 | 182,0858103 | 2,260276103 | -11,45942 |
| **60** | Mid-layer | 222,5 | 10 | 0,69 | 0,5175 | 13,78180958 | 1,139306245 | -11,35164 |
| **60** | Mid-layer | 102,9 | 10 | 0,69 | 0,5175 | 9,319333019 | 0,969384831 | -11,686555 |
| **85** | Mid-layer | 176,8 | 115 | 7,94 | 5,95125 | 140,9029112 | 2,148919966 | -11,451488 |
| **80** | Mid-layer | 115,1 | 75 | 5,18 | 3,88125 | 73,95085918 | 1,868943224 | -11,637895 |
| **90** | Mid-layer | 81,19 | 165 | 11,39 | 8,53875 | 136,5090712 | 2,135161512 | -11,789467 |

From the table log K is the logarithm of the stress intensity factor range and the last column shows the logarithm of the rate of crack growth. The actual stresses where calculated using the assumption of bending solid bar. The Euler-Bernoulli equation was used to approximate the stresses at various interfaces using the measured stresses on the surfaces.

$$M = \frac{\sigma I}{y} \tag{96}$$

Where:

$M$ is the moment

$I$ is the second moment of area

$\sigma$ is the stress

$y$ is the distance from the centre of the conductor core to the point where the stress has to be measured.

Using the Paris law, a double logarithmic plot of the data was done and is shown in figure 6-1 below.

The double logarithm plot will give a straight line of the form:

$$\log \frac{da}{dn} = \log C + m \log \Delta K \tag{97}$$

A straight line whose gradient is $m$ and intercept is log C can be fitted in the fatigue data.

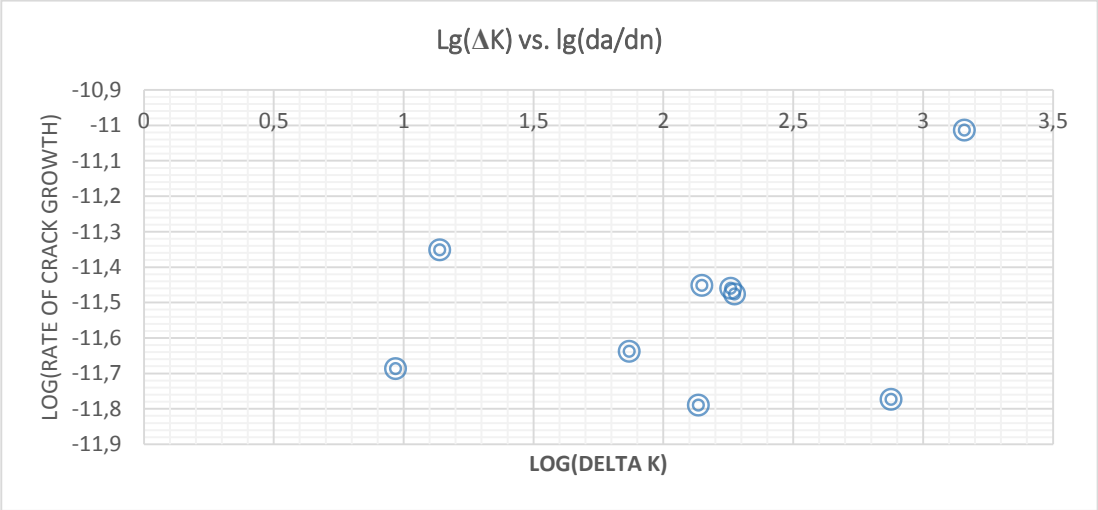


**Figure 6-1: Log-log plot of fatigue data for sample 1**

A straight line of best fit was then fitted into this data and is shown in figure 6-2.

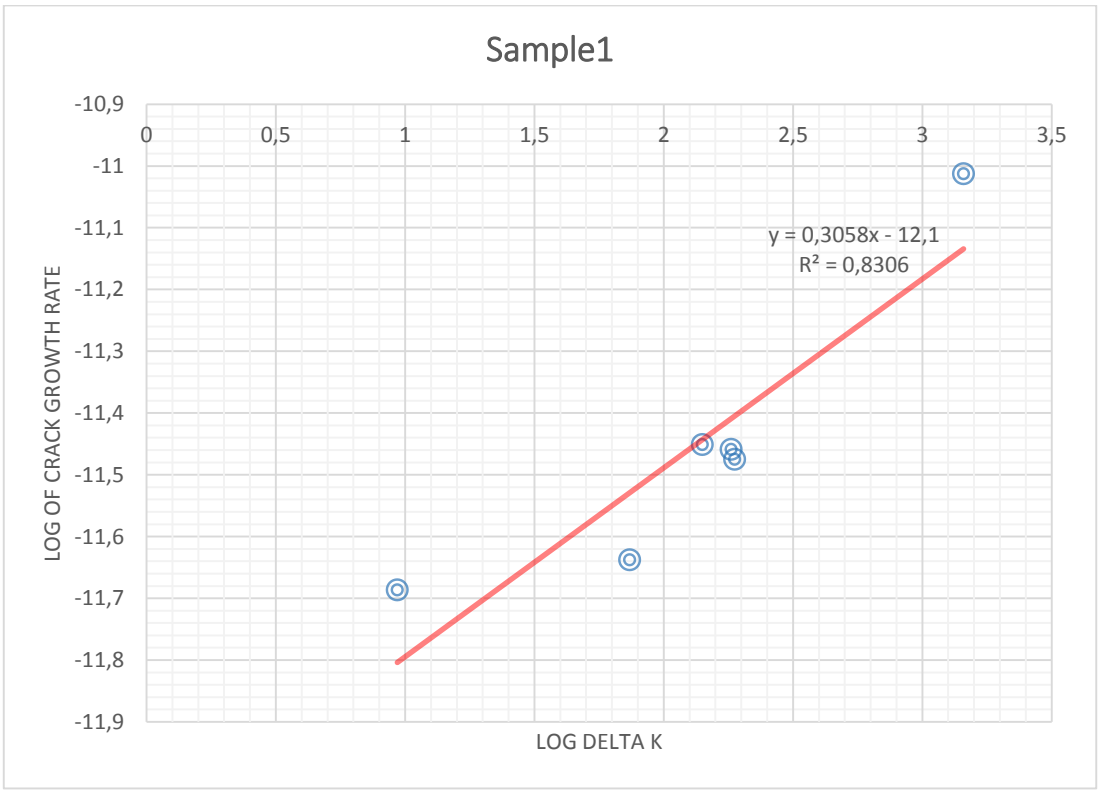


**Figure 6-2: Best fit line**

From this best fit line fitted with a correlation constant of 0.91, a gradient of 0.3058 and intercept of -12.1 were found. From these value the following values of $C$ and $m$ were calculated.

$$C = 7.943 \times 10^{-13} \; and \; m = 0.3058$$

A crack growth law of the following form was established;

$$\frac{dn}{da} = 7.943 \times 10^{-13} (\Delta K)^{0.3058} \tag{98}$$

The values of $C$ and $m$ in this case are not material constants but rather structure constants for this set-up. Table 6-2 shows a comparison between the cracks calculated from this law and the actual crack size. The average value of the variance is 11.766%. The same procedure described here was applied to data for sample 1 and a crack growth law with $C = 4.1 \times 10^{-14} \; and \; m = 0.7466$. The variance for this law averaged at -17.969%.

**Table 6-2: Comparison of the calculated crack length to the actual length**

| Crack length (Calculated ) | Crack length(Actual) | Variance |
|---|---|---|
| 375,57 | 485,30 | -22,61 |
| 200,15 | 167,30 | 19,63 |
| 307,33 | 84,33 | 264,44 |
| 198,12 | 173,60 | 14,12 |
| 89,28 | 222,50 | -59,87 |
| 79,12 | 102,90 | -23,11 |
| 183,04 | 176,80 | 3,53 |
| 150,00 | 115,10 | 30,32 |
| 181,26 | 81,19 | 123,25 |
| 25,16 | 61,59 | -59,15 |
| 21,10 | 44,87 | -52,96 |
| 9,61 | 266,90 | -96,40 |
| | **Average** | **11,7662** |

### 6.3 Equivalent Initial Flaw Size (EIFS)

The Equivalent Initial Flaw Size (EIFS) is the size of the initial flaw that under-static cyclic loading would result in a prescribed endurance. The calculation of the value of the EIFS was based on the established crack growth laws and back extrapolation of the fatigue data.

Integration of the Paris law given by equation (93) for a centre crack on an infinite plate will give the following result:

$$a_f^{\frac{2-m}{2}} + a_o^{\frac{2-m}{2}} = \left(\frac{m-2}{2}\right)\frac{C}{\sqrt{\pi}^3}.N \qquad (99)$$

Where *N* is the number of fatigue cycles.

Where:

$a_f$ is the final crack length after *N* cycles

$a_o$ is the EIFS

For sample 1 with a maximum final crack length of 266.9 microns, the EIFS was found to be 266.899 microns. For the second sample the EIFS was found to be 270.40 microns.

Assuming a linear relationship between the EISF and the actual average fret marks dimensions, the following dimensions were obtained for an EIFS of size zero;

- Fret mark length of 2457.538 microns
- Fret mark width of 407.98 microns
- Fret mark Depth of 217.413 microns

These dimensions can be taken as the maximum allowable initial flaw size for the conductor at manufacturing.

# 7. Conclusion

The surface quality of the manufactured TERN ACSR conductor has been studied and its contact mechanics analysed. Both linear elastic and nonlinear finite element analysis has been used to determine the normal contact force and hence the tension injected in the conductor during manufacturing to result in this surface quality. From the conductor inner contact mechanics model presented, it was shown that a tension of 4.4kN was used during the manufacturing of the conductor. This tension resulted in an interference averaging about 432 microns in the outer layer.

The outer layer has the smallest equivalent radius and hence will have the deepest fret marks as the depth is inversely proportional to the equivalent radius. These deep marks will result in a higher stress concentration factor and hence earlier nucleation of cracks. For layers with large equivalent radii and hence large fret marks, crack nucleation will be delayed but if the surface becomes too large, multiple cracks might initiate and eventually merge to cause failure. Hence the equivalent radius must not be too large even if a larger one would result in a lower stress concentration.

The calculated tension of 4.4kN will require the bobbin braking system to be set at 12.83kg (≅13) for a bobbin of 200mm flange size. From the results presented it is recommended that the winding set-up is such that the lay ratios for the contacting layers are relatively closer to each and closer to the maximum recommended lay for those layers for improved strand surface quality. Although a maximum equivalent radii to result in theoretically no fret marks on the strand surfaces has being given, it would be practically too challenging to achieve it. The calculated radius of 12.77mm can be achieved by setting the outer layer lay ratio to 14 which is the maximum permissible but this will require the mid-layer ratio to be set to over 20. This is would be way above the recommended maximum ratio of 15 for this layer and hence the conductor would not be compliant to the current manufacturing standards.

The analyses from the Energy dispersive Spectroscopy (EDS) showed that oxygen is present before and after the fatigue testing indicating that fretting was occurring throughout the life of the conductor samples. The presence of a high percentage of zinc (maximum of 13.45%) for an untested sample and 0% after testing indicates that there might be some of form of loss of the galvanization on the core wires.

The fractographic analysis showed that by 40 million cycles of fatigue testing, cracks had already evolved and by 50 million cycles they had grown to a maximum size of 485.3 microns.

From the established fatigue crack propagation models, the equivalent initial flaw size of 454.49 microns and 270.43 microns for sample one and two were calculated respectively. Using the EISF and assuming a linear back extrapolation, the maximum allowable surface defect of the conductor was estimated to be 2457.54 microns, 407.98 microns and 217.41microns for the length, width and depth of the fret marks respectively.

# 8. References


1. Shigley,J., and Bundynas, R., (2008). Mechanical Engineering Design. Tata McGraw-Hill, New Delhi.
2. Jansen, M., Zuidema, J., and Wanhill, R.,(2002). Fracture Mechanics, 2nd Edition, Spons Press, London.
3. Mathur, D., (1981).Mechanics. S. Chand and Company limited, New Delhi.
4. Guirgutiu, V.,(2008). Structural Health Monitoring with Piezoelectric Wafer Active Sensors. Elsevier, New York.
5. T.L. Anderson, T.L,. (1991). Fracture Mechanics, Fundamentals and Applications. CRC Press, Florida.
6. S. Rao, S.,(2004). Mechanical Vibrations, 4th Edition. Pearson Education, Miami.
7. Benham, P.P,. and R.J. Crawford, R.J,.(1987).Mechanics of Engineering Materials. Longman Scientific & Technical, New York.
8. Timoshenko, S., and J. Gere, J,.(1998). Mechanicals of Materials. Stanley Thornes Ltd, Cheltenham.
9. Broek, D,.(1986). Elementary Engineering Fracture Mechanics, 4th Edition, Kluwer Academic Publishers, Dordrecht.
10. Bougue, M,.(2009).High Voltage overhead Power Lines, Theoretical Calculations and formulae for conductor installations. Crown Publications cc, Johannesburg.
11. O'Connor, P.D,. and Kleyner, A,.(2012). Practical Reliability Engineering, 5th Edition, Wiley, West Sussex.
12. Bisnatch, s,. et al (2006). The Fundamentals and Practice of Overhead Line Maintenance. Crown Publishers cc, Johannesburg.
13. Kogut, L. and Etsion, I., 2002. Elastic-plastic contact analysis of a sphere and a rigid flat. Journal of Applied Mechanics.
14. Sanders A.P. and Brannon R.M., 2011.Determining a surrogate contact pair in hertzian contact problem. Journal of Tribology.
15. Vu-quoc, L., Zhang, X., and Lesburg, L. 2000. A Normal Force-Displacement Model for Contacting Spheres Accounting for Plastic Deformation: Force Driven Formulation. ASME J. Appl. Mech, 67, pp.363-371.
16. Antoine, J. F., Visa, C., Sauvey, C., and Abba, G. 2006.Approximate analytical Model for Hertzian Elliptical Contact Problems. ASME J. Tribology.
17. Sanchez-Brea, L.M., Gomez-Pedrero, J.A., and Bernabeu, E. 1999. Measurement of surface defects on thin steel wires by atomic force microscopy. Journal of Applied Surface science.

18. Kogut, L. and Etsion, I. 2002. A Finite Element Based Elastic-Plastic Model for the Contact of Rough surfaces. Tribology Transactions
19. Johnson, K. L., 1985. Contact Mechanics, First Ed, Cambridge University Press, Cambridge.
20. Timoshenko, S.P., and Goodier, J. N. 1970.Theory of Elasticity. Second Ed, McGraw Hill, New York)
21. Cardou, A. 2013. Stick-Slip Mechanical Models for Overhead Electrical Conductors in Bending. Universite' Laval, Quebec)
22. Hale, L. C. 1999. "Contact Mechanics, in "Principles and Techniques for designing precision machines. "MIT PhD Thesis, pp. 417-426.
23. Rawlins, C.B. 2005. Analytical Elements of Overhead Conductor Fabrication. First Ed. Fultus Corporation.
24. The Planning, Design and construction of Overhead Power Lines .2010. Eskom Power series
25. Brandon, D. and Kaplan, D. W. 2008. Microstructural Characterization of Materials. Second Ed. John Wiley & sons, Ltd, West Sussex)
26. Xie, J. 2011. Stereomicroscopy: 3D Imaging and the Third Dimension Measurement. *Application Note, Agilent Technologies.*
27. EPRI AC Transmission Line Reference Book-200kV and Above.2006. 2nd Ed, *the Orange Book*
28. https://en.wikipedia.org/wiki/K%C3%A1rm%C3%A1n_vortex_street
29. http://www.mscsoftware.com/product/marc
30. http://www.afgrow.net/applications/DTDHandbook/
31. http://www.mech.utah.edu/~me7960/lectures/Topic7-ContactStressesAndDeformations.pdf
32. http://feaforall.com/2014/10/23/hertz-contact/
33. http://solareis.anl.gov/documents/docs/APT_61117_EVS_TM_08_4.pdf
34. https://www.jic.ac.uk/microscopy/intro_EM.html
35. https://books.google.co.za/books?id=NojlBwAAQBAJ&pg=PA106&lpg
36. http://www.microscopemaster.com/electron-microscope.html
37. http://www.mechanical.in/engineering-metrology-and-measurements-subject-notes/
38. http://www.nist.gov/calibrations/upload/89-4088.pdf
39. https://www.youtube.com/watch?v=oNqSzzycRhw
40. http://www.sciencedirect.com/science/article/pii/S0142112308001710
41. http://www.managementstudyguide.com/quality-control-techniques.htm

# Annexure A
# Strands Tensile Tests Certificate

# Annexure B

# Electron dispersive spectroscopy (EDS) reports

**Report 1: Outer Layer**

- **Strand 1**

| Strand 1_1 | Wt% | Wt% Sigma |
|---|---|---|
| C | 11.32 | 0.28 |
| O | 19.35 | 0.18 |
| Na | 0.04 | 0.03 |
| Al | 67.31 | 0.49 |
| Si | 0.13 | 0.04 |
| S | 0.37 | 0.04 |
| Cl | 0.19 | 0.04 |
| Fe | 0.17 | 0.22 |
| Ni | 0.78 | 0.58 |
| Ag | 0.33 | 0.12 |
| Total | 100.00 | |

**Strand 1_1**

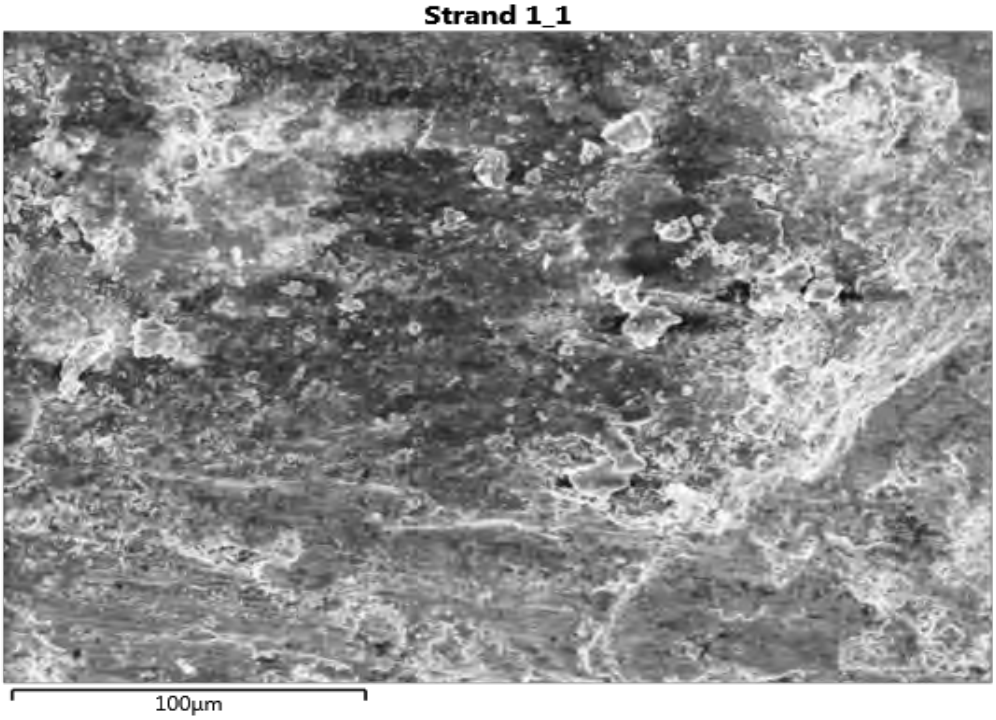

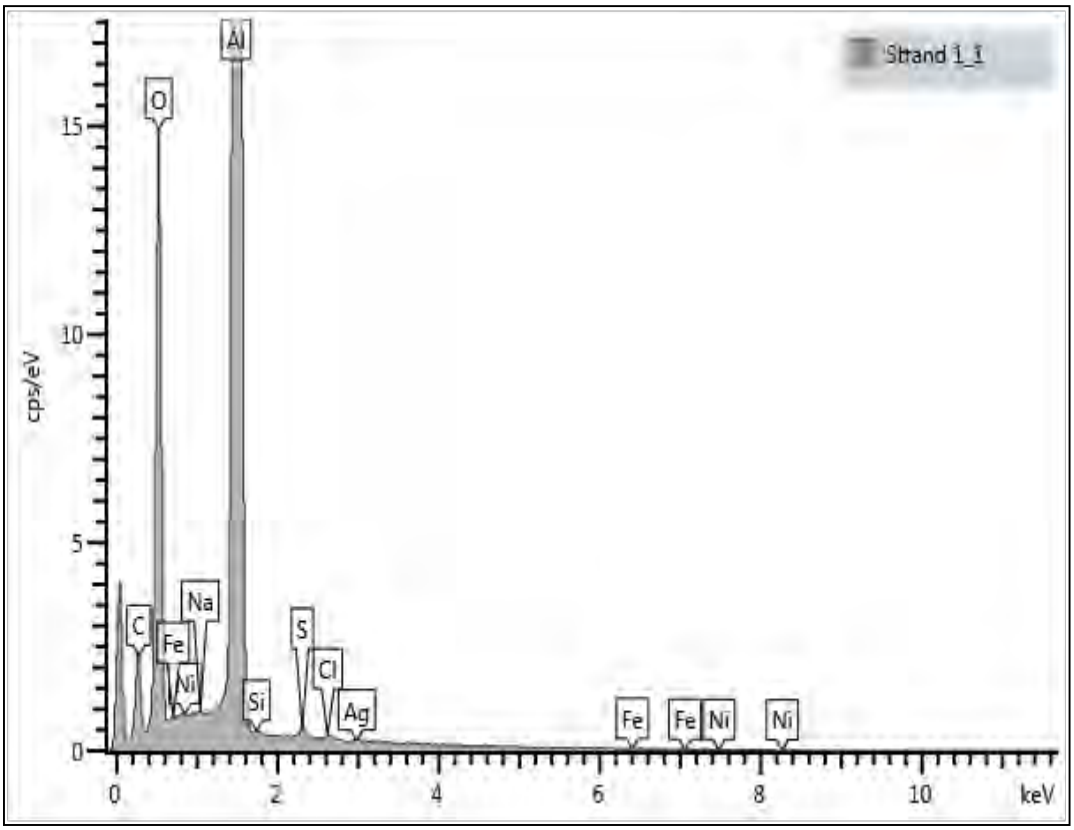
Strand 1_1
cps/eV
keV
O
Al
C
Fe
Ni
Na
Si
S
Cl
Ag
Fe
Fe
Ni
Ni
0
5
10
15
0
2
4
6
8
10

**Report 2: Middle layer**

- **Strand 1, point 1**

| Sample 2_1 | Wt% | Wt% Sigma |
|---|---|---|
| C | 0.00 | 0.00 |
| O | 10.23 | 0.22 |
| Al | 84.67 | 0.24 |
| Si | 3.75 | 0.06 |
| Ar | 0.08 | 0.05 |
| K | 0.23 | 0.03 |
| Ca | 0.09 | 0.02 |
| Fe | 0.49 | 0.04 |
| Ag | 0.47 | 0.12 |
| Total | 100.00 | |

**Sample 2_1**

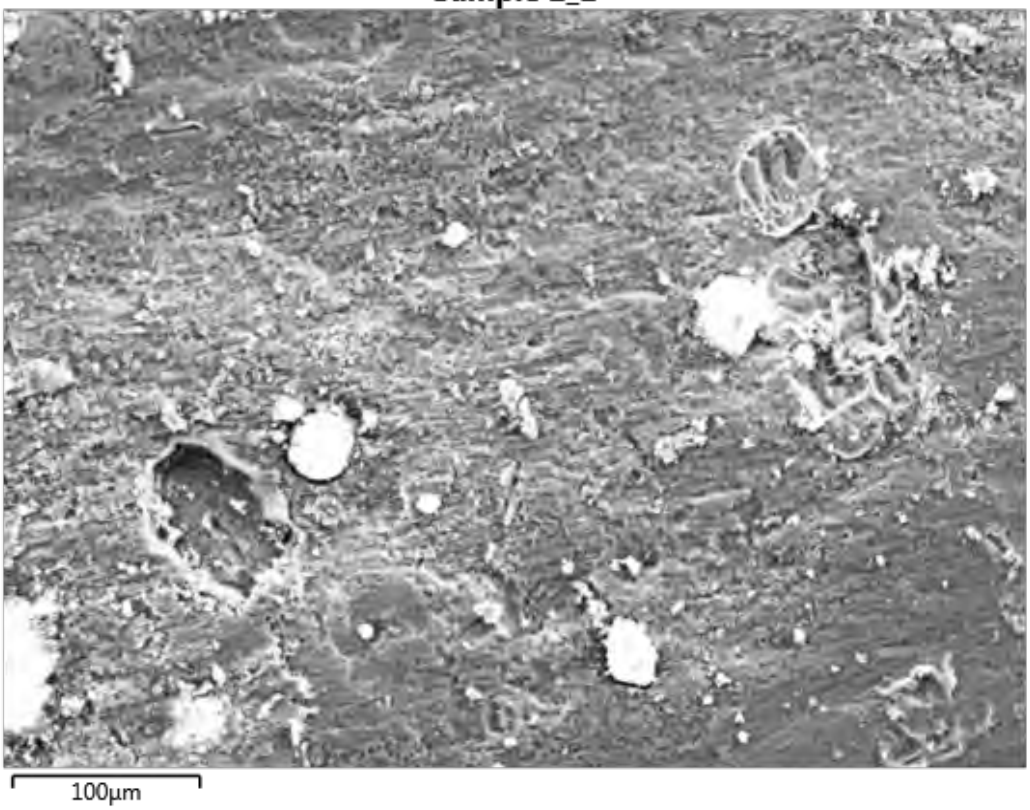

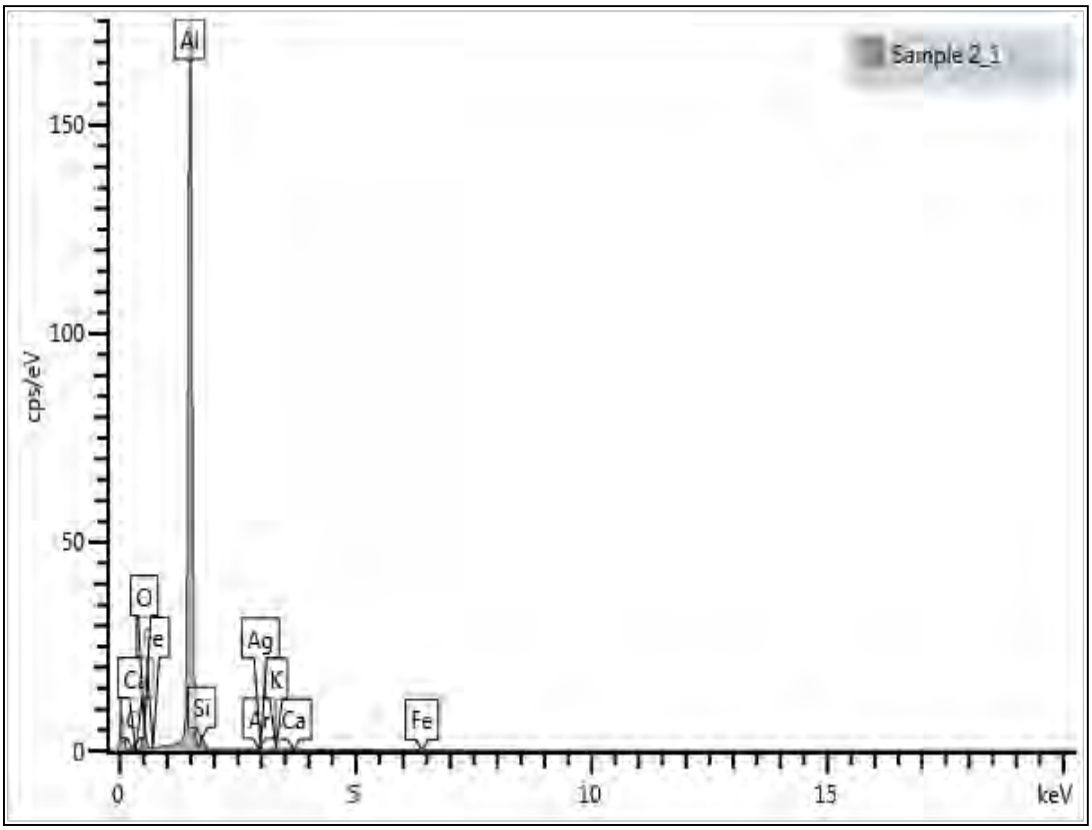
Sample 2_1
Al
O
Fe
Ag
K
Ca
Si
Fe
cps/eV
150
100
50
0
0
5
10
15
keV

**Strand 1, point 2**

| Sample 2_2 | Wt% | Wt% Sigma |
|---|---|---|
| C | 0.00 | 0.00 |
| O | 8.33 | 0.23 |
| Al | 89.85 | 0.26 |
| Si | 0.66 | 0.04 |
| Ar | 0.00 | 0.00 |
| K | 0.06 | 0.03 |
| Ca | 0.17 | 0.03 |
| Fe | 0.40 | 0.05 |
| Ag | 0.53 | 0.13 |
| Total | 100.00 | |

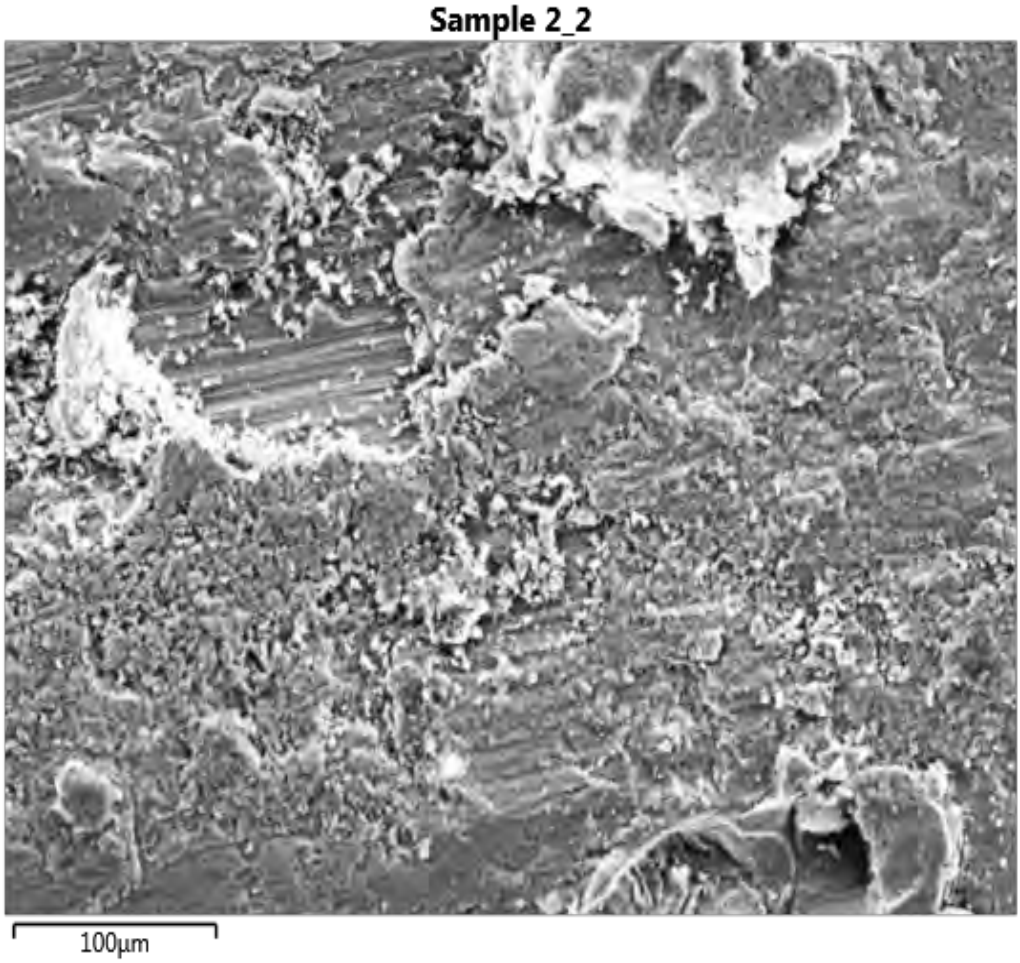

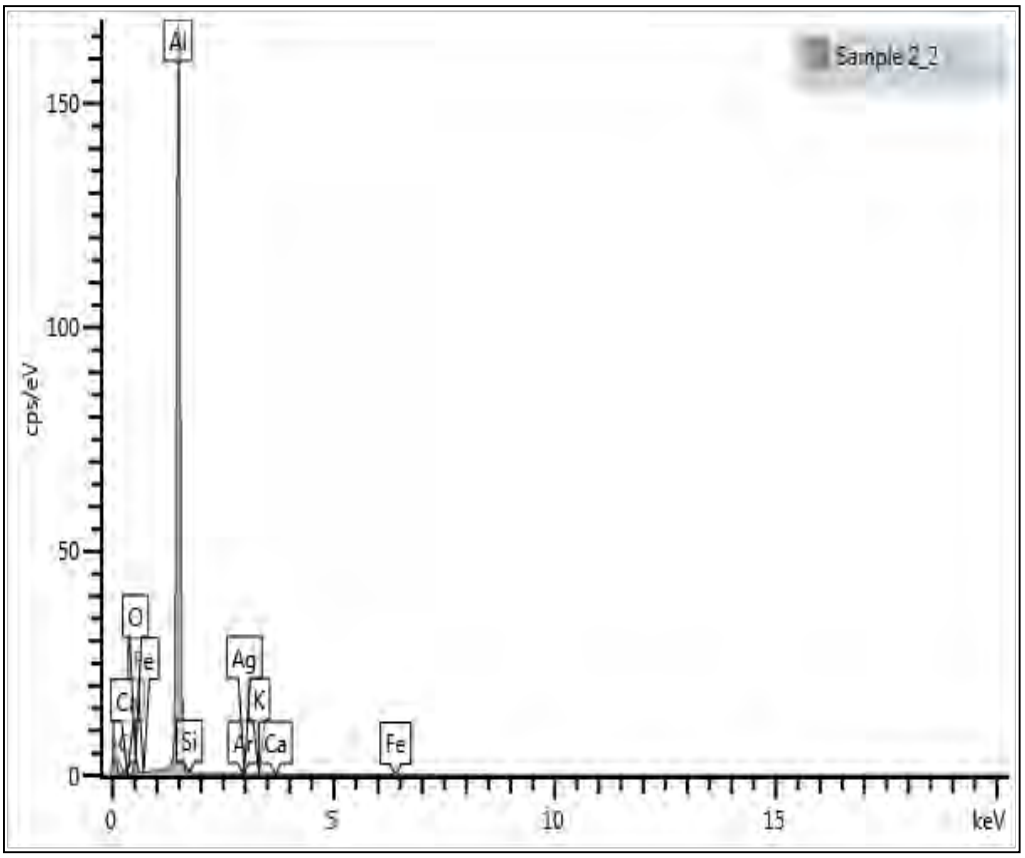


OXFORD INSTRUMENTS
*The Business of Science®*

**Report 3: Inner Layer**

**Strand 2-inner layer top, point 1**

| Spectrum 9 | Wt% | Wt% Sigma |
|---|---|---|
| C | 7.93 | 1.13 |
| O | 19.04 | 0.27 |
| Al | 28.90 | 0.37 |
| Si | 0.08 | 0.03 |
| K | 0.01 | 0.02 |
| Ca | 0.01 | 0.02 |
| Zn | 44.04 | 0.57 |
| Total | 100.00 | |

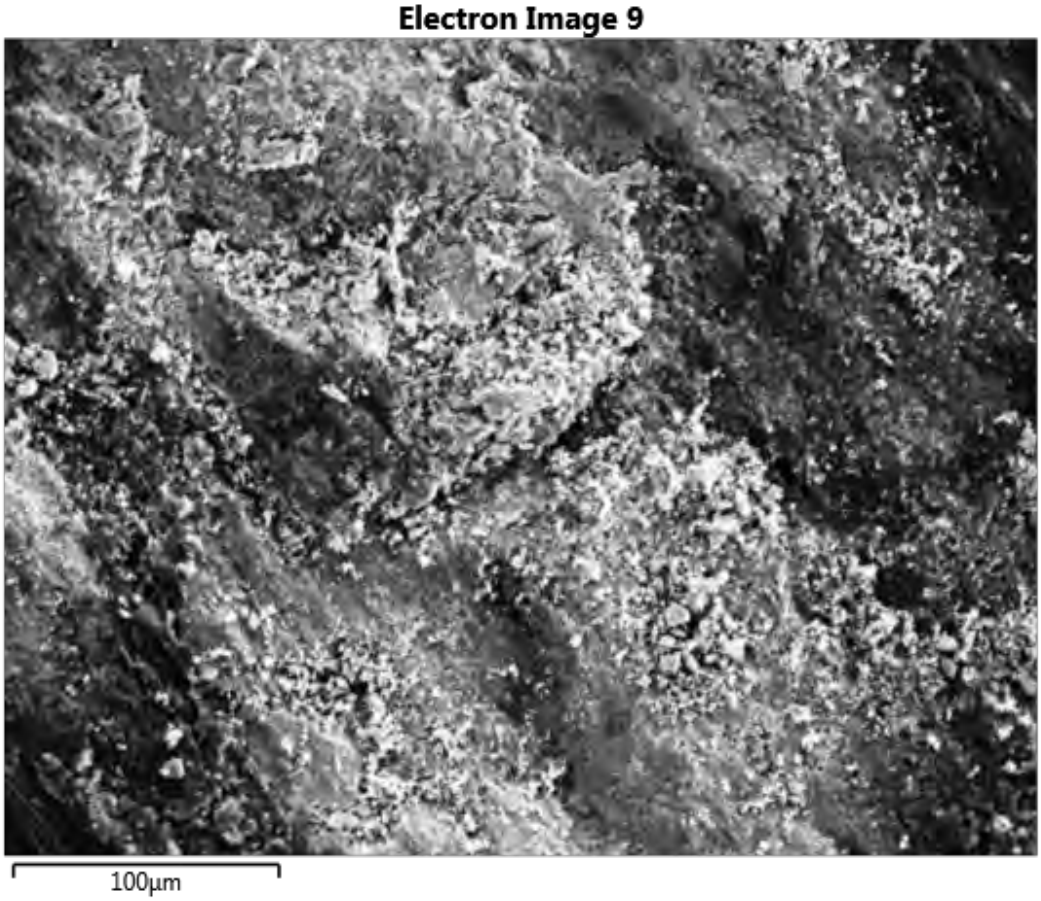

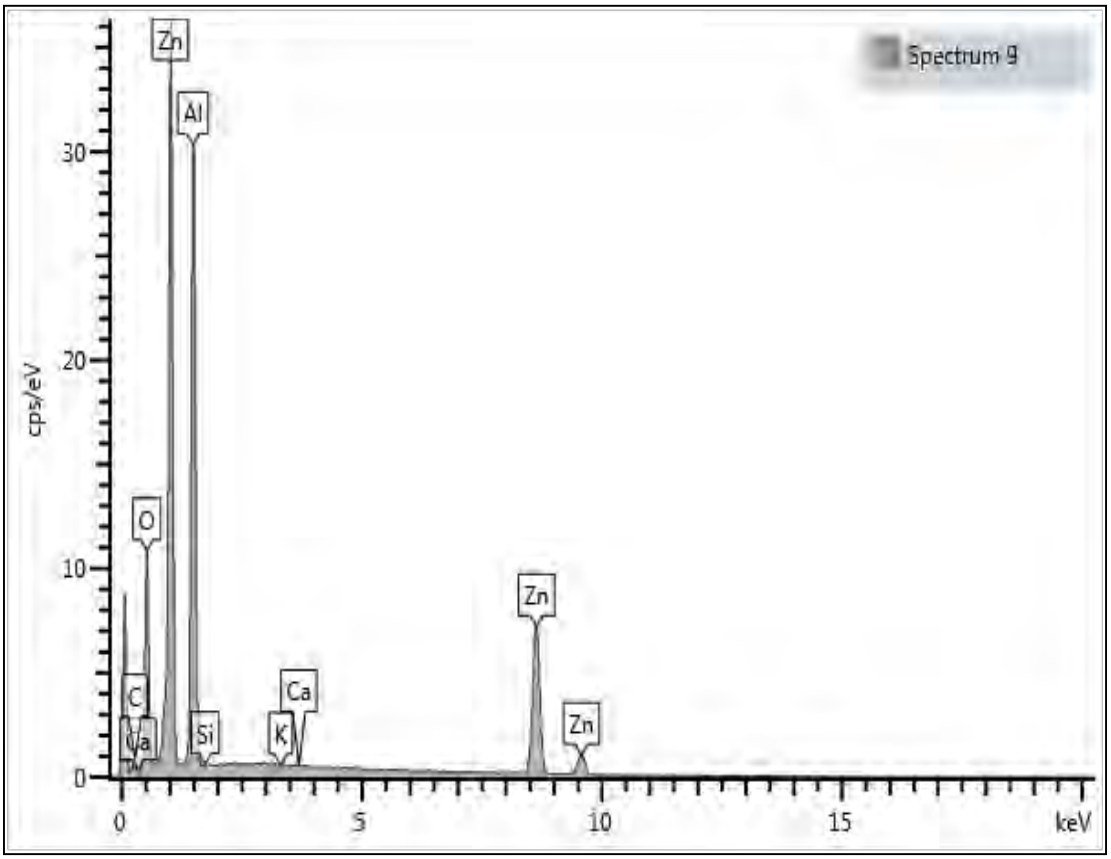
Spectrum 9
Zn
Al
O
C
Ca
K
Si
Zn
Zn
cps/eV
30
20
10
0
0
5
10
15
keV

**Report 1: Inner Layer**

| strand1_top | Wt% | Wt% Sigma |
|---|---|---|
| C | 9.56 | 0.80 |
| O | 15.48 | 0.21 |
| Al | 71.70 | 0.65 |
| Si | 2.76 | 0.06 |
| K | 0.11 | 0.03 |
| Fe | 0.40 | 0.05 |
| Total | 100.00 | |

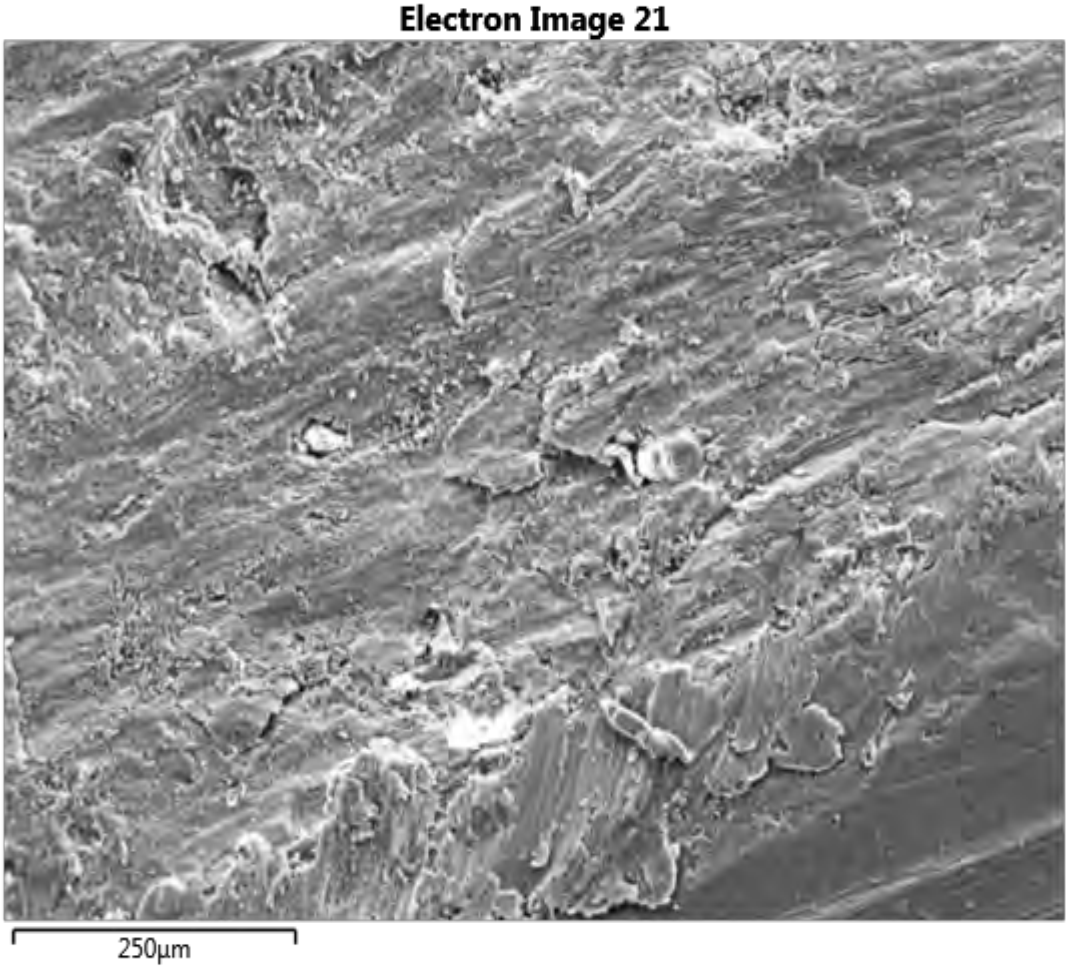

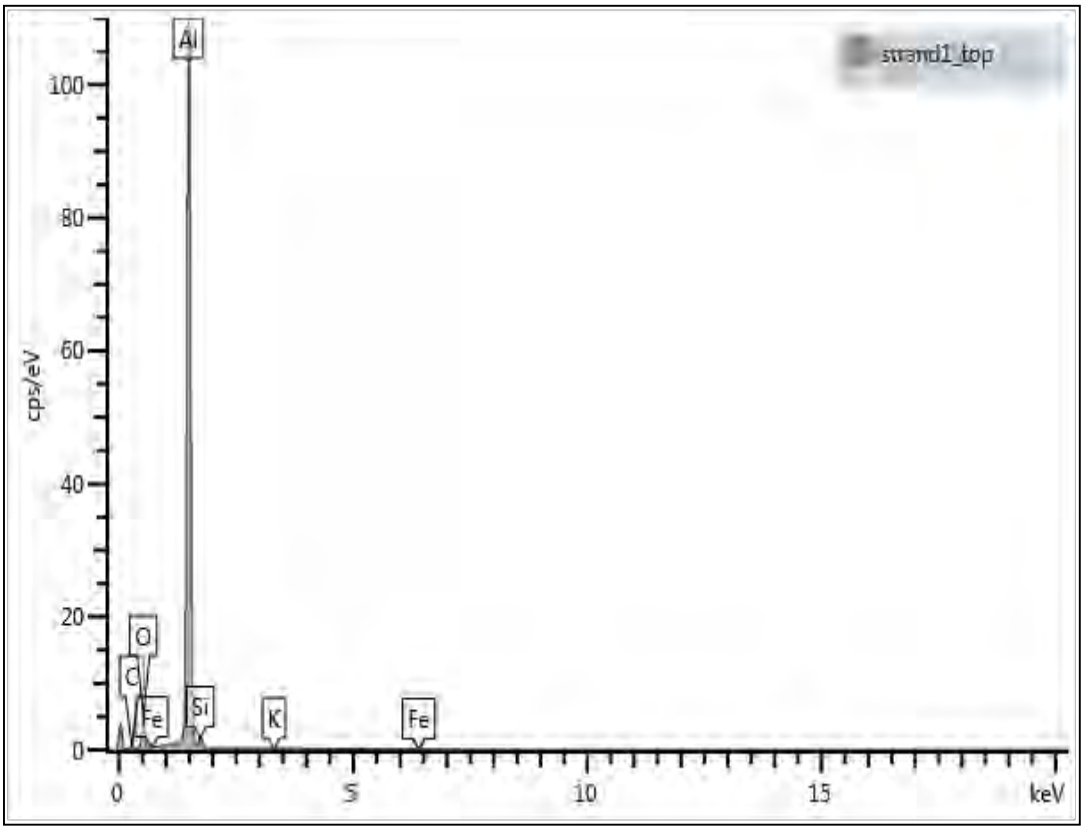
strand1_top
Al
O
C
Fe
Si
K
Fe
cps/eV
100
80
60
40
20
0
0
5
10
15
keV

**Report 2: Middle Layer**

| Spectrum 19 | Wt% | Wt% Sigma |
|---|---|---|
| O | 17.37 | 0.17 |
| Al | 76.14 | 0.18 |
| Si | 5.72 | 0.08 |
| Ar | 0.12 | 0.03 |
| K | 0.15 | 0.03 |
| Fe | 0.50 | 0.05 |
| Total | 100.00 | |

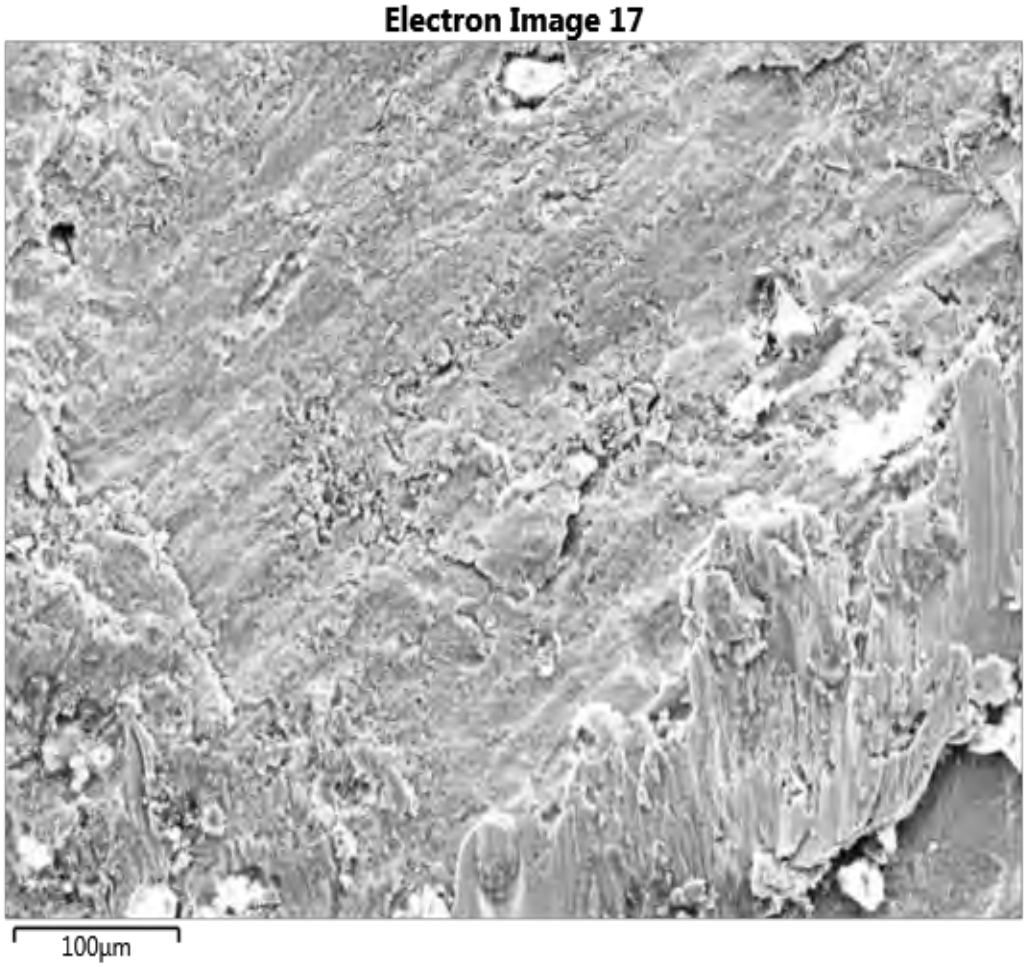

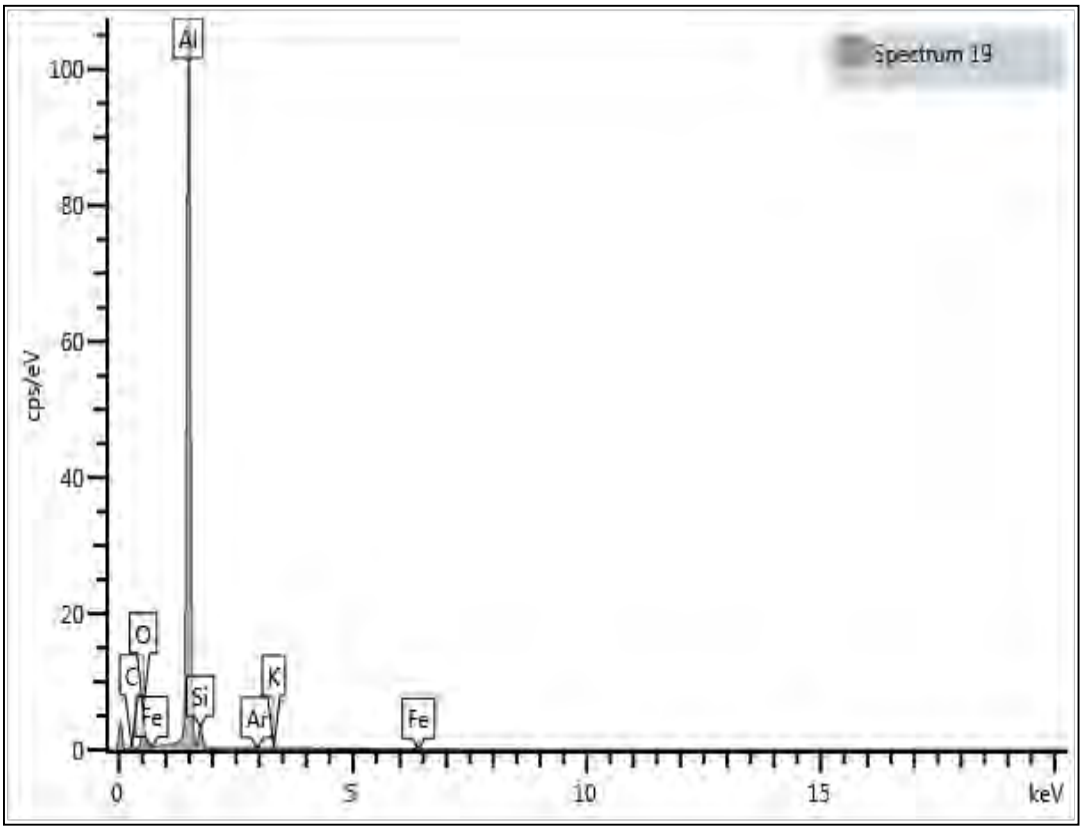
Spectrum 19
Al
O
C
Fe
Si
Ar
K
Fe
cps/eV
100
80
60
40
20
0
0
5
10
15
keV

**Report 3: Outer Layer**

| Spectrum 25 | Wt% | Wt% Sigma |
|---|---|---|
| O | 6.92 | 0.20 |
| Al | 90.74 | 0.23 |
| Si | 1.87 | 0.09 |
| Ca | 0.02 | 0.04 |
| Fe | 0.45 | 0.08 |
| Total | 100.00 | |

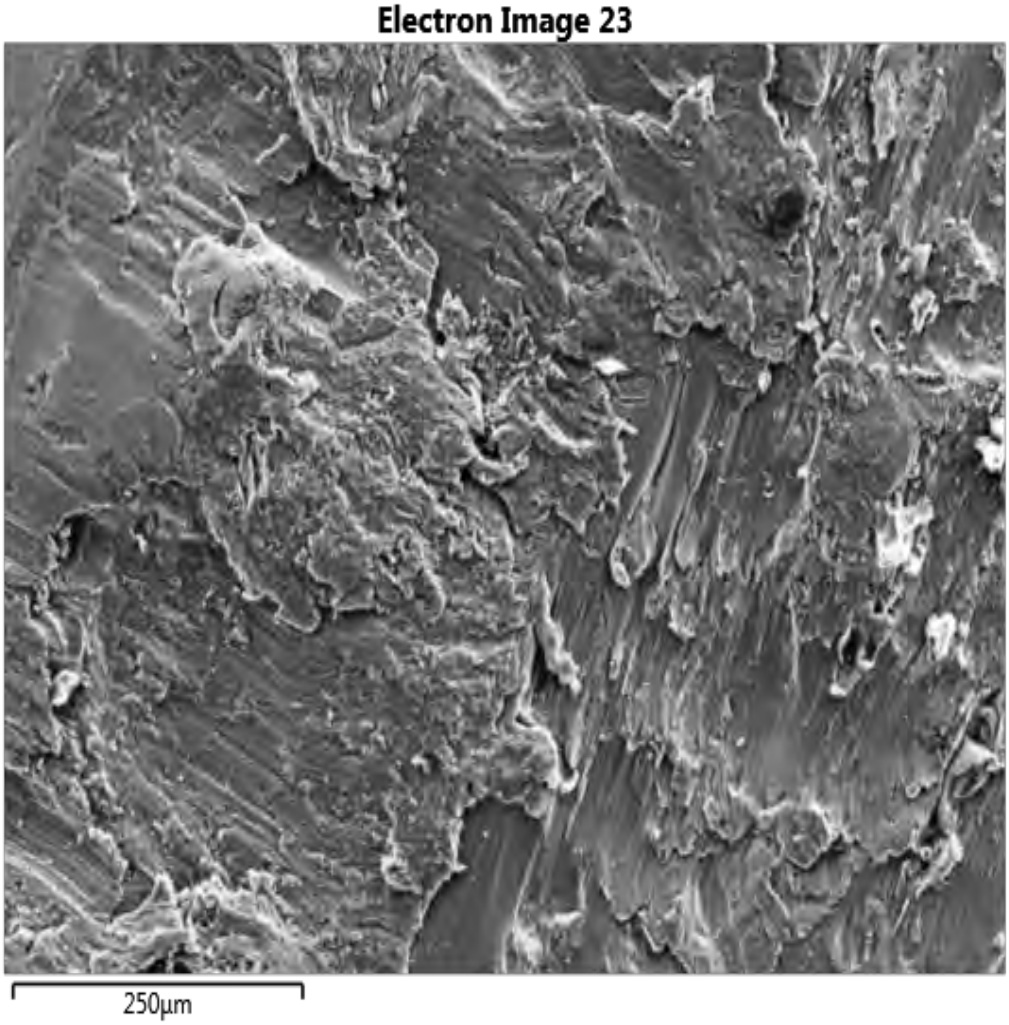

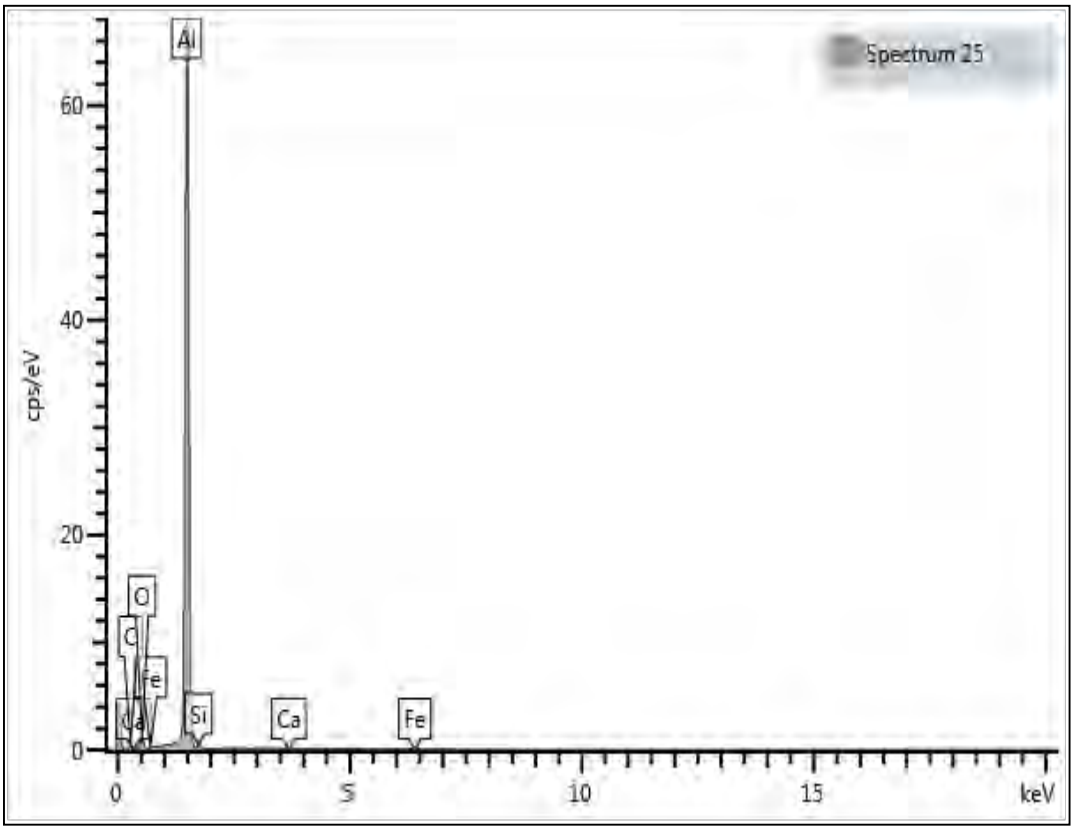
Spectrum 25
Al
O
C
Fe
Ca
Si
Ca
Fe
cps/eV
60
40
20
0
0
5
10
15
keV

# Annexure C

## Simulation results for different equivalent radii

**Table C1: Simulation results for sphere of equivalent radius of 8.584mm**

| Increment | Normal Contact force | Stress | Plastic strain |
|---|---|---|---|
| 1 | 24.72 | 38.18 | 6.805E-4 |
| 2 | 40.21 | 49.66 | 2.95E-3 |
| 3 | 49.87 | 57.58 | 5.728E-3 |
| 4 | 56.7 | 63.74 | 8.726E-3 |
| 5 | 62.04 | 68.86 | 1.19E-2 |
| 6 | 66.47 | 73.29 | 1.52E-2 |
| 7 | 70.3 | 77.23 | 1.856E-2 |
| 8 | 73.7 | 80.79 | 2.197E-2 |
| 9 | 76.76 | 84.06 | 2.542E-2 |
| 10 | 79.56 | 87.08 | 2.891E-2 |
| 11 | 82.15 | 89.91 | 3.242E-2 |
| 12 | 84.56 | 92.57 | 3.596E-2 |
| 13 | 86.82 | 95.08 | 3.951E-2 |
| 14 | 88.95 | 97.47 | 4.309E-2 |
| 15 | 90.96 | 99.75 | 4.669E-2 |
| 16 | 92.88 | 101.9 | 5.03E-2 |
| 17 | 94.7 | 104.0 | 5.393E-2 |
| 18 | 96.45 | 106.0 | 5.758E-2 |
| 19 | 98.12 | 108.0 | 6.125E-2 |
| 20 | 99.73 | 109.9 | 6.493E-2 |
| 21 | 100.7 | 113.1 | 7.149E-2 |
| 22 | 101.0 | 116.4 | 7.862E-2 |
| 23 | 101.3 | 119.5 | 8.582E-2 |
| 24 | 101.5 | 122.6 | 9.308E-2 |
| 25 | 101.8 | 125.5 | 1.004E-1 |
| 26 | 102.0 | 128.2 | 1.078E-1 |
| 27 | 102.2 | 130.9 | 1.152E-1 |
| 28 | 102.4 | 133.6 | 1.227E-1 |

| Increment | Normal Contact force | Stress | Plastic strain |
|---|---|---|---|
| 29 | 102.5 | 136.1 | 1.303E-1 |
| 30 | 102.7 | 138.6 | 1.379E-1 |
| 31 | 102.8 | 141.0 | 1.456E-1 |
| 32 | 103.0 | 143.3 | 1.534E-1 |
| 33 | 103.1 | 145.6 | 1.612E-1 |
| 34 | 103.2 | 147.8 | 1.691E-1 |
| 35 | 103.3 | 150.0 | 1.771E-1 |
| 36 | 103.4 | 152.2 | 1.853E-1 |
| 37 | 103.5 | 154.3 | 1.935E-1 |
| 38 | 103.5 | 156.5 | 2.019E-1 |
| 39 | 103.6 | 158.5 | 2.109E-1 |
| 40 | 103.7 | 160.6 | 2.189E-1 |
| 41 | 103.7 | 162.6 | 2.275E-1 |
| 42 | 103.8 | 164.6 | 2.362E-1 |
| 43 | 103.9 | 166.6 | 2.45E-1 |
| 44 | 103.9 | 168.6 | 2.53E-1 |
| 45 | 103.9 | 170.5 | 2.628E-1 |
| 46 | 104.0 | 172.4 | 2.718E-1 |
| 47 | 104.0 | 174.3 | 2.809E-1 |
| 48 | 104.0 | 176.2 | 2.9E-1 |
| 49 | 104.1 | 178.0 | 2.993E-1 |
| 50 | 104.1 | 179.9 | 3.086E-1 |

**Table C2: Simulation results for sphere of equivalent radius of 6.627mm**

| Increment | Normal Contact force | Stress | Plastic strain |
|---|---|---|---|
| 1 | 27.01 | 44.41 | 1.693E-3 |
| 2 | 39.05 | 56.55 | 5.294E-3 |
| 3 | 45.99 | 64.89 | 9.371E-3 |
| 4 | 51.0 | 71.38 | 1.37E-2 |
| 5 | 55.04 | 76.8 | 1.814E-2 |
| 6 | 58.47 | 81.52 | 2.265E-2 |
| 7 | 61.47 | 85.72 | 2.72E-2 |
| 8 | 64.15 | 89.53 | 3.18E-2 |
| 9 | 66.59 | 93.03 | 3.644E-2 |
| 10 | 68.83 | 96.28 | 4.11E-2 |
| 11 | 70.91 | 99.33 | 4.579E-2 |
| 12 | 72.85 | 102.2 | 5.051E-2 |
| 13 | 74.67 | 104.9 | 5.525E-2 |
| 14 | 76.39 | 107.5 | 6.002E-2 |
| 15 | 78.01 | 110.0 | 6.481E-2 |
| 16 | 79.14 | 113.7 | 7.246E-2 |
| 17 | 79.42 | 118.0 | 8.184E-2 |
| 18 | 79.66 | 122.0 | 9.131E-2 |
| 19 | 79.87 | 125.8 | 1.009E-1 |
| 20 | 80.05 | 129.4 | 1.106E-1 |
| 21 | 80.21 | 132.9 | 1.203E-1 |
| 22 | 80.35 | 136.2 | 1.302E-1 |
| 23 | 80.47 | 139.4 | 1.401E-1 |
| 24 | 80.54 | 142.5 | 1.502E-1 |
| 25 | 80.67 | 145.5 | 1.604E-1 |
| 26 | 80.75 | 148.5 | 1.706E-1 |
| 27 | 80.82 | 151.3 | 1.812E-1 |
| 28 | 80.88 | 154.1 | 1.92E-1 |
| 29 | 80.93 | 156.8 | 2.028E-1 |
| 30 | 80.98 | 159.5 | 2.138E-1 |
| 31 | 81.01 | 162.1 | 2.249E-1 |
| 32 | 81.04 | 164.7 | 2.362E-1 |

| Increment | Normal Contact force | Stress | Plastic strain |
|---|---|---|---|
| 33 | 81.06 | 167.3 | 2.476E-1 |
| 34 | 81.08 | 169.8 | 2.591E-1 |
| 35 | 81.09 | 172.3 | 2.708E-1 |
| 36 | 81.1 | 174.7 | 2.826E-1 |
| 37 | 81.11 | 177.1 | 2.945E-1 |
| 38 | 81.11 | 179.5 | 3.065E-1 |
| 39 | 81.10 | 181.9 | 3.187E-1 |
| 40 | 81.10 | 184.2 | 3.31E-1 |
| 41 | 81.09 | 186.5 | 3.435E-1 |
| 42 | 81.08 | 188.8 | 3.562E-1 |
| 43 | 81.07 | 191.1 | 3.691E-1 |
| 44 | 81.06 | 193.4 | 3.821E-1 |
| 45 | 81.05 | 195.7 | 3.954E-1 |
| 46 | 81.03 | 198.0 | 4.088E-1 |
| 47 | 81.02 | 200.2 | 4.225E-1 |
| 48 | 81.0 | 202.5 | 4.364E-1 |
| 49 | 80.98 | 204.8 | 4.505E-1 |
| 50 | 80.96 | 207.0 | 4.649E-1 |

**Table C3: Simulation results for a sphere of equivalent radius of 9.092mm**

| Increment | Normal Contact force | Stress | Plastic strain |
|---|---|---|---|
| 1 | 29.41 | 40.46 | 1.012E-3 |
| 2 | 44.64 | 51.84 | 3.606E-3 |
| 3 | 53.62 | 59.63 | 6.607E-3 |
| 4 | 59.93 | 65.68 | 9.845E-3 |
| 5 | 64.94 | 70.72 | 1.321E-2 |
| 6 | 69.15 | 75.09 | 1.665E-2 |
| 7 | 72.82 | 78.98 | 2.013E-2 |
| 8 | 76.08 | 82.49 | 2.366E-2 |
| 9 | 79.04 | 85.72 | 2.72E-2 |
| 10 | 81.75 | 88.71 | 3.078E-2 |
| 11 | 84.26 | 91.51 | 3.437E-2 |
| 12 | 86.61 | 94.14 | 3.799E-2 |
| 13 | 88.81 | 96.63 | 4.162E-2 |
| 14 | 90.88 | 99.0 | 4.527E-2 |
| 15 | 92.85 | 101.3 | 4.893E-2 |
| 16 | 94.72 | 103.4 | 5.261E-2 |
| 17 | 96.51 | 105.5 | 5.631E-2 |
| 18 | 98.22 | 107.5 | 6.002E-2 |
| 19 | 99.85 | 109.4 | 6.375E-2 |
| 20 | 101.3 | 111.8 | 6.836E-2 |
| 21 | 101.6 | 115.2 | 7.561E-2 |
| 22 | 101.8 | 118.5 | 8.292E-2 |
| 23 | 102.1 | 121.6 | 9.028E-2 |
| 24 | 102.3 | 124.6 | 9.771E-2 |
| 25 | 102.5 | 127.5 | 1.052E-1 |
| 26 | 102.7 | 130.2 | 1.123E-1 |
| 27 | 102.8 | 132.9 | 1.204E-1 |
| 28 | 103.0 | 135.5 | 1.28E-1 |
| 29 | 103.1 | 138.0 | 1.357E-1 |
| 30 | 103.2 | 140.5 | 1.435E-1 |
| 31 | 103.3 | 142.4 | 1.514E-1 |
| 32 | 103.4 | 145.2 | 1.593E-1 |

| Increment | Normal Contact force | Stress | Plastic strain |
|---|---|---|---|
| 33 | 103.5 | 147.5 | 1.672E-1 |
| 34 | 103.6 | 149.7 | 1.754E-1 |
| 35 | 103.6 | 151.9 | 1.837E-1 |
| 36 | 103.7 | 154.1 | 1.92E-1 |
| 37 | 103.8 | 156.2 | 2.004E-1 |
| 38 | 103.8 | 158.3 | 2.09E-1 |
| 39 | 103.8 | 160.4 | 2.176E-1 |
| 40 | 103.9 | 162.4 | 2.265E-1 |
| 41 | 103.9 | 164.4 | 2.35E-1 |
| 42 | 103.9 | 166.4 | 2.439E-1 |
| 43 | 104.0 | 168.4 | 2.528E-1 |
| 44 | 104.0 | 170.4 | 2.618E-1 |
| 45 | 104.0 | 172.3 | 2.708E-1 |
| 46 | 104.0 | 174.2 | 2.8E-1 |
| 47 | 104.0 | 176.1 | 2.892E-1 |
| 48 | 104.0 | 177.9 | 2.985E-1 |
| 49 | 104.0 | 179.8 | 3.079E-1 |
| 50 | 104.0 | 181.6 | 3.174E-1 |

**Table C4: Simulation results for a sphere of equivalent radius of 7.496 mm**

| Increment | Normal Contact force | Stress | Plastic strain |
|---|---|---|---|
| 1 | 27.08 | 44.41 | 1.693E-3 |
| 2 | 39.05 | 56.55 | 5.294E-3 |
| 3 | 45.99 | 64.89 | 9.37E-3 |
| 4 | 51.00 | 71.38 | 1.37E-2 |
| 5 | 55.04 | 76.80 | 1.814E-2 |
| 6 | 58.47 | 81.52 | 2.265E-2 |
| 7 | 61.47 | 85.72 | 2.72E-2 |
| 8 | 64.15 | 89.53 | 3.18E-2 |
| 9 | 66.59 | 93.03 | 3.644E-2 |
| 10 | 68.83 | 96.28 | 4.11E-2 |
| 11 | 70.91 | 99.33 | 4.579E-2 |
| 12 | 72.85 | 102.2 | 5.051E-2 |
| 13 | 74.67 | 104.9 | 5.525E-2 |
| 14 | 76.39 | 107.5 | 6.002E-2 |
| 15 | 78.01 | 110.0 | 6.481E-2 |
| 16 | 79.14 | 113.7 | 7.246E-2 |
| 17 | 79.42 | 118.0 | 8.184E-2 |
| 18 | 79.66 | 122.0 | 9.131E-2 |
| 19 | 79.87 | 125.8 | 1.009E-1 |
| 20 | 80.05 | 129.4 | 1.106E-1 |
| 21 | 80.21 | 132.9 | 1.203E-1 |
| 22 | 80.35 | 136.2 | 1.302E-1 |
| 23 | 80.47 | 139.4 | 1.401E-1 |
| 24 | 80.58 | 142.5 | 1.502E-1 |
| 25 | 80.67 | 145.5 | 1.604E-1 |
| 26 | 80.75 | 148.5 | 1.706E-1 |
| 27 | 80.82 | 151.3 | 1.812E-1 |
| 28 | 80.88 | 154.1 | 1.92E-1 |
| 29 | 80.93 | 156.8 | 2.028E-1 |
| 30 | 80.98 | 159.5 | 2.138E-1 |
| 31 | 81.01 | 162.1 | 2.249E-1 |
| 32 | 81.04 | 164.7 | 2.362E-1 |

| Increment | Normal Contact force | Stress | Plastic strain |
|---|---|---|---|
| 33 | 81.06 | 167.3 | 2.476E-1 |
| 34 | 81.08 | 169.8 | 2.591E-1 |
| 35 | 81.09 | 172.3 | 2.708E-1 |
| 36 | 81.10 | 174.7 | 2.826E-1 |
| 37 | 81.11 | 177.1 | 2.945E-1 |
| 38 | 81.11 | 179.5 | 3.065E-1 |
| 39 | 81.10 | 181.9 | 3.187E-1 |
| 40 | 81.10 | 184.2 | 3.31E-1 |
| 41 | 81.09 | 186.5 | 3.435E-1 |
| 42 | 81.08 | 188.8 | 3.562E-1 |
| 43 | 81.07 | 191.1 | 3.691E-1 |
| 44 | 81.06 | 193.4 | 3.821E-1 |
| 45 | 81.05 | 195.7 | 3.954E-1 |
| 46 | 81.03 | 198.0 | 3.954E-1 |
| 47 | 81.02 | 200.2 | 4.088E-1 |
| 48 | 81.00 | 202.5 | 4.225E-1 |
| 49 | 80.98 | 204.8 | 4.364E-1 |
| 50 | 80.96 | 207.0 | 4.505E-1 |

# ANNEXURE D

**Table D-1:Fatigue testing recordings for sample 1**

| | | | |
|---|---|---|---|
| 04 November 2014 | 00:00:00 | 00:05:00 | 00:05:00 |
| 04 November 2014 | 00:00:00 | 00:15:00 | 00:15:00 |
| 05 November 2014 | 00:03:31 | 00:25:25 | 0:21:54 |
| 05 November 2014 | 00:03:40 | 00:17:53 | 0:14:13 |
| 05 November 2014 | 00:26:38 | 01:08:30 | 0:41:52 |
| 05 November 2014 | 00:05:00 | 00:31:51 | 0:26:51 |
| 05 November 2014 | 00:00:00 | 01:00:00 | 1:00:00 |
| 05 November 2014 | 00:00:00 | 00:26:26 | 0:26:26 |
| 05 November 2014 | 00:00:00 | 00:12:03 | 0:12:03 |
| 06 November 2014 | 00:00:00 | 01:14:31 | 1:14:31 |
| 06 November 2014 | 00:00:31 | 00:08:35 | 0:08:04 |
| 06 November 2014 | 00:01:30 | 00:38:30 | 0:37:00 |
| 06 November 2014 | 00:06:00 | 00:16:31 | 0:10:31 |
| 06 November 2014 | 00:00:00 | 00:00:00 | 0:00:00 |
| 06 November 2014 | 00:00:00 | 00:00:00 | 0:00:00 |
| 06 November 2014 | 00:00:00 | 00:00:00 | 0:00:00 |
| 06 November 2014 | 00:01:54 | 02:21:54 | 2:20:00 |
| 07 November 2014 | 0:03:30 | 0:18:36 | 0:15:06 |
| 07 November 2014 | 0:19:05 | 03:43:09 | 3:24:04 |
| 07 November 2014 | 00:03:40 | 02:09:55 | 2:06:15 |
| 10 November 2014 | 00:00 | 01:00:00 | 1:00:00 |
| 10 November 2014 | 00:00:00 | 00:13:14 | 0:13:14 |
| 10 November 2014 | 00:00:00 | 05:30:00 | 5:30:00 |
| 11 November 2014 | 00:00:00 | 07:30:00 | 7:30:00 |
| 12 November 2014 | 00:00:00 | 07:35:06 | 7:35:06 |
| 13 November 2014 | 00:00:00 | 07:30:00 | 7:30:00 |
| 14 November 2014 | 08:21:00 | 10:54:00 | 2:33:00 |
| 14 November 2014 | 11:01:00 | 11:37:07 | 0:36:07 |
| 14 November 2014 | 11:37:00 | 13:40:00 | 2:03:00 |
| 14 November 2014 | 02:28:00 | 04:46:00 | 2:18:00 |
| 17 November 2014 | 00:00:00 | 07:00:00 | 7:00:00 |
| 18 November 2014 | 00:00:00 | 08:05:30 | 8:05:30 |
| 19 November 2014 | 00:00:00 | 09:01:09 | 9:01:09 |
| 20 November 2014 | 00:00:00 | 02:30:00 | 2:30:00 |
| 21 November 2014 | 00:00:00 | 07:10:00 | 7:10:00 |
| 24 November 2014 | 00:00:00 | 07:08:00 | 7:08:00 |
| 25 November 2014 | 00:00:00 | 07:48:55 | 7:48:55 |
| 27 November 2014 | 08:52:00 | 10:16:00 | 1:24:00 |
| 27 November 2014 | 00:00:00 | 01:51:36 | 1:51:36 |
| 27 November 2014 | 00:00:00 | 00:52:00 | 0:52:00 |
| 27 November 2014 | 00:00:00 | 00:58:40 | 0:58:40 |
| 27 November 2014 | 00:00:00 | 02:00:00 | 2:00:00 |
| 02 December 2014 | 00:00:00 | 02:35:00 | 2:35:00 |
| 03 December 2014 | 00:00:00 | 00:46:00 | 0:46:00 |

| | | | |
|---|---|---|---|
| 03 December 2014 | 00:00:00 | 05:25:00 | 5:25:00 |
| 04 December 2014 | 00:00:00 | 01:45:00 | 1:45:00 |
| 05 December 2014 | 00:00:00 | 00:56:00 | 0:56:00 |
| 05 December 2014 | 00:00:00 | 01:19:00 | 1:19:00 |
| 08 December 2014 | 00:00:00 | 03:54:00 | 3:54:00 |
| 08 December 2014 | 00:00:00 | 03:00:00 | 3:00:00 |
| 09 December 2014 | 00:00:00 | 06:37:00 | 6:37:00 |
| 10 December 2014 | 00:00:00 | 04:07:00 | 4:07:00 |
| 12 December 2014 | 00:00:00 | 02:00:00 | 2:00:00 |
| 12 January 2015 | 00:00:00 | 06:45:00 | 6:45:00 |
| 13 January 2015 | 00:00:00 | 07:00:00 | 7:00:00 |
| 14 January 1900 | 00:00:00 | 03:28:00 | 3:28:00 |
| 15 January 2015 | 00:00:00 | 03:30:00 | 3:30:00 |
| 16 January 2015 | 00:00:00 | 04:04:00 | 4:04:00 |
| 19 January 2015 | 00:00:00 | 01:20:00 | 4:04:00 |
| 20 January 2015 | 00:00:00 | 08:10:00 | 8:10:00 |
| 21 January 1900 | 00:00:00 | 3:37:00 | 8:53:35 |
| 22 January 2015 | 0:00:00 | 8:00:00 | 8:00:00 |
| 23 January 2015 | 0:00:00 | 8:30:00 | 8:30:00 |
| 26 January 1900 | 0:00:00 | 7:00:00 | 7:00:00 |
| 27 January 2015 | 0:00:00 | 6:01:00 | 6:01:00 |
| 28 January 2015 | 0:00:00 | 2:00:00 | 2:00:00 |
| 29 January 2015 | 0:00:00 | 8:00:00 | 8:00:00 |
| 30 January 2015 | 0:00:00 | 5:09:00 | 5:09:00 |
| 02 February 2015 | 0:00:00 | 3:32:00 | 3:32:00 |
| 03 February 2015 | 0:00:00 | 7:20:00 | 7:20:00 |
| 04 February 2015 | 0:00:00 | 8:00:00 | 8:00:00 |
| 05 February 2015 | 0:00:00 | 8:00:00 | 8:00:00 |
| 06 February 2015 | 0:00:00 | 4:49:00 | 4:49:00 |
| 09 February 2015 | 0:00:00 | 9:00:00 | 9:00:00 |
| 10 February 2015 | 0:00:00 | 2:40:00 | 2:40:00 |
| 11 February 2015 | 0:00:00 | 5:00:00 | 5:00:00 |
| 12 February 2015 | 0:00:00 | 7:30:00 | 7:30:00 |
| 13 February 2015 | 0:00:00 | 8:15:00 | 8:15:00 |
| 16 February 2015 | 0:00:00 | 8:18:00 | 8:18:00 |
| 17 February 2015 | 0:00:00 | 3:01:00 | 3:01:00 |
| 18 February 2015 | 0:00:00 | 7:31:00 | 7:31:00 |
| 19 February 2015 | 0:00:00 | 6:20:00 | 6:20:00 |
| 20 February 2015 | 0:00:00 | 8:00:00 | 8:00:00 |
| 23 February 2015 | 0:00:00 | 5:40:00 | 5:40:00 |
| 24 February 2015 | 0:00:00 | 8:00:00 | 8:00:00 |
| 25 February 2015 | 0:00:00 | 4:04:00 | 4:04:00 |
| **Total Duration** | | **3.5 months** | 344:35:42 |
| **Total No. of Cycles** | | | **50862222** |
| **Cycles in Million cycles** | | | **50,9** |